Università degli Studi di Trieste

XXV ciclo del dottorato di ricerca in Nanotecnologie

A closer look at heterogeneous catalysis: reaction intermediates at the single-molecule level

settore scientifico-disciplinare FIS/03 – Fisica della Materia

student Angelo Peronio

school director prof. Maurizio Fermeglia

supervisor prof. Giovanni Comelli

tutor dr. Carlo Dri

Academic year 2011/2012

UNIVERSITÀ DEGLI STUDI DI TRIESTE

XXV CICLO DEL DOTTORATO DI RICERCA IN NANOTECNOLOGIE

A CLOSER LOOK AT HETEROGENEOUS CATALYSIS: REACTION INTERMEDIATES AT THE SINGLE-MOLECULE LEVEL

settore scientifico-disciplinare FIS/03 – Fisica della Materia

STUDENT Angelo Peronio

SCHOOL DIRECTOR prof. Maurizio Fermeglia .....

SUPERVISOR prof. Giovanni Comelli .....

TUTOR dr. Carlo Dri .....

Academic year 2011/2012

Abstract

The present work pertains to the surface science approach to heterogeneous catalysis. In particular model systems for CO_2 hydrogenation to methanol, and NO selective catalytic reduction, are investigated by means of a combined approach, where the molecular-level insight provided by a low-temperature scanning tunneling microscope is complemented by density functional theory (DFT) calculations of their electronic structure. To this end, the Inelastic Electron Tunneling Spectroscopy (STM-IETS) technique was introduced for the first time in our laboratory, a recent development which allows to measure the vibrational spectrum of *individual molecules* adsorbed on a surface.

Regarding CO_2, we provide single molecule imaging and characterization of CO_2/Ni(110), chemisorbed with high charge transfer from the substrate, in an activated state that plays a crucial role in the hydrogenation process. We obtain a detailed characterization of the adsorption geometries and an estimate of the energies corresponding to the different adsorbed states. A consistent picture of CO_2 chemisorption on Ni(110) is provided on the basis of the newly available information, yielding a deeper insight into the previously existing spectroscopic and theoretical data.

In the Selective Catalytic Reduction (SCR) process, nitrogen oxide is *selectively* transformed to N_2 by reductants such as ammonia. The specificity of this reaction was tentatively attributed to the formation of NH_3−NO coadsorption complexes, as indicated by several surface science techniques. Here we characterize the NH_3−NO complex at the atomic scale on the (111) surface of platinum, investigating the intermolecular interactions that tune the selectivity. The structures that arise upon coadsorption of NH_3 and NO are analyzed in terms of adsorption sites, geometry, energetics and charge rearrangement. An ordered 2×2 adlayer forms, where the two molecules are arranged in a configuration that maximizes mutual interactions. In this structure, NH_3 adsorbs on top and NO on fcc-hollow sites, leading to a cohesional stabilization of the extended layer by 0.29 eV/unit cell. The calculated vibrational energies of the individually-adsorbed species and of the coadsorption structure fit the experimental values found in literature within less than 6%.

The characterizations and optimizations that had to be tackled in order to successfully perform STM-IETS measurement are eventually presented, focusing in particular on an original method which allows to increase the achieved resolution. Namely, the *modulation broadening* associated to phase-sensitive detection is reduced by employing a tailored modulation function, different from the commonly-used sinusoid. This method is not limited to STM-IETS, but can be easily applied whenever a lock-in amplifier is used to measure a second derivative.

Riassunto

Il presente lavoro di tesi tratta problemi di catalisi eterogenea con i metodi della scienza delle superfici. In particolare sono stati studiati sistemi-modello per l'idrogenazione dell'anidride carbonica a metanolo, e per la riduzione selettiva del monossido di azoto, combinando il dettaglio molecolare fornito dalla microscopia a scansione a effetto tunnel a bassa temperatura (LT-STM) con calcoli di struttura elettronica basati sulla teoria del funzionale della densità (DFT). È stata anche impiegata, per la prima volta nel nostro laboratorio, una recente tecnica sperimentale che consente si misurare spettri vibrazionali di *singole molecole* adsorbite su una superficie.

È stato caratterizzato l'adsorbimento di singole molecole di CO_2 sulla superficie (111) del nichel, dove queste chemisorbono ricevendo un forte trasferimento di carica dalla superficie. Questa specie attivata gioca un ruolo fondamentale nel processo di idrogenazione. Sono state ottenute le geometrie di adsorbimento, assieme ad una stima delle energie corrispondenti ai vari stati, arrivando ad un quadro coerente del chemisorbimento dell'anidride carbonica su Ni(110), che include anche i dati spettroscopici e teorici esistenti.

Nel processo di riduzione selettiva del monossido di azoto (SCR) quest'ultimo reagisce con l'ammoniaca per formare azoto molecolare. Il ruolo giocato da un complesso NH_3–NO nella selettività di questa reazione è stato in passato suggerito da diverse tecniche sperimentali. Questo tipo di complesso viene qui caratterizzato su scala microscopica sulla superficie (111) del platino, concentrandosi in particolare sulle interazioni intermolecolari all'origine della selettività. Vengono determinati i siti, le geometrie e l'energia di adsorbimento delle strutture derivanti dal coadsorbimento di NH_3 ed NO. In particolare, viene a formarsi uno strato ordinato con una periodicità 2×2, nel quale le due molecole sono disposte a scacchiera, in una configurazione che massimizza le interazioni reciproche. In questa struttura, l'ammoniaca adsorbe sui siti *on-top*, mentre l'NO sugli *fcc-hollow*, con una stabilizzazione di $0.29\,\text{eV}$/cella unitaria derivante dalla mutua interazione. Le energie vibrazionali calcolate sono in accordo entro il 6% con gli esperimenti riportati in letteratura, sia nel caso delle specie adsorbite individualmente, sia nel caso del complesso di coadsorbimento.

Infine, vengono dettagliate le ottimizzazione e le caratterizzazioni che sono state necessarie per utilizzare con successo la spettroscopia STM-IETS con il nostro sistema sperimentale. In particolare, viene presentato un metodo originale che permette di aumentare la risoluzione di questo tipo di misure, diminuendo l'allargamento dovuto alla modulazione. Questo, sempre presente nelle tecniche che utilizzano un amplificatore *lock-in*, viene ridotto utilizzando una funzione di modulazione *ad hoc* invece della sinusoide *standard*. Questo metodo è generale, e può essere facilmente applicato ogniqualvolta un amplificatore *lock-in* viene utilizzato per misurare una derivata seconda.

Contents

Chapter 1

Introduction

«*A* catalyst *is a substance which affects the rate of a chemical reaction without being part of its end products.*» [1]. At the beginning of 19$^{\text{th}}$ century, Wilhelm Ostwald defined the phenomenon of catalysis, which had been observed by chemists since the early 1800s, and whose technical applications would have deeply shaped the 20$^{\text{th}}$ and 21$^{\text{th}}$ centuries. Indeed, our present life would be very different without – for instance – the iron-based catalysts at the heart of the Haber process for ammonia synthesis: every year 450×10^9 kg of fertilizers are produced in this way, using for this about 1% of the world energy supply [2]. Catalysis is ubiquitous in oil refining processes, but also in the production and use of alternative energy vectors, such as hydrogen; it allows the abatement of pollutants from industrial plants as well as from motor vehicles; catalysis is involved in the 90% of the production of chemical industries [3].

In general, a catalyst increases the rate of a reaction by forming intermediate compounds with the chemical species involved. This opens new reaction paths, characterized by lower activation barriers, and correspondingly higher reaction rates. An important point is implied here: the understanding of the working principle of a catalyst involves its characterization at the atomic and molecular scale, because its activity originates form its interaction with the reactants *at the molecular level.*

In industrial processes this interaction takes most often place at the surface separating a solid catalyst from the gaseous or liquid reactants (heterogeneous catalysis), so the problem turns to the characterization of the chemistry between the species adsorbed on this surface. However real catalysts have complex structures, involving for instance nanometer-sized active particles dispersed in porous ceramic matrices. For this reason, an important route for their understanding has been the *surface science* approach, where the problem is simplified by considering model systems (well defined, single-crystal surfaces) in a controlled environment (Ultra-High Vacuum, UHV) [1]. Although this approach had been suggested by Irvin Langmuir in the 1920s, it has become possible only from the 1960s, with the development of a whole arsenal of experimental techniques, aimed at the characterization the electronic and

structural properties of surfaces [4]. Among these, the Scanning Tunneling Microscope (STM) [5] is unique in two ways: first, it eases our understanding in a "natural" way, by allowing us to actually see what is happening on the surface at the molecular scale; second, the information it provides is *local*, not surface-averaged. When employed at cryogenic temperatures, it becomes a "Swiss-Army knife" for single-molecule chemistry, allowing to image and manipulate individual molecules, inject energy and charge in a controlled fashion by means of the tunneling electrons, break or form chemical bonds, measure the electronic and vibrational properties of one molecule at a time [6].

During my PhD I applied low-temperature STM techniques to study model systems for heterogeneous catalysis, in particular in this thesis

chapter 2 introduces the scanning tunneling microscopy and describes our apparatus;

chapter 3 reports an investigation on a model system for carbon dioxide hydrogenation to methanol, describing a chemisorbed, activated CO_2 species;

chapter 4 is about the origin of selectivity in the reduction of NO with NH_3 on platinum-based catalysts.

These investigations required a combined approach, where the experimental STM data have been integrated with Density Functional Theory (DFT) calculations, part of which I personally performed. DFT, describing the ground-state properties of a system at the atomic scale, is in a certain sense the most natural complement of low-temperature STM measurements.

During my PhD I introduced for the first time in our laboratory one of the most challenging LT-STM techniques, the Inelastic Electron Tunneling Spectroscopy with an STM (STM-IETS) [7], which allows to measure the vibrational modes of one single adsorbed molecule. This is of immediate interest form the catalysis point of view: the vibrational spectrum of a molecule is not only a fingerprint of its chemical identity, but allows also to probe its interactions with the local environment.

chapter 5 introduces the STM-IETS technique, and details the key issues and optimizations that had to be tackled in order to successfully perform this kind measurements.

Among these optimizations, I discovered that it is possible to increase the resolution of phase-sensitive measurements with a lock-in amplifier by employing a tailored modulation waveform, different form the commonly-used sinusoid;

chapter 6 presents this new measurement scheme, which has a general applicability, not limited to STM spectroscopies.

References

[1] G. Ertl, *Reactions at Surfaces: From Atoms to Complexity (Nobel Lecture)*, Angew. Chem. Int. Ed. **47** (2008) 3524.

[2] V. Smil, *Enriching the Earth: Fritz Haber, Carl Bosch, and the Transformation of World Food Production*, The MIT Press, Cambridge 2004.

[3] J. Haber, *Catalysis - where science and industry meet*, Pure Appl. Chem. **66** (1994) 1597.

[4] D. P. Woodruff and T. A. Delchar, *Modern Techniques of Surface Science*, Cambridge University Press, Cambridge 1994.

[5] G. Binnig and H. Rohrer, *Scanning Tunneling Microscopy–from Birth to Adolescence (Nobel Lecture)*, Angew. Chem. Int. Ed. **26** (1987) 606.

[6] W. Ho, *Single-molecule chemistry*, J. Chem. Phys. **117** (2002) 11033.

[7] B. C. Stipe, M. A. Rezaei, and W. Ho, *Single-Molecule Vibrational Spectroscopy and Microscopy*, Science **280** (1998) 1732.

Chapter 2

Scanning Tunneling Microscopy

In this introductory chapter, the fundamental concepts of Scanning Tunneling Microscopy (STM) will be presented, in order to understand the experiments described in this thesis and to get more insight into the powerful tools provided by this technique for the characterization of atoms and molecules at surfaces. In particular, we will briefly explain how the Low-Temperature Scanning Tunneling Microscope (LT-STM) allows for characterizing the species of interest with sub-ångström resolution, investigating the electronic properties of surfaces and adsorbates and resolving individual vibrational states by inelastic tunneling.

The second part of the chapter presents the details of experimental system used throughout this thesis, briefly outlining the features which are relevant to low-temperature STM imaging and spectroscopy experiments.

2.1 Operating principle

When a metallic tip is approached to a conductive surface, a potential barrier due to the vacuum gap is present between the two objects. If a voltage bias is applied between them, and their distance is small enough, the electrons can *tunnel* across the potential barrier from the tip to the sample or vice versa, giving rise to a current flow between them, which is strongly dependent on the tip-to-sample distance. The tip is scanned over an area of the surface with sub-ångström lateral resolution and images can be obtained in the following two modes:

constant height mode: the tip is kept at a constant height while scanning, and the tunneling current I, which is recorded in every scan point, is color-coded to form the STM image $I(x, y)$ (figure 2.1a);

constant current mode: during the scan, the tunneling current is kept constant by changing the tip height z by means of an electronic feedback system, and the STM image is formed by color-coding the tip height $z(x, y)$ at every scan point (figure 2.1b).

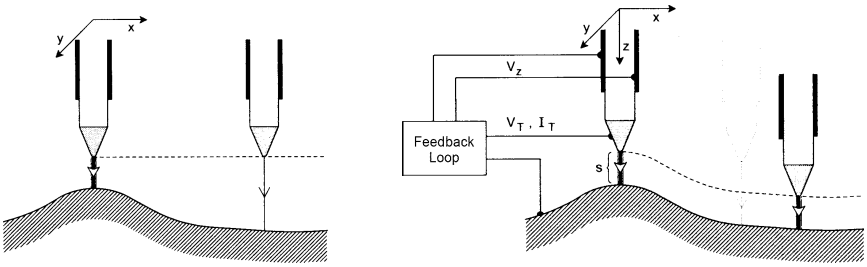

(a) Constant height (b) Constant current

Figure 2.1: The two STM imaging modes [1].

The former mode enables higher scanning speeds because no limitation is imposed by the response time of the feedback electronics, but has the critical drawback that the tip is not "protected" against accidental crashes on surface asperities. In all our experiments in this thesis we will thus use the constant current scan mode, which is the most commonly used mode.

2.2 Theory of Scanning Tunneling Microscopy

The information contained in an STM image is not simply the topography of the surface. This is easily understandable since the image contrast (i. e. the tip height) is governed by the tunneling current, which depends not only on the geometrical position of the atoms at the surface, but also on the spatial distribution and the energy of the tip/sample electronic states available for the tunneling process.

To understand the aforementioned effects involved in the formation of the STM image, we will briefly review the theoretical aspects of the tunneling process between two metal electrodes such as the tip and the sample. Needless to say, the goal of the theoretical analysis of the tunneling process is to derive the most precise approximation to the tunneling current.

2.2.1 Simple model of the electron tunneling

The tunneling of electrons between the tip and the sample across the vacuum barrier, in a first rough approximation, can be thought as a simple tunneling across a rectangular potential barrier in one dimension.

If the potential barrier has a height U, and the electron represented by the wave function $\psi(z)$ travels from the left with energy E (see figure 2.2), the time-independent Schrödinger equation of the system is:

$$-\frac{\hbar^2}{2m}\frac{\mathrm{d}^2}{\mathrm{d}z^2}\psi(z) + V(z)\psi(z) = E\,\psi(z)$$

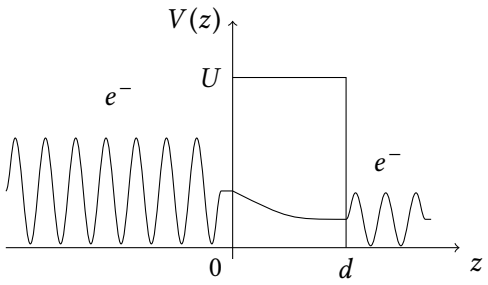

Figure 2.2: An electron impinging from the left on a one-dimensional potential barrier can cross the barrier even if $E < U$ provided the width d is small enough.

The general solution in the region $0 \leq z \leq d$ is given by:

$$\psi(z) = Ae^{-kz} + Be^{kz}$$

where

$$k = \frac{1}{\hbar}\sqrt{2m(U-E)} \tag{2.1}$$

Since the component which grows with z would have no physical meaning[1], the solution in this case is given only by the decreasing exponential component. Since the wave function must be continuous in all space, and also its derivative, one finds that in the region $0 \leq z \leq d$:

$$\psi(z) = \psi(0)\, e^{-kz}$$

By locating the sample at the $z = 0$ plane and the tip apex at $z = d$, the probability of finding the electron on the tip is proportional to the square modulus of the wave function in d:

$$w \propto \left|\psi(d)\right|^2 = \left|\psi(0)\right|^2 e^{-2kz} \tag{2.2}$$

This exponential dependence of the tunneling probability versus the tip-sample distance, as we will see below, is the physical property of the tip-sample system which enables picometer-scale resolution in the z direction, orthogonal to the sample surface.

2.2.2 Metal-vacuum-metal tunneling

If we electrically connect the tip with the sample, their Fermi energies ϵ_F will become equal. It is clear that at $T \approx 0\,\mathrm{K}$, all the states below ϵ_F will be filled, and no states will be occupied above ϵ_F. If we apply no bias voltage between them, there will be no tunneling since there are no states for the electrons to tunnel to. By biasing the sample, a net tunneling current flows: for instance, as shown in the left part

[1] The probability of finding the electron at a distance z from the $z = 0$ plane would increase with z, which is absurd in the case of an electron impinging on the barrier from the left.

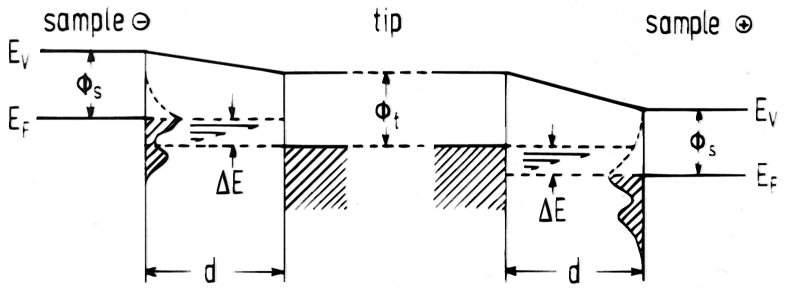

Figure 2.3: Electronic energy levels involved in tunneling. Left: tunneling from filled states in the sample to empty states in the tip (negative sample bias V); right: tunneling from filled states in the tip to empty states in the sample (positive V). Here the the shaded region schematically represents the density of electronic states in the energy $\rho(\epsilon)$, d is the sample-to-tip distance, E_F the Fermi energy, E_V the vacuum level, ϕ_s and ϕ_t the work functions of the sample and the tip, $\Delta E = e|V|$ the energy due to the sample bias voltage. Reproduced from [2].

of figure 2.3, if the sample bias is negative, an electron in a sample state ψ_n with energy E_n lying between ϵ_F and $\epsilon_\mathrm{F} + eV$, has a chance to tunnel into an empty tip state.

Let us call ϕ the work function of the metal, which is defined as the minimum energy required to extract an electron from the bulk to the vacuum level. If we neglect all temperature effects, the Fermi energy is exactly the upper limit of the occupied states in a metal; thus, within our model $\epsilon_\mathrm{F} = E_\mathrm{V} - \phi$. If we suppose that the bias is much smaller than the work function, $eV \ll \phi$, the energy of the electronic states involved in the tunneling process will be $E_n \approx -\phi$. Then the probability w for the electron in the nth sample state ψ_n to tunnel in the tip, from equation (2.2), is

$$w \propto \left|\psi_n(0)\right|^2 e^{-2kd}$$

where

$$k = \frac{1}{\hbar}\sqrt{2m\phi}$$

since from equation (2.1) $eV - \epsilon_\mathrm{F} = eV + \phi \approx \phi$. Now, in a metal there is a finite number of electronic states within ϵ_F and $\epsilon_\mathrm{F} + eV$. Thus to write an approximation for the tunneling current we must include the contributions from all these states:

$$I \propto \sum_{E_n=\epsilon_\mathrm{F}-eV}^{\epsilon_\mathrm{F}} \left|\psi_n(0)\right|^2 e^{-2kd} \tag{2.3}$$

If V is sufficiently small, then the sum in equation 2.3 can be replaced with the local density of states (LDOS) at the Fermi level. The LDOS is the number of electrons per unit volume per unit energy at a given point in space and at a given

energy: at a distance z from the sample, the LDOS at the energy E is defined as

$$\rho_S(z, E) \equiv \frac{1}{\varepsilon} \sum_{E_n = E-\varepsilon}^{E} \left|\psi_n(z)\right|^2 \tag{2.4}$$

for a sufficiently small ε. By using this expression for the LDOS, the current can be rewritten as [3]:

$$I \propto V \rho_S(0, \epsilon_\mathrm{F})\, e^{-2kd} \tag{2.5}$$

$$\approx V \rho_S(0, \epsilon_\mathrm{F})\, e^{-1.03\sqrt{\phi}\, d} \tag{2.6}$$

If we consider a typical metal work function $\phi \approx 4\,\mathrm{eV}$, then we obtain the typical value of the decay constant $k = 1\,\mathrm{Å}^{-1} = 10\,\mathrm{nm}^{-1}$. This gives an estimate of the rate of change of the current with the distance: the current increases by a factor of 3 when the distance changes by one Bohr radius ($\Delta d = 53\,\mathrm{pm}$). Equation (2.6) indicates two important facts: according to this model, equation (2.6) shows that an STM image is a Fermi level LDOS contour of the sample surface. Secondly, the tunneling current is extremely sensitive to very small differences in the tip-sample distance, and this property accounts for the fact that the STM can follow the corrugation of single atoms while scanning above the surface [3].

In 1961, well before the invention of the scanning tunneling microscope, Bardeen [4] developed an extension of the one dimensional tunneling problem to the three dimensional case. Instead of solving the complicated Schrödinger equation for of the entire metal-insulator-metal system, his approach was to initially solve it for two electrodes as separate entities and then calculate their overlap by using the Fermi golden rule. What he calculated is the M matrix element, i. e. the probability of tunneling from a state ψ, on one side of the barrier, to a state χ on the other side [3]:

$$M = \frac{\hbar}{2m} \int_{z=z_0} \mathrm{d}S\; \chi^* \frac{\partial \psi}{\partial z} - \psi \frac{\partial \chi^*}{\partial z}$$

where $z = z_0$ is a separation surface lying entirely within the two electrodes.

Following Bardeen's approach, by determining the rate of electron transfer between the two states with the Fermi golden rule and by assuming that $k_\mathrm{B}T$ is small enough to approximate the Fermi distribution with a step function, we obtain the following expression for the tunneling current [3]:

$$I = \frac{4\pi e}{\hbar} \int_0^{eV} \mathrm{d}\epsilon\; \rho_S(\epsilon_\mathrm{F} - eV + \epsilon)\; \rho_T(\epsilon_\mathrm{F} + \epsilon)\; |M|^2 \tag{2.7}$$

Eventually, if the M matrix is assumed to be almost constant within the range of interest, we obtain a final, simplified expression for the tunneling current:

$$I \propto \int_0^{eV} \mathrm{d}\epsilon\; \rho_S(\epsilon_\mathrm{F} - eV + \epsilon)\; \rho_T(\epsilon_\mathrm{F} + \epsilon) \tag{2.8}$$

Therefore the tunneling current, within Bardeen's extension of the one-dimensional tunneling problem, is not only a constant LDOS contour at the Fermi level, but rather a convolution of the density of states (DOS) of two electrodes.

2.2.3 Scanning tunneling spectroscopy

At this point, we can exploit Bardeen's formalism to understand how the STM can also provide information about the electronic properties of samples and adsorbates by scanning tunneling spectroscopy (STS) [5, 6].

As can be understood from figure 2.3, by changing the applied voltage V it is possible to select the electronic states involved in the tunneling process. At a given voltage V, the tunneling current in Bardeen's approximation is given by equation (2.8).

If the tip is assumed to have a constant DOS, then the first derivative of the tunneling current gives:

$$\frac{\mathrm{d}I}{\mathrm{d}V} \propto \rho_S(\epsilon_\mathrm{F} - eV)$$

and thus it is possible to probe the DOS of the sample, or molecular states close to the Fermi level, through the tunneling current conductance.

Since the tunneling current exhibits a dramatic dependence on the tip-sample separation, STS data need to be normalized for comparison. The commonly used normalization is the one proposed by Feenstra and Stroscio [7]:

$$g_N(V) \equiv \frac{\mathrm{d}\ln I}{\mathrm{d}\ln V} = \frac{\mathrm{d}I}{\mathrm{d}V} \cdot \frac{V}{I}$$

called *normalized dynamic conductance*.

The achievable resolution in the $\mathrm{d}I/\mathrm{d}V$ spectra is strongly temperature dependent: the overall energy broadening from the Fermi distribution of the tip and the sample states around the Fermi energy is about $4\,k_\mathrm{B}\,T$, that at room temperature gives about 100 meV and 1 meV at 4 K [3]. Thus in order to perform STS with high energy resolution is necessary to work at low temperatures. Moreover, working at low temperatures guarantees optimum stability of the tip position (thanks to the reduced thermal drift) during the time required for the spectra acquisition, i. e. tens of seconds or more.

To acquire $\mathrm{d}I/\mathrm{d}V$ spectra, a lock-in amplifier is commonly used to recover the signal of interest from the background noise. In particular, the first harmonic of the lock–in output is recorded, which directly gives the first derivative of the tunneling current. The STS measurements can be either acquired in point mode, i. e. above a feature of interest, as a function of the voltage, or in laterally resolved mode at a fixed voltage V_b. In the first case, during a typical point mode STS, the tip is moved to a point of interest on the surface, then the feedback loop is switched off and the voltage is ramped while recording the signal from the lock-in amplifier. In the second case, the acquisition of STS images, also called continuous imaging tunneling spectroscopy (CITS), is similar to the STM topography imaging, but maps the $\mathrm{d}I/\mathrm{d}V|_{V=V_b}$ signal instead of the tip height. Notice that since the lock-in amplifier

usually requires an integration time of the order of 30 ms or more per image point, the acquisition time of STS images is much longer than normal STM images (unless the number of points is reduced).

When characterizing molecules adsorbed at surfaces, however, there are a number of limitations in employing the STS technique. First of all, occupied states of the sample which lie at the upper range of the energy window ΔE available for the tunneling process, represented in figure 2.3, contribute more significantly to the tunneling current (as shown by the arrows) since the barrier height seen by these states is lower. Conversely, low-lying states (i. e. far below the Fermi level of the sample) have little contribution to the tunneling current. Therefore, the sensitivity of STS to occupied sample (or adsorbate) states rapidly decreases with increasing energy below ϵ_F [8].

Secondly, the allowed range of the electron energies (i. e. gap voltages) is within ±4 eV and ±5 eV since in this limit we approach the typical work function of one of the two metals, where field emission occurs. However, as has been shown by photoemission spectroscopy experiments, interesting features expected for adsorbates often appear out of this range [9]. The range is often further limited by other processes, for instance by molecular dissociation that can occur due to vibrations induced by inelastic tunneling processes, at voltages well below the field emission limit. Third, with STS a chemical identification of the molecules requires the support of theoretical calculations [9].

A more direct chemical information is instead provided by Inelastic Electron Tunneling Spectroscopy (STM-IETS), which allows to access the vibrational modes of an adsorbed molecule by measuring the $\mathrm{d}^2I/\mathrm{d}V^2$ characteristic of the tunneling junction. Part of my PhD was devoted to introducing for the first time in our laboratory this technique, which will be presented in detail in chapter 5.

2.3 The experimental system

The experimental system is based on a commercial Omicron LT-STM with a dedicated Ultra High Vacuum (UHV) chamber, and complemented by a preparation chamber designed and assembled by our group. I will recall here the main characteristics of this setup, referring to [10] for a thorough description.

2.3.1 The microscope

The Omicron LT-STM head (figure 2.4b) is a single-tube STM: a piezoelectric hollow cylinder, where the tip is fixed at the top, is covered with four electrodes which split the cylinder in four quadrants. By applying suitable voltage difference between the quadrants and the inner electrode, the piezoelectric cylinder can be bent in order to scan the tip laterally onto the sample (xy plane) with sub-ångstrom resolution. Moreover, the tip can be moved orthogonally to the sample surface (z direction) with a voltage difference applied between the inner and the outer surface of the cylinder. In normal scanning conditions the constant current mode is used: during

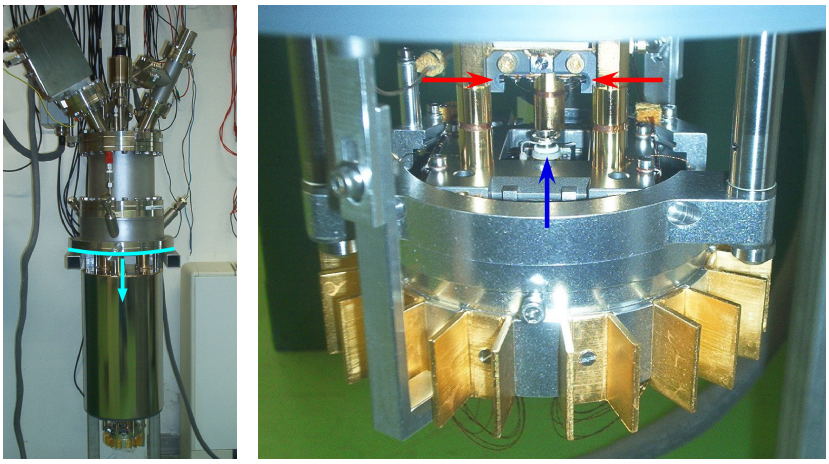

(a) (b)

Figure 2.4: (a) shows the whole LT-STM assembly: the out-of-vacuum part (top part) with the electrical feedthroughs; the blue line indicates the mounting flange and the STM head is visible at the bottom; (b) Close-up of the STM head with the slits for inserting and fixing the sample (red arrows) and the top part of the piezoelectric cylinder (blue arrow) where the STM tip is to be fixed.

the lateral scan, the current is kept constant by using a feedback loop, which changes the z position of the tip in order to follow the local corrugation of the sample (see section 2.1).

2.3.2 Low-temperature setup

This LT-STM can ideally operate at any sample temperature between 2.5 K and room temperature (RT). The cooling system is made up of two concentric cylindrical cryostats below which the STM head is fixed. In order to cool the sample below RT the external cryostat has always to be filled with liquid nitrogen (LN_2), while the inner cryostat can be filled with LN_2 (boiling at 77 K) or liquid helium (LHe) (boiling at about 4.2 K) according to the desired temperature, as described in table 2.1. All the intermediate temperatures can be reached by means of a resistive heater located near the sample stage and powered by a PID temperature controller. The temperature is measured by means of a silicon diode installed behind the sample stage. If no counter-heating is applied, the STM can be kept at 4 K for 24 h before having to refill the inner cryostat.

To reach temperatures as low as 4 K at the sample, the STM head is surrounded by a double shielding mechanism (figure 2.5), in order to prevent external electromagnetic radiation from limiting the cooling power. The internal shield (figure 2.5(a)) is firmly bolted to the base of the LHe cryostat at a temperature close to 4 K, thus providing a thermal bath to the STM head. The external shield (figure 2.5b) is

Table 2.1: Operating temperatures of the LT-STM with the respective cooling methods.

T range [K]	Coolant (inner cryostat)
2.5 ÷ 4	pumped LHe
4 ÷ 55	LHe
55 ÷ 77	pumped LN_2
77 ÷ 300	LN_2

(a) The internal 4 K shield (b) The external 77 K shield

Figure 2.5: The LT-STM radiation shielding: (a) the inner shield which is tightly bolted on the base of the LHe cryostat to ensure a 4 K thermal bath around the STM head; (b) the outer shield is fixed to the base of the LN_2 cryostat.

fixed firmly against the base of the LN_2 cryostat, close to 77 K.

2.3.3 Mechanical isolation

One of the most important issues in STM measurements is the performance of the mechanical vibrations isolation system. As a matter of fact, since atoms exhibit corrugations of roughly 1 pm to 10 pm, it is critical to have an excellent mechanical stability of the tip-sample junction: periodic instabilities of the order of 100 pm, for instance, would not be acceptable. This issue gains even more importance when exploiting the unique characterization techniques of the LT-STM. For instance, a very precise tip positioning and stability on the time scale of hours is required to perform repeated and reliable inelastic tunneling spectroscopy measurements. For this mechanical isolation purpose, the STM head can be suspended below the cryostat by means of three springs. Moreover, an eddy current damping system, described hereafter, provides effective, smooth damping of possible, very low frequency instabilities. The STM head is mounted on a circular plate which is surrounded by copper alloy "U"s (see figure 2.4(b)) that are centered within radially distributed

small magnets, fixed on the inner part of the internal radiation shield. If the STM stage moves, the movement of the copper conductors within the magnets induces eddy currents in the copper alloy, which in turn build up magnetic fields that tend to counteract the initial movement of the STM plate.

2.3.4 Measurement and control electronics

The control unit (CU) provides the real-time feedback loop and the appropriate voltage signals to drive the tip during then scan process, and is one of the most important components of STM systems: both its performance and reliability influence the quality of the images in terms of noise level and stability, and determine the complexity of the experimental techniques which can be used. The Omicron LT-STM is shipped with a dedicated control hardware and software, the MATRIX SPM Control System. The CU is composed by different digital hardware boards, linked to a PC that runs the control software where the user can control the relevant parameters for the imaging process (gap voltage, tunneling current, scan size, scan speed, ...). The main advantages of the MATRIX control system are the high resolution – 20 bit at 62.5 kHz– of the digital-to-analog converter (DAC) which drives the z position of the tip, and the high-quality analog-to-digital converter (ADC) sampling the tunneling current signal (16 bit, 400 kHz).

The tunneling current is measured by a current amplifier mounted outside the vacuum vessel. The MATRIX system is shipped with the Omicron PRE4 transimpedance amplifier, having a gain of 3×10^7 V/A at a bandwidth of 40 kHz, or 3×10^9 V/A at 0.8 kHz. During my PhD, it was replaced by a customized version of the commercial Femto DLPCA-200, chosen for its superior noise performance. This versatile instrument is capable of gains ranging from 10^3 to 10^{11} V/A; the settings useful for STM operation are reported in table 5.1 at page 83.

2.3.5 UHV system

The whole LT-STM assembly is designed to be mounted from the top flange of the dedicated UHV chamber, where a port aligner is interposed between the microscope assembly and the chamber in order to allow for the alignment of the STM head inside the eddy current vibration damping system (see section 2.3.3). The chamber is equipped with a carousel where tips and samples can be temporarily stored, retrieved and inserted into the LT-STM by means of a wobblestick. To prevent stray radiation from increasing the final sample temperature, the windows for optical access of the chamber are IR filtered.

A gate valve separates the STM chamber from the sample preparation chamber. The latter is structured around an horizontal manipulator, used to transfer sample and STM tips between the two chambers, and to position these in front of the various instruments. On the manipulator, the sample can be heated to 1300 K via filament heating and electron bombardment, or cooled to 90 K via LN_2 circulation.

The facilities available at present on the preparation chamber, indicated in figure 2.6, are:

- a sputter gun, needed in order to clean the samples by bombardment with noble gases;
- a quadrupole mass spectrometer;
- a fast-entry lock system, providing a quick way to insert and extract samples and STM tips from the preparation chamber without breaking the vacuum;
- a Low Energy Electron Diffraction (LEED) system, for a quick structural characterization of the samples prior to the insertion in the STM;
- different types of molecule and metal evaporators;
- a quartz balance for deposition rate monitoring;
- a gas line, allowing to dose various gases in the chamber background;

The vacuum is maintained by a 500 l/s ion pump in the STM chamber, whereas the preparation chamber is pumped by a magnetically-levitated turbo pump (450 l/s) together with a smaller ion pump (240 l/s) equipped with a titanium sublimation cartridge and a liquid nitrogen cooled cryopanel. The base pressure in the preparation chamber varies between 1×10^{-8} Pa and 2×10^{-8} Pa, whereas the radiation shields of the STM act as cryo-pumps, ensuring a local lower pressure at the STM head.

References

[1] G. Binnig and H. Rohrer, *Scanning Tunneling Microscopy - from birth to adolescence*, *Nobel lecture*, 1986.

[2] R. Behm and W. Hösler, *Chemistry and Physics of Solid Surfaces*, ed. by R. Vanselow and R. Howe, vol. IV, Springer, Berlin 1986.

[3] C. J. Chen, *Introduction to scanning tunneling microscopy*, Oxford University Press, 1993.

[4] J. Bardeen, *Tunnelling from a Many–Particle Point of View*, Phys. Rev. Lett. **6** (1961) 57.

[5] R. Feenstra, *Scanning tunneling spectroscopy*, Surf. Sci. **299–300** (1994) 965.

[6] R. Hamers, *Atomic-Resolution Surface Spectroscopy with the Scanning Tunneling Microscope*, Ann. Rev. Phys. Chem. **40** (1989) 531.

[7] R. Feenstra and J. Stroscio, *Real-space determination of surface structure by scanning tunneling microscopy*, Physica Scripta **T19** (1987) 55.

[8] J. Wintterlin and R. Behm, *Scanning Tunneling Microscopy*, ed. by H.-J. Güntherodt and R. Wiesendanger, vol. I, Springer, Berlin 1992.

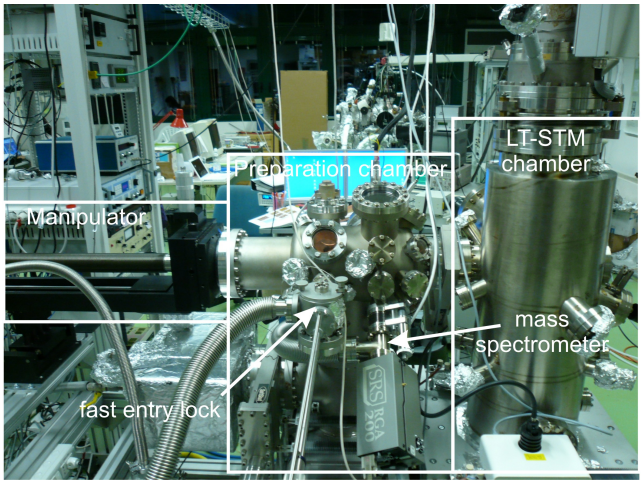

(a)

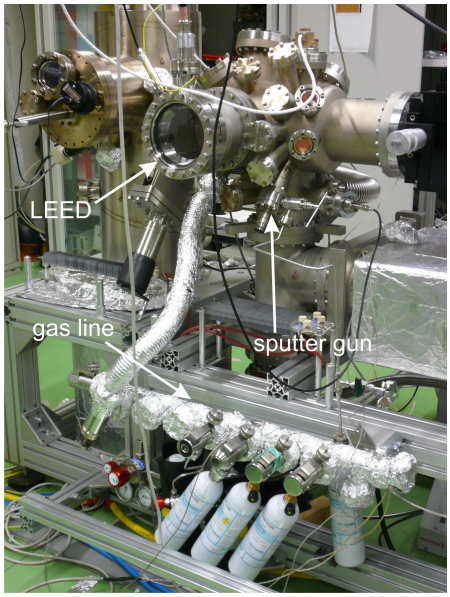

(b)

Figure 2.6: Two opposite views of the preparation chamber, showing the position of the various instruments.

[9] T. Komeda, *Chemical identification and manipulation of molecules by vibrational excitation via inelastic tunneling process with scanning tunneling microscopy*, Prog. Surf. Sci. **78** (2005) 41.

[10] C. Dri, *Characterization and manipulation of single molecules and molecular complexes by Low Temperature Scanning Tunneling Microscopy*, PhD thesis, Dottorato di ricerca in Nanotecnologie – Università degli Studi di Trieste, 2008.

Part I

Model systems for heterogeneous catalysis

Chapter 3

Characterization of the activated CO_2 species on Ni(110)

The chemistry of carbon dioxide has become of great interest both for technological and environmental issues. Indeed, carbon dioxide is one of the most problematic greenhouse gases and many efforts are presently dedicated to reduce its concentration in the atmosphere by limiting the emissions from fossil-fueled plants and vehicles [1–3]. This molecule is also a fundamental ingredient for the industrial catalytic organic synthesis of many compounds like, for example, methanol, which is used as a high energy density vector in direct methanol fuel cells. Alternative methanol-based economies have been recently proposed, exploiting the great availability of CO_2 from the atmosphere [4]. Motivated by this interest, in the last years many efforts in the field of surface science have been devoted to the characterization of the interaction of CO_2 with model catalyst surfaces [5].

Recent investigations have shown that, while the common industrial process for methanol synthesis is carried out on Cu-based supported catalysts [6], the addition of Ni to a Cu model catalyst yields a 60-fold increase in the rate of methanol production [7–9]. The peculiar reactivity of Ni for CO_2 hydrogenation with respect to other transition metals has been ascribed to the different adsorption mechanism of CO_2. In a previous joint experimental and numerical investigation [10, 11] we have firstly characterized the adsorption of CO_2 on the Ni(110) substrate, ascribing the observed features in the high resolution electron energy loss (HREEL) spectra to the presence of two chemisorbed configurations beside the physisorbed state, which is commonly observed on other transition metal surfaces. Secondly, we have investigated the hydrogenation mechanisms, unveiling that the chemisorbed species were the key for both Langmuir-Hinshelwood and Eley-Rideal hydrogenation steps [12, 13]. Shedding light onto the role of the Ni substrate, we found that the transfer of almost one electron from the metal to the molecule in the chemisorbed state yields an activated precursor for the reaction with hydrogen, thus explaining the peculiar activity of Ni in this case.

While the details of the CO_2 hydrogenation reaction have been thoroughly char-

acterized, a direct, local evidence supporting the assignment of the adsorption sites and geometries of the activated, chemisorbed CO_2 state is still lacking. Indeed, the identification of the adsorption configurations was based solely on a comparison between the HREEL vibrational frequencies and their estimated values obtained from density functional theory (DFT) calculations.

Here we provide single-molecule imaging of CO_2 on Ni(110). Experimental low temperature scanning tunneling microscopy (LT-STM) data are interpreted by comparison with simulated DFT images, thus providing direct information for the adsorption geometries. To our knowledge, these are the very first STM images with sub-molecular resolution of single carbon dioxide molecules in a chemisorbed state, while only physisorbed CO_2 has been previously imaged [14]. From the theoretical point of view, for the characterization of such weakly bound, closed-shell molecules, which is well known to be a demanding task, we had to improve standard DFT calculations with the inclusion of dispersion forces and zero point energies (ZPE). By means of this approach we present a complete characterization of the different adsorption geometries and we refine the previous assignment of the vibrational modes.

This work, where I contributed most of the STM measurements, has been published as [15].

3.1 Methods

The Ni(110) sample (MaTecK GmbH) was preliminarily treated at 1000 K in a hydrogen-flux furnace for 12 h at 10^5 Pa in order to reduce the concentration of contaminants like carbon and sulfur. The sample was then transferred into the UHV system, where it was initially cleaned by standard Ar^+ sputtering (1 keV at room temperature) and prolonged annealing (1100 K) cycles. Repeated oxidation and reduction treatments were performed to further reduce carbon contamination. Once the sample crystalline ordering and cleanness were confirmed by low-energy electron diffraction (LEED) and STM, the routine daily cleaning procedure consisted of a single sputtering and annealing cycle (1000 K). Carbon dioxide (SIAD, purity 99.998%) was dosed on the Ni sample by backfilling of the preparation chamber through a leak valve (p_{CO_2} in the 10^{-7} Pa range).

The theoretical calculations were performed within the framework of the DFT in the spin polarized generalized gradient approximation (σ-GGA) using the Perdew-Burke-Ernzerhof implementation [16], if not otherwise specified. We used the plane-waves-based PWscf and PHonon codes of the Quantum ESPRESSO (QE) distribution [17] with publicly available ultrasoft pseudopotentials.[1] Most of the technicalities are the same of references [10, 12, 13] and we report here only the details that are different or relevant to the present results. The previous analysis of the local energy minima for chemisorption was significantly improved by accounting also for the van der Waals contribution using a semi-empirical addition of dispersive forces

[1] Ultrasoft pseudopotentials from the publicly available Quantum ESPRESSO table are used: `Ni.pbe-nd-rrkjus.UPF`, `O.pbe-rrkjus.UPF`, `C.pbe-rrkjus.UPF`, and `H.pbe-rrkjus.UPF`

to conventional density functionals in the framework of the DFT-D approach [18], implemented in the QE suite.

We used slab geometries to simulate CO_2 adsorption and in particular supercells with a 3×3 in-plane periodicity and one CO_2 molecule, corresponding to a coverage of $1/9$ ML,[2] to simulate the adsorption of individual molecules. Larger supercells were used to test the strength of lateral interactions between repeated images of individually adsorbed molecules. Supercells with 4×4 and 5×5 in-plane periodicity were used to describe molecules adsorbed in pairs and triplets. At variance with our previous approach, we performed supercell "single-side" calculations in order to avoid fictitious interactions between adsorbates facing from the opposite sides of repeated slabs. We checked that a five layer Ni slab plus a vacuum space of three times the slab thickness is enough to almost entirely screen the fictitious electric field in the supercell due to the asymmetry of the finite system in the direction perpendicular to the surface, so that no dipole correction was needed. The central Ni layer was kept fixed and all the other atomic positions were fully relaxed. In order to estimate the relevant energy barriers for adsorption and diffusion, we used the nudged elastic band method (NEB) [19], relaxing the images in the paths until the forces orthogonal to the path were below 0.5 eV/nm. For the quantitative evaluation of the vibrational modes and frequencies, only the adsorbed molecules and the first layer of the slab were allowed to vibrate. The STM images are calculated from the local density of states (LDOS) using the Tersoff-Hamann approach [20]. In order to reproduce the constant current mode used in the experiments, we consider LDOS isosurfaces lying mainly between 0.3 nm and 0.6 nm from the surface, and map their heights with a linear scale.

3.2 Results

3.2.1 STM images

An STM image of the surface after exposing the Ni sample to 0.17 L of CO_2 at $T = 110$ K is shown in Figure 3.1 (upper left panel). Two different species adsorbed along the Ni troughs, a bright and a dim one, are clearly distinguishable. Close inspection of several experimental images indicates that the dim species are characterized by a dark halo, symmetric with respect to the underlying Ni atomic troughs, whereas the halo of the bright species is symmetric with respect to an axis rotated by about $\pm 45^\circ$ from the the [001] direction. While the dim molecules can be found as single, isolated units (figure 3.1c), the bright molecules appear only within characteristic complexes of 2 (figure 3.1b) or 3 (figure 3.1a) molecules. The 2-molecule unit is formed by a bright and a dim species, and is arranged so that the dimer axis forms an angle of about $\pm 45^\circ$ with respect to the atomic rows. The 3-molecule unit is formed by two bright and one dim species, arranged in a V-shaped fashion with the vertex pointing along the $[1\bar{1}0]$ (as in figure 3.1a) or along the [001] direction.

[2] One monolayer (1 ML) corresponds to one molecule per each Ni substrate atom

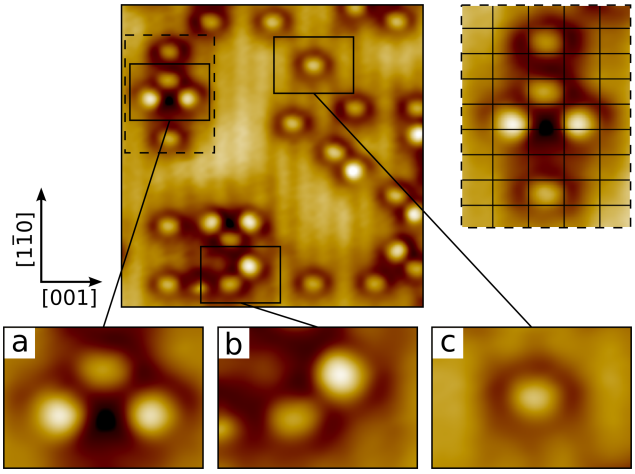

Figure 3.1: STM image (top left, 5.2 nm × 5.2 nm) of CO_2 (0.05 ML coverage) adsorbed on Ni(110) at 110 K. Two non-equivalent CO_2 species can be distinguished from their apparent height. Close-ups (1.4 nm × 1.0 nm) of the 3-molecule (a), the 2-molecule (b), and the single molecule units (c) are shown in the bottom row. In the dashed line inset (top right, 1.6 nm × 2.2 nm) the crossing points of the grid correspond to the positions of the substrate Ni atoms. (sample bias $V = -10$ mV, tunneling current $I = 1$ nA).

In the images, the bright species appears (18 ± 6) pm higher than the dim species; furthermore, it is characterized by a different position with respect to the substrate unit cell. This can be seen on the dashed-line inset in figure 3.1, where a calibrated grid, with the crossing points of the vertical and horizontal lines corresponding to the positions of the surface Ni atoms, has been superimposed. Close inspection of the experimental STM images allowed us to infer that both species are adsorbed in hollow sites but with different geometry: the dim species is adsorbed symmetrically at the center of the unit cell, while the bright species appears slightly shifted off-center towards one of the Ni atoms at the corners of the unit cell. While the registry of the substrate could be easily assigned in the [001] direction since the atomic rows are clearly resolved in the images, the assignment in the [1$\bar{1}$0] direction involved matching the grid of the atomic positions with substrate defects (e. g. Ni single vacancies).

To investigate the relative stability of the two species, different sample preparations with varying CO_2 coverage have been characterized by STM imaging. From image counting statistics, the coverage of the two species as a function of the total CO_2 coverage has been obtained and is shown in figure 3.2. For coverage values higher than 75×10^{-3} ML, the imaging conditions become very unstable due to the appearance of a very weakly bound CO_2 species which strongly interacts with the STM tip. The latter species can be attributed to the physisorbed state, which was previously reported [10]. No further information can be drawn about its adsorption

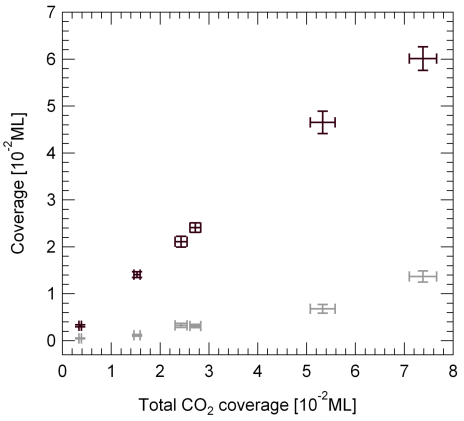

Figure 3.2: Coverage of the dim (black) and the bright (gray) CO_2 species on Ni(110), as a function of the total CO_2 coverage.

Table 3.1: Calculated energies (in eV) for the adsorption states of CO_2 on Ni(110) predicted by DFT in a 3×3 in-plane periodic supercell. Columns from left to right refer to adsorption energies within standard GGA, DFT-D-corrected GGA, DFT-D-corrected GGA plus ZPE contribution.

states	GGA	DFT-D	DFT-D + ZPE
HU	0.24	0.66	0.73
HU-s	0.19	0.60	0.69
SB	0.17	0.52	0.58
HS	0.09	0.50	0.58
phys.	0.06	0.29	0.29

properties since there was no way to image this species in a stable condition.

3.2.2 DFT calculations

The experimental STM imaging has been complemented by a thorough investigation of the possible chemisorption geometries with an extensive search for local energy minima.

Our present calculations predict the existence of two new stable configurations, the "hollow-up symmetric" (HU-s) and the "hollow-symmetric" (HS), both positioned at hollow sites, in addition to those previously found which were indicated as "hollow-up" (HU) and "short-bridge" (SB) [10]. All the predicted adsorption configurations are shown with ball models in the bottom rows of figure 3.3.

The HU configuration exhibits a dominant carbon coordination with Ni and oxygen atoms pointing upward and the molecular plane inclined with respect to the Ni surface normal [10]. The HU-s is very similar, but with one of the two C–O

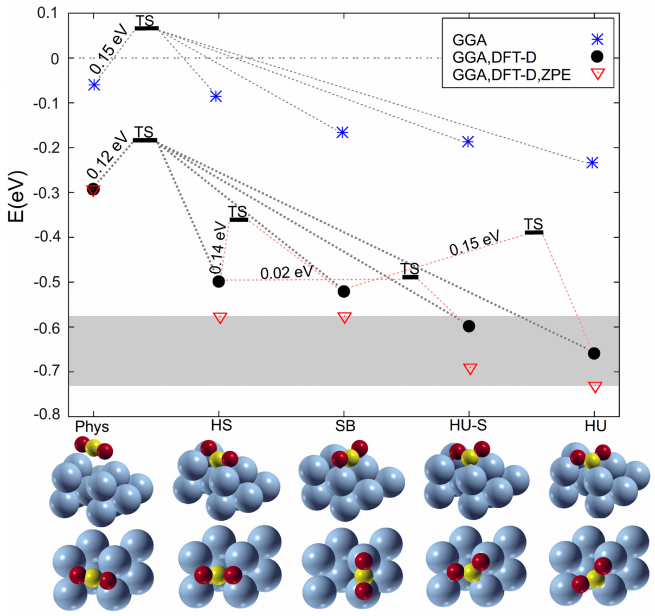

Figure 3.3: Energy diagram for different CO_2 adsorption configurations on Ni(110) and relevant adsorption and diffusion barriers, calculated using DFT both with standard GGA and with DFT-D-corrected GGA. DFT-D energies including the ZPE contributions are also reported. The shaded region highlights the energy range of all the chemisorbed configurations in the latter approximation. The zero of the energy is set to the non-dissociated molecule at infinite distance from the surface. The bottom rows depict the ball models of all the stable CO_2 configurations; only Ni atoms of the two outer layers are shown, but a five-layer thick slab was used in the calculations.

Table 3.2: Calculated geometries and charge transfer for the adsorption states of CO_2 on Ni(110) predicted by DFT in a 3×3 in-plane periodic supercell. Columns from left to right refer to distance between the carbon atom and the Ni plane (h_C); C−O bond length(s) (d_{C-O}); O−C−O angle (α_{O-C-O}); charges in standard GGA (q). DFT-D-corrected values are indicated in brackets when different from GGA results.

states	h_C [pm]	d_{C-O} [pm]	α_{O-C-O} [deg]	q [$\lvert e \rvert$]
HU	137	128	126.0	−0.93 (−0.85)
HU-s	123	132/127[a]	121.7	−0.97
SB	173	123	140.7	−0.63 (−0.58)
HS	95	130	121.9	−1.00
phys.	345 (276)	117	179.9	0

[a] In the HU-s state the two oxygen atoms are non-equivalent.

bonds in a more symmetric position, with the oxygen atom coordinated with two surface Ni atoms. The HS configuration is even more symmetric, having a mirror plane parallel to the long-bridge [001] direction and is characterized by a weaker adsorption energy.

In all chemisorbed configurations the molecule is charged and distorted with respect to the linear gas phase geometry. Adsorption energies calculated with different approximations are shown in figure 3.3 and table 3.1, whereas structural parameters and charges are summarized in table 3.2.

As already commented in reference [10], the σ-GGA approximation does not take into account the dispersion forces and usually underestimates adsorption energies. The DFT-D correction systematically gives higher adsorption energies for the chemisorbed configurations by about 0.4 eV with respect to the values obtained with standard GGA. Tests for HU and SB using both local density approximation (LDA) and GGA indicate that the corrected DFT-D estimates are almost in between GGA and LDA results and give the same relative stability for the chemisorbed configurations. DFT-D results are instead clearly different from GGA for the weakly bound, metastable state representing a physisorbed configuration: the DFT-D calculations provide a clear indication of the existence of a local energy minimum characterized by an adsorption energy of about 0.3 eV (instead of the 0.06 eV within standard GGA) [10] and a distance from the surface smaller than 0.3 nm (instead of about 0.4 nm in GGA).

A further refinement of the adsorption energies can be obtained by including an estimate of the ZPE correction to the total energies of the adsorbed configurations. The ZPE can be calculated as the sum of the vibrational frequencies divided by two. Since the ZPE correction for the isolated, linear, gas phase molecule is larger than for the adsorbed configurations, the net result is an additional energy shift towards lower energies for the chemisorbed configurations. The resulting picture is a set of four different possible adsorption configurations lying within an energy range of 0.15 eV (i. e., about 20%) around an average value of 0.65 eV (shaded region in figure 3.3). Since the numerical uncertainty on the energies (due to supercell size, slab and vacuum thickness, kinetic energy cutoff, special k-point set for Brillouin zone sampling) is of the order of 0.02 eV, but the uncertainty due to physical approximations could be up to one order of magnitude larger and therefore comparable with such range, the four configurations should be considered almost energetically equivalent. The most relevant difference among them is related to the charge transfer (q) and to the height of the C atom from the Ni surface (h_C), which are respectively the smallest and the largest in the case of SB (see table 3.2). Since the relative stability and the geometries of the chemisorbed configurations are practically unchanged in the different approximations used, it is reasonable to refer to the DFT-D and ZPE corrected GGA values as to the most reliable estimates of the energies, and keep the standard GGA approach for investigating vibrational properties and simulating STM images.

In order to account for the possible contribution of kinetic effects, which can play a relevant role in the adsorption process considering the small differences in

Table 3.3: Calculated vibrational energies (in meV) of the various chemisorption geometries.

mode	HU	HU-s	SB	HS	phys.	expt.[a]
asymmetric stretch	173	166	216	164	287	168
symmetric stretch	136	123	140	134	160	141
bending	88	87	80	86	79	81–90
hindered rotation	50	46	63	50	78	–
external stretch	44	42	39	42	25	46

[a] Experimental results from reference [10].

the predicted adsorption energies, we have also calculated with DFT-D the relevant adsorption and diffusion barriers that turn out to be similar to those predicted by GGA: therefore, the overall picture of the energetics given by DFT-D is similar to GGA, but with an almost rigid energy shift. At variance with standard GGA calculations [10], DFT-D predicts that the chemisorption processes are non-activated. In this case, the adsorption energies calculated within the DFT-D framework for the physisorbed and the chemisorbed states (0.29 eV and $\approx$ 0.65 eV, respectively) can be directly compared with the desorption energy experimental values obtained by temperature programmed desorption experiments [10], 0.26 ± 0.15 eV and 0.60 ± 0.15 eV, respectively. The comparison gives excellent agreement. Despite the prediction of a non-activated adsorption mechanism, preliminary STM measurements suggest that when dosing CO_2 at very low temperatures (i. e. about 10 K), it is not possible to form any of the chemisorbed states, but only the physisorbed state appears. This result can be reconciled in consistent picture of the energetics by assuming that the metastable physisorbed state is trapped after dissipating the energy from the gas phase through non-adiabatic processes [21].

Lateral interactions, coverage and ordering effects have also been investigated, performing tests using GGA for HS configurations in different supercells: in a 4×4 supercell rather than in the usual 3×3 supercell and also in a 2×4 and a 4×2 supercell (1/8 ML), the latter simulating the alignment along the $[1\bar{1}0]$ and [001] direction, respectively. The variations of the HS adsorption energy in the different cases are comparable with the numerical error, thus indicating no significant lateral interactions when two molecules are separated by more than 0.5 nm and no ordering trend, consistent with the fact that no clear surface ordering in the CO_2 adlayer is observed.

The calculated vibrational frequencies for the four stable configurations are shown in table 3.3 and compared with the experimental data already reported in reference [10].

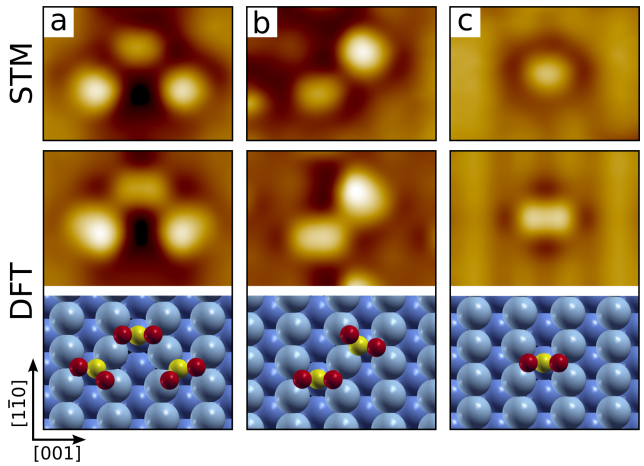

Figure 3.4: Close-ups from figure 3.1 showing the experimental (top row) and DFT calculated (middle row) STM images of the 3-molecule (a), the 2-molecule (b) and the single molecule units (c). The bottom row shows ball models of the calculated geometries of the three units.

3.2.3 Discussion

On the basis of our DFT results, we have simulated the STM images of all the four predicted chemisorption configurations for the isolated molecule and several 2- or 3-molecule complexes.

A systematic comparison between the experimental images and the calculated adsorption geometries, with careful attention to the alignment of the symmetry axes with respect to the crystallographic directions of the Ni substrate, indicates that the dim species corresponds to the HS configuration and the bright species to the HU-s or HU configuration. On the basis of this attribution, a remarkable agreement is obtained when comparing the experimental and simulated images shown in figure 3.4.

In the 3- or 2-molecule complexes (figure 3.4(a), (b)), one molecule clearly corresponds to HS. The other(s) could be either HU or HU-s, since the simulated STM images in the two cases appear almost identical (HU-s was used for the simulated images shown). The only difference is a very small mutual attractive interaction (about 0.05 eV) for the HS+HU-s pair with respect to the sum of the individually adsorbed molecules, at variance with the HS+HU configuration. The triplet configuration is particularly stable, with an energy gain of about 0.2 eV with respect to the sum of the three molecules adsorbed apart, both considering HU or HU-s. The simulated images of pairs and triplets show very clearly a deep depression in between the adsorbed molecules of the complexes, closely resembling the experimental pattern.

DFT simulations allow us to infer that the dark halo surrounding the isolated molecule, as well as the darker regions in the complexes, are originated by the elec-

tron transfer from the neighboring surface Ni atoms to the adsorbed molecules (see table 3.2).

With concern to the energetics of the adsorbed species, it is clear from figure 3.2 that the experimentally most common configuration is the HS, at variance with what seems to be suggested by numerical simulations.

The origin of this apparent discrepancy can be discussed as follows. Firstly, it is important to recall that the variations of the calculated adsorption energy in the different configurations are comparable with the uncertainty due to physical approximations, as already pointed out, and therefore care has to be taken in considering the energy differences of the four configurations. Secondly, kinetic effects (e. g. diffusion, dissipation) may steer the adsorption process towards adsorption phases which are not at the thermodynamic equilibrium. Finally, we note that the HU and HU-s chemisorbed states have a larger distance from the Ni surface than HS (see table 3.2) and therefore are more exposed to the influence of the scanning STM tip which could induce uncontrolled site switching or desorption.

On the basis of the present picture of multisite chemisorption we can now discuss and refine our previous tentative assignment of the modes observed in HREEL spectra measured at 77 K [10]. As can be seen from table 3.3, we additionally point out that the measured 168 meV peak is also compatible within the expected accuracy with the asymmetric stretching mode of HU-s and HS configurations (besides HU), the 141 meV peak with the symmetric stretching mode of HS (besides HU and SB) and the 90 meV peak with the bending mode of HU-s and HS configurations (besides HU). In our previous report [10], the peak at 81 meV was correlated both to the linear, physisorbed configuration and to the SB configuration. The presence of this peak also at very low coverage (i. e. < 0.1 ML, as in the present work), where the physisorbed species is known to be absent, was interpreted as the fact that the SB species was already present in these conditions on the Ni surface. However, in our STM images the population of the SB site appears to be an extremely rare event, yielding a SB coverage well below the detection threshold of any non-local spectroscopic technique. On the other hand, the peak at 81 meV cannot be immediately attributed to any of the other chemisorbed configurations (neither HS nor HU-s, beside HU). Since the SB species shows the largest distance from the Ni surface, a tip induced site change may again explain the discrepancy. An alternative explanation is related to the possible influence of co-adsorbed hydrogen. It is well known that at our dosing temperatures (about 100 K) the Ni surface readily reconstructs upon dissociative adsorption of hydrogen [22, 23], impinging from the background due to the residual pressure of the UHV system. Since the energy differences between the possible stable CO_2 adsorption configurations are very small, $H-CO_2$ lateral interactions or surface relaxation may play a relevant role upon $H_2 + CO_2$ co-adsorption. In order to obtain information on the role of the presence of hydrogen on the population of the adsorption sites, we performed some preliminary STM measurements at 77 K, in the same measurement conditions of the HREEL spectra. Indeed, we could observe that, while the as-prepared surface showed only molecules in HS and HU sites, exposure to H_2 induced a site switching yielding only SB and HU species. Al-

though the role of the many different experimental variables (surface temperature, hydrogen exposure, exposure time, surface reconstruction) leading to the observed site change have not been thoroughly investigated yet, this observation points out to the fact that the presence of the peak at 81 meV in the HREEL spectra also at low coverage may be ascribed to the presence of very small amounts of hydrogen on the surface inducing a minor part of the HS and/or HU species to switch to the SB site. Since the discussion of the effects of hydrogen co-adsorption with CO_2 are beyond the scope of the present article, further measurements and details will be presented elsewhere. However, we cannot exclude that in the HREEL spectra at higher coverage the peak at 81 meV indeed is related to the presence of the SB species, but stabilized by lateral interactions irrespective of hydrogen co-adsorption effects.

3.3 Conclusions

We have imaged by means of LT-STM single CO_2 molecules chemisorbed in different adsorption configurations on a Ni(110) surface. *Ab-initio* DFT calculations, both within the standard GGA for the exchange-correlation functional and with the DFT-D correction for the Van der Waals contribution, predict four almost energetically equivalent chemisorption configurations. Three of the predicted adsorption geometries are consistent with the experimental STM images, namely the previously predicted HU and the novel HU-s and HS species. The DFT-D adsorption energy values, corrected also with the ZPE, are in good agreement with our previous TPD data. Accounting for the new adsorption configurations found in this work, we could refine the assignment of the vibrational modes observed in our previous HREEL spectra, discussing the possible influence of co-adsorbed atomic hydrogen in the population of the adsorption sites under UHV experimental conditions.

References

[1] H. Yang, Z. Xu, M. Fan, R. Gupta, R. B. Slimane, A. E. Bland, and I. Wright, *Progress in carbon dioxide separation and capture: A review*, J. Env. Sci. **20** (2008) 14.

[2] C. Song, *Global challenges and strategies for control, conversion and utilization of CO2 for sustainable development involving energy, catalysis, adsorption and chemical processing*, Catal. Today **115** (2006) 2.

[3] K. S. Lackner, *A Guide to CO2 Sequestration*, Science **300** (2003) 1677.

[4] G. A. Olah, A. Goeppert, and G. K. S. Prakash, *Beyond oil and gas: the methanol economy*, Wiley-VCH, 2006.

[5] U. Burghaus, *Surface science perspective of carbon dioxide chemistry–Adsorption kinetics and dynamics of CO2 on selected model surfaces*, Catal. Today **148** (2009) 212.

[6] J. B. Hansen, *Handbook of Heterogeneous Catalysis*, ed. by G. Ertl, H. Knözinger, F. Schüth, and J. Weitkamp, vol. 4, Wiley-VCH, 1997, 1856.

[7] J. Nerlov and I. Chorkendorff, *Methanol Synthesis from CO2, CO, and H2over Cu(100) and Ni/Cu(100)*, J. Catal. **181** (1999) 271.

[8] J. Nerlov and I. Chorkendorff, *Promotion through gas phase induced surface segregation: Methanol synthesis from CO, CO2 and H2 over Ni/Cu(100)*, Catal. Lett. **54** (1998) 171.

[9] J. Nerlov, S. Sckerl, J. Wambach, and I. Chorkendorff, *Methanol synthesis from CO2, CO and H2 over Cu(1 0 0) and Cu(1 0 0) modified by Ni and Co*, Appl. Catal. A **191** (2000) 97.

[10] X. Ding, L. De Rogatis, E. Vesselli, A. Baraldi, G. Comelli, R. Rosei, L. Savio, L. Vattuone, M. Rocca, P. Fornasiero, F. Ancilotto, A. Baldereschi, and M. Peressi, *Interaction of carbon dioxide with Ni(110): A combined experimental and theoretical study*, Phys. Rev. B **76** (2007) 195425.

[11] X. Ding, V. Pagan, M. Peressi, and F. Ancilotto, *Modeling adsorption of CO2 on Ni(110) surface*, Mater. Sci. Eng. C **27** (2007) 1355.

[12] E. Vesselli, L. De Rogatis, X. Ding, A. Baraldi, L. Savio, L. Vattuone, M. Rocca, P. Fornasiero, M. Peressi, A. Baldereschi, R. Rosei, and G. Comelli, *Carbon dioxide hydrogenation on Ni(110).* J. Am. Chem. Soc. **130** (2008) 11417.

[13] E. Vesselli, M. Rizzi, L. De Rogatis, X. Ding, A. Baraldi, G. Comelli, L. Savio, L. Vattuone, M. Rocca, P. Fornasiero, A. Baldereschi, and M. Peressi, *Hydrogen-Assisted Transformation of CO2 on Nickel: The Role of Formate and Carbon Monoxide*, J. Phys. Chem. Lett. **1** (2010) 402.

[14] K. L. Wong, G. Pawin, K.-Y. Kwon, X. Lin, T. Jiao, U. Solanki, R. H. J. Fawcett, L. Bartels, S. Stolbov, and T. S. Rahman, *A Molecule Carrier*, Science **315** (2007) 1391.

[15] C. Dri, A. Peronio, E. Vesselli, C. Africh, M. Rizzi, A. Baldereschi, M. Peressi, and G. Comelli, *Imaging and characterization of activated CO_{2} species on Ni(110)*, Phys. Rev. B **82** (2010) 165403.

[16] J. P. Perdew, K. Burke, and M. Ernzerhof, *Generalized Gradient Approximation Made Simple*, Phys. Rev. Lett. **77** (1996) 3865.

[17] P. Giannozzi et al., *QUANTUM ESPRESSO: A modular and open-source software project for quantum simulations of materials*, J. Phys.: Condens. Matter **21** (2009) 395502.

[18] S. Grimme, *Semiempirical GGA-type density functional constructed with a long-range dispersion correction*, Cond. Mat. Phys. **27** (2006) 1787.

[19] H. Jónsson, G. Mills, and K. W. Jacobsen, *Nudged elastic band method for finding minimum energy paths of transitions*, ed. by B. J. Berne, G. Ciccotti, and D. Coker, Singapore: World Scientific, 1998, chap. Classical and Quantum Dynamics in Condensed Phase Simulations, 385.

[20] J. Tersoff and D. R. Hamann, *Theory of the scanning tunneling microscope*, Phys. Rev. B **31** (1985) 805.

[21] E. Hasselbrink, *Non-adiabaticity in surface chemical reactions*, Surface Science **603** (2009) 1564.

[22] V. Penka, K. Christmann, and G. Ertl, *Ordered low-temperature phases in the H/Ni(110) system*, Surf. Sci. **136** (1984) 307.

[23] G. Kresse and J. Hafner, *First-principles study of the adsorption of atomic H on Ni (111), (100) and (110)*, Surf. Sci. **459** (2000) 287.

Chapter 4

The NH_3–NO coadsorption system on Pt(111)

The reduction of nitric oxide by ammonia to form N_2 and water has a prominent role in the control of NO_x emission from industrial and automotive processes. Ammonia (NH_3) is added to the exhaust gases in presence of a catalyst that promotes the selective NO reduction without favoring other undesired concurrent reactions such as O_2 reduction [1]. The most common catalysts for this Selective Catalytic Reduction (SCR) process are based on metal oxides or zeolites, whereas for low-temperature ($< 300\,^{\circ}C$) applications in absence of sulfur also noble metals are used [2].

The selectivity of this process has been tentatively explained by the formation of coadsorption complexes [3]. Indeed, studies with isotopically-labeled reagents ($^{15}NH_3$ and ^{14}NO) at high pressures (up to 2×10^4 Pa) showed that on various metals like Pt, Cu, and Ru the resulting N_2 stems mainly from the interaction of one molecule of NH_3 with one of NO [4], pointing towards a thorough intermixing of the two species at reaction conditions. Detailed studies of NH_3 and NO coadsorption by means of surface-integrating techniques were performed in particular on Pt(111) [3, 5, 6]. In this model system the two reactants barely dissociate [7, 8] and the reaction is almost inhibited in UHV [5], thus allowing for an unambiguous characterization of the forming complex. Such a complex formation was first proposed on the basis of Electron Energy Loss vibrational Spectroscopy (EELS) and Thermal Desorption Spectroscopy (TDS) experiments [5, 6]. Indeed, it was observed that some distinct vibrational losses of NO and NH_3 coalesce into a single feature upon coadsorption. Moreover, TDS proved that the two reactants stabilize each other on the surface, since they desorb together at 355 K, above the desorption maxima of the individually-adsorbed species. Eventually, Near-Edge X-ray Absorption Fine Structure spectroscopy (NEXAFS) measurements [3]. correlated the coadsorption of NH_3 with an increased N–O bond length, leading to a surface-mediated donor-acceptor picture: the weakening of the N–O bond is due to an enhanced electron back-donation into the NO π^* anti-bonding resonance, with NH_3 acting as electron donor.

All these techniques provided evidence for a relevant NH_3−NO interaction upon coadsorption on the (111) surface of platinum, but the exact nature of this coadsorption structure is at present unknown: what is its microscopic structure? Which is the nature of the complex-stabilizing interaction? Here we address the first question by providing an atomistic characterization of the adsorption of the NH_3−NO/Pt(111) complex, elucidating its structure by combining Scanning Tunnel Microscopy (STM) experiments and DFT calculations, and relating these new results to the observations in the literature. Evidence concerning the mechanisms involved in the NH_3−NO interaction is also provided.

This work, where I contributed part of the experiments and part of the DFT calculations, is the subject of two forthcoming publications [9, 10].

4.1 Methods

4.1.1 Experimental

Experiments were performed in two custom ultra-high vacuum setups (base pressure 1×10^{-8} Pa) hosting commercial Omicron microscopes: a variable-temperature STM (VT-STM) and a low-temperature STM (LT-STM). Images were acquired in constant-current mode with the sample cooled either by liquid nitrogen or by liquid helium. The tunneling parameters as well as the sample temperature are provided in each figure caption.

The Pt(111) sample was initially cleaned by repeated cycles of sputtering and annealing up to 1330 K. The appearance of graphene islands after the annealing drove us to modify the cleaning procedure along the lines of an existing recipe [11], to reduce the segregation of carbon: the daily preparation consisted of sputtering, annealing (5 min at 1270 K, with 5×10^{-6} Pa of oxygen during the heating ramp up to 970 K), oxidation ($p_{O_2} = 5 \times 10^{-6}$ Pa ramping the sample temperature from 970 K down to 110 K and then up to 570 K), reduction with H_2 to remove residual surface oxygen ($p_{H_2} = 1 \times 10^{-6}$ Pa ramping the sample temperature from 420 K down to to 300 K an up to 420 K), flash to 620 K to desorb residual hydrogen.

NH_3 (SIAD or Alphagaz, purity 99.995%) and NO (SIAD or Alphagaz, purity 99.9%) were dosed on the platinum sample using a microchannel-plate doser (VT-STM) or by backfilling the preparation chamber through a leak valve (LT-STM) up to a total pressure in the 10^{-7} Pa range. In the latter case the total exposure was determined by integrating the pressure signal sampled every 250 ms. Unless not otherwise specified gas dosing was performed at a surface temperature of about 90 K.

LT-STM images were elaborated [12][13] after their acquisition by simple plane subtraction, whereas a polynomial of degree 3 was subtracted from VT-STM ones. The only enhancement applied was B-spline resampling to increase the pixel count. When a known periodic lattice was observable – for instance a NO 2×2 structure –, it was used to calibrate the length scale of the image and to correct for the linear distortion due to the thermal drift of the sample with respect to the STM tip [14].

When indicated the images were also rotated to be oriented along the crystallographic axes of the platinum sample.

4.1.2 Theoretical

Density Functional Theory (DFT) calculations were performed with the plane-wave-based suite Quantum ESPRESSO [15], employing the Generalized Gradient Approximation for the exchange correlation functional in the Perdew-Burke-Ernzerhof parametrization (GGA-PBE) [16]. This approach does not take into account dispersive forces, which typically contribute a small correction to the energy of a covalent or ionic bond, but can be relevant for inter-molecular interactions such as in the NH_3–NO mixed layer. Before including explicitly these effects in our computations, we compared many of our GGA results with calculations performed within the Local Density Approximation of the exchange-correlation functional in the Perdew-Zunger parametrization (LDA-PZ) [17]. Since LDA typically overbinds – as opposed to GGA – we can consider the LDA and GGA values for the binding energies as a lower and an upper limit, respectively. We performed also some tests using the GGA with the revPBE functional [18] for the local and semi-local interaction, and the vdW-DF1 functional [19] for the non-local part.

Ultra-soft pseudo-potentials [20] were employed to describe the electron-ion interaction[1]. It was checked that spin-polarized calculations are not necessary, with the only exception of the open-shell gas-phase NO molecule. Standard numerical convergence for the most relevant physical quantities were obtained using a plane-wave cutoff of 30 Ry for the wave functions and 240 Ry for the charge density. The calculated lattice parameter of bulk platinum was found to be 400 pm, to be compared with the experimental value of 392 pm [21].

The platinum (111) surface was simulated by means of periodically-repeated supercells with slab geometry, with five metal layers and a vacuum space 1.85 nm wide, corresponding to eight inter-layer distances. Molecules are adsorbed at only one side of the slab, therefore a dipole correction [22] is used to compensate the fictitious electrostatic field due to the asymmetric configuration and the finite slab thickness. Atomic positions were relaxed until all forces were below 10^{-3} Ry/bohr, keeping the atoms of the two lowest layers of the platinum slab fixed at their bulk positions.

Integration over the Brillouin zone was performed using the "cold smearing" technique [23] with a smearing parameter of 2×10^{-2} Ry and Monkhorst-Pack mesh of k-points [24] dependent on the size of the surface cell: $6 \times 6 \times 1$ k-points for a 2×2 cell and $3 \times 3 \times 1$ for a 4×4 one.

[1] We employed the GGA-PBE and LDA-PZ pseudo-potentials H.pbe-van_bm.UPF, N.pbe-van_-bm.UPF, O.pbe-van_bm.UPF, Pt.pbe-n-van.UPF, H.pz-rrkjus.UPF, N.pz-rrkjus.UPF, O.pz-rrkjus.UPF, and Pt.pz-rrkjus.UPF available at `http://www.quantum-espresso.org`. We instead generated the GGA-revPBE pseudo-potentials by means of the atomic code of the Quantum ESPRESSO suite, employing an energy cutoff of 35 Ry and core cutoff radii for valence electrons of $r_s^{\mathrm{H}} = 1.2$ bohr, $r_s^{\mathrm{N}} = 1.6$ bohr, $r_p^{\mathrm{N}} = 1.5$ bohr, $r_s^{\mathrm{O}} = 1.6$ bohr, $r_p^{\mathrm{O}} = 1.6$ bohr, $r_s^{\mathrm{Pt}} = 2.6$ bohr, and $r_d^{\mathrm{Pt}} = 2.3$ bohr.

The experimental constant-current STM images were simulated within the Tersoff-Hamann approximation [25], according to which the tunneling current is proportional to the energy-Integrated Local Density of States. The ILDOS is the real-space density of electronic states which participate in the tunneling process, having an energy between ϵ_F and $\epsilon_F + |e|V$, were ϵ_F denotes the Fermi energy and V the experimental sample bias. Specifically, we mapped on a linear scale an ILDOS isosurface lying about 0.4 nm over the surface, blurring them with a Gaussian kernel (FWHM = 64 pm) to account for the finite size of the STM tip. This approach does not coincide with the usual mapping of the ILDOS at constant height: the latter is simpler to implement but it might lead to different results, especially when dealing with adsorbates.

Vibrational frequencies at the Γ point were computed using Density Functional Perturbation Theory (DFPT) [26] in order to add the Zero Point Energy correction (ZPE) to the adsorption energies and to compare vibrational modes with the available EELS experimental data. Since platinum is one order of magnitude more massive than the adsorbate atoms, we greatly reduced the computational burden of this calculation by keeping fixed the position of the metal atoms. The validity of this procedure was checked by performing test calculations which included also the first surface layer, without detecting any appreciable change in the relevant frequencies.

The adsorption energy is computed as

$$E_{\text{ads}} = E(\text{ads/Pt}) - \sum E(\text{ads}) - E(\text{Pt})$$

where the first term on the right side is the energy of the slab with the adsorbates, the second is the energy of the individual adsorbates in gas phase and the last is the energy of the bare platinum slab. With this convention, stable configurations are characterized by negative adsorption energies.

Charge transfers upon adsorption were estimated trough the Löwdin population analysis, calculated using atomic-orbital projectors [27]. Ball models were rendered with the XCrySDen software [28].

4.2 Results and discussion

The natural starting point to understand the formation of the NH_3–NO coadsorption complex is the separate adsorption of its "building blocks" – ammonia and nitric oxide –, which was already the subject of many experimental and theoretical studies. Here we first review what is already known on these surfaces, then we present our characterization by means of STM and DFT. We report only what is new or relevant to the present investigation, relating our findings to the previous literature. On this basis, we eventually present the data on the coadsorption layer.

4.2.1 Ammonia

Results from literature

Ammonia does not significantly dissociate on the (100) and (111) surfaces of platinum [7], as opposed to more open, stepped or polycrystalline ones [7, 29]. Its adsorption on Pt(111) was investigated with various surface science techniques [30–39] and different *ab initio* DFT-based approaches [40–47] identifying three adsorption states sequentially populated upon NH_3 uptake, labeled as α-, β-, and γ-NH_3 [33].

α-NH_3 is the first-appearing species, displaying a maximum coverage of 0.25 ML[2] and an "inverted umbrella" geometry: its three-fold axis stands up vertical [31]. with the N atom towards the platinum surface [32]. Concerning the adsorption site, a direct experimental determination is lacking: it was tentatively assigned to a threefold-hollow site from vibrational measurements [31], but all the existing DFT calculations [40–47] unambiguously favor the top site. Actually, the latter has a lower local electron density and thus a lower Pauli repulsion for electron-donor adsorbates like NH_3 [44, 48]. There is indeed a significant charge transfer from the molecule's lone-pair orbital to the surface, which enhances its dipole moment from the 1.47 D value of gas-phase NH_3 to about 2.0 D [32], leading to a strong electrostatic repulsion between adsorbed molecules [41]. The α-NH_3 adsorption energy per molecule is therefore coverage-dependent, as indicated by DFT calculations and TDS experiments: at a coverage of 1/4 ML calculations based on the Generalized Gradient Approximation predict an adsorption energy from −0.70 eV to −0.79 eV [43–47], which decreases to the range −0.92 eV to −0.97 eV at 1/9 ML [44, 47]. This variation is consistent with the broad desorption feature in the TDS spectra [33, 39].

The β-NH_3 state appears after the saturation of the α-NH_3 layer (0.25 ML), up to a total coverage of 1 ML; it is hydrogen-bonded to α-NH_3 and starts desorbing around 140 K [32]. TDS measurements [33] found an activation energy for desorption of (0.37 ± 0.03) eV, indicating a strong β-NH_3 − α-NH_3 hydrogen bond. This bond is indeed enhanced by the positive local charge on the H atom of α-NH_3, arising from the electron transfer from the molecule to the platinum surface [40].

Finally, γ-NH_3 is the multilayer of solid ammonia formed below 100 K at coverages higher than 1 ML [33].

Low-Energy Electron Diffraction (LEED) measurements did not detect any adsorbate-induced periodicity [31], either because NH_3 lacks a long-range order on this surface, or because the ordering is destroyed by the interaction with the LEED electron beam.

Our results

Our experimental STM images of the adsorbed NH_3 are shown in figure 4.1. The surfaces in panels 4.1b and 4.1c were prepared by saturating the clean platinum kept at $T < 140$ K with about 2 L of NH_3,[3] and then flashing the sample to the various tem-

[2] One monolayer (ML) corresponds to one adsorbate per surface atom

[3] One langmuir (L) is equal to 10^{-6} torr · s, or 1.33×10^{-4} Pa · s

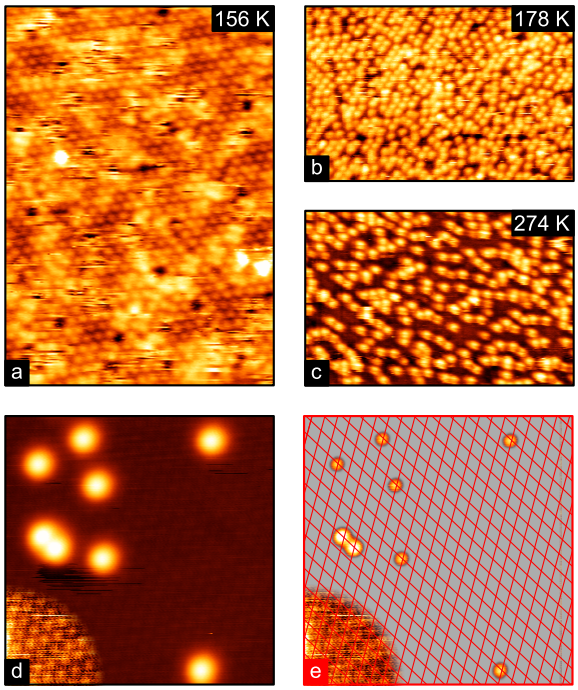

Figure 4.1: NH_3 adsorbed on Pt(111). (a) a complete layer of α-NH_3 after an uptake at 156 K. α-NH_3 shows a 2×2 local periodicity, and is covered by some β-NH_3; (b) a flash to 178 K leaves very small islands of 2×2 α-NH_3 and desorbs β-NH_3 completely; (c) a flash to 274 K reduces the coverage and arranges α-NH_3 molecules in short linear structures. (d) NH_3 dosed on a cold (98 K) surface. The substrate atoms are highlighted in the lower-left corner with a different color mapping. (e) is the same image as (d), with a different color mapping to emphasize the molecules' centers. The grid is described in the text and crosses over the top sites, which are therefore confirmed to be the NH_3 adsorption sites. Image parameters: (a) 12 nm $\times$ 17 nm, sample bias $V = 600$ mV, tunneling current $I = 0.1$ nA, surface temperature $T = 156$ K; (b) 20 nm $\times$ 13 nm, $V = 346$ mV, $I = 0.4$ nA, $T < 170$ K; (c) 20 nm $\times$ 13 nm, $V = 401$ mV, $I = 0.4$ nA, $T < 170$ K; (d) 5.6 nm $\times$ 5.6 nm, $V = -100$ mV, $I = 50$ nA, $T = 5$ K.

peratures reported in the figure. The surface in panel 4.1a was instead obtained by dosing NH_3 during the imaging of a surface kept at 156 K and previously prepared with a low coverage of NH_3. After an uptake at 156 K (figure 4.1a) 2×2 ordered domains are present on the surface, partially covered by an unresolved species. A flash to 178K (4.1b), above the desorption temperature of β-NH_3, completely removes the second-layer molecules leaving an incomplete first layer partly arranged in 2×2 islands. This suggests the identification of the 2×2 layer as α-NH_3 and the unresolved one as β-NH_3. Flashing at higher temperature (4.1c) reduces α-NH_3 coverage and destroys the 2×2 periodicity: the molecules appear in dimers and in short linear structures. Further flashing (not shown) leaves isolated molecules randomly distributed on the surface.

Figure 4.1d shows instead a surface obtained with a small exposure of NH_3 (0.04 L) on a cold surface (98 K) without any subsequent annealing. In this image the platinum atoms are individually resolved (emphasized in the lower-left corner), allowing us to directly determine the adsorption site of α-NH_3. To this end, the periodicity of the Pt(111) lattice was highlighted by Fourier filtering,[4] the filtered image was then used to overlay a grid on the original image (figure 4.1e), crossing above the platinum atoms. Eventually, the color-scale was expanded to evidence that all the NH_3 centers correspond to the grid crossings, and thus to the top sites.

On the theoretical side, we characterized by DFT the adsorption of α-NH_3 at different coverages, obtaining equilibrium geometry, energetics, charge redistribution, vibrational modes, and STM images. Our results agree with the existing literature [44] for the 1/4 ML case, confirming in particular that adsorption is favored on the top site. The adsorption energy with (without) ZPE correction is $E_{ads} = -0.60$ eV/molecule (-0.69 eV/molecule) for the 2×2 ordered layer at 1/4 ML, decreasing to -0.81 eV/molecule (-0.99 eV/molecule) at 1/16 ML. There is no general consensus in literature about the existence of other adsorption sites. We found stable but very weak adsorption on bridge, fcc-hollow, and hcp-hollow sites,[5] with a ZPE-corrected adsorption energy of -0.05 eV/molecule at 1/4 ML, equal within the numerical accuracy. Other DFT results concerning geometry, charge redistribution, and vibrational frequencies of the adsorbed α-NH_3 are reported in tables 4.2 and 4.3 for comparison with the coadsorbed complex.

Summarizing, our experiments demonstrate that α-NH_3 adsorbs on top sites as predicted by DFT, forming a short-ranged 2×2 structure only at coverages close to 1/4 ML. This periodicity readily disappears with decreasing coverage. It can be argued that the transition between the various α-NH_3 adsorption configurations with decreasing coverage – from 2×2 layer, to short linear structures, to randomly distributed molecules – is related to the strong electrostatic repulsion between the dipoles of the adsorbed molecules. Indeed, similar structures are obtained in a

[4] We employed a band-pass first-order Butterworth filter, upper wavelength 0.30 nm, lower wavelength 0.23 nm

[5] Hcp-hollow sites have an atom of the second layer under them, fcc-hollow ones have another hollow site instead.

Monte Carlo simulation of a lattice gas whose molecules interact with a dipole-dipole repulsive pair potential [49].

4.2.2 Nitric oxide

Results from literature

The adsorption of NO on Pt(111) has been extensively characterized both experimentally – as reviewed by Zhu and coworkers [8] – and theoretically [50–54], leading to a coherent picture with three different adsorption sites in a 2×2 periodicity. NO adsorption begins at threefold fcc-hollow sites (α-NO) up to a maximum coverage of 1/4 ML. Before the completion of this layer, also the top sites start to be populated (β-NO) up to a total coverage of 1/2 ML; eventually the hcp-hollow sites (γ-NO) are occupied too, up to 3/4 ML. Accordingly, the calculated GGA adsorption energies are [52]: -1.84 eV/molecule in adsorbing a complete layer of α-NO on clean platinum, -1.36 eV/molecule for a complete layer of β-NO on the α-NO layer, and -1.03 eV/molecule for a γ-NO layer on α-NO + β-NO. Adsorption always takes place trough the N atom, but while α-NO and γ-NO stand vertically on the surface, β-NO has its axis tilted by about 50° with respect to the surface normal [52, 55]. Upon heating, no dissociation takes place and the onset of desorption is 190 K, 275 K, and 320 K for γ-, β-, and α-NO, respectively [8]; the TDS peaks of the latter two species merge in a single broad feature [5, 6].

Our results

The left panels of figure 4.2 show the three adsorption configurations of nitric oxide, prepared in three different experiments by saturating the surface with about 3 L of NO and subsequently flashing to 310 K (α-NO), 210 K (α-NO + β-NO) or 180 K (α-NO + β-NO + γ-NO). On the basis of NO adsorption sites, we can distinguish between the fcc- and the hcp-hollow sites in the STM images. This allows us to determine the orientation of the platinum crystal and the relative orientation of its crystallographic axes with respect to the STM scanner reference frame.

By carefully flashing the NO-saturated surface to 315 K we were able to prepare an almost complete pure α-NO layer, with a residual β-NO coverage of about 0.04 ML. Any further increase of the flashing temperature induces the desorption of α-NO without reducing the residual β-NO coverage significantly. This effect can be ascribed to the mutual stabilization between α-NO and β-NO: measurements of the work function variation during NO uptake showed indeed that the two species have opposite dipole moments [56]. An existing DFT study attributes this effect to the different intra-molecular redistribution of the charge transfered upon adsorption from the surface to α-NO or β-NO [52].

Our DFT-optimized structures agree with the existing literature [52–55], giving for instance $E_{\text{ads}} = -1.64$ eV/molecule (-1.71 eV/molecule) with (without) ZPE correction for the 2×2 layer of α-NO. These structures are shown in the ball models

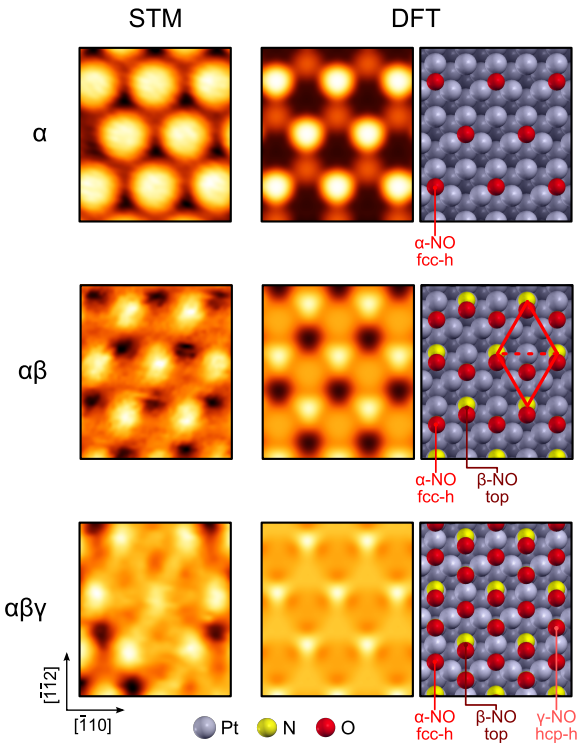

Figure 4.2: The adsorption structures of NO on Pt(111). Left column: experimental STM images; middle column: DFT-simulated STM images; right column: ball model of the calculated geometries. Top row: α-NO adsorbed on fcc-hollow sites at a total coverage $\Theta = 1/4$ ML; middle row: α-NO + β-NO adsorbed on top sites at $\Theta = 1/2$ ML, here a 2×2 unit cell delimited by four β-NO molecules is highlighted; bottom row: α-NO + β-NO + γ-NO adsorbed on hcp-hollow sites at $\Theta = 3/4$ ML, the dark spots on this experimental image are due to missing γ-NO molecules. The ball models show the β-NO molecules tilted in the same direction, whereas the corresponding simulated images are averages over the three possible tilt directions, as explained in the text. All images are 1.4 nm $\times$ 1.6 nm. Image parameters: (α) $V = -75$ mV, $I = 20$ nA, $T = 5$ K; ($\alpha\beta$) $V = 400$ mV, $I = 0.40$ nA, $T = 150$ K; ($\alpha\beta\gamma$) $V = 400$ mV, $I = 0.62$ nA, $T = 150$ K. An ILDOS iso-value of 4.0×10^{-2} nm^{-3} is used for all the simulated images.

of figure 4.2, together with the corresponding simulated STM images. Our DFT results confirm that β-NO is tilted towards an fcc-hollow site [52, 55], but also show that each β-NO molecule can be independently tilted in any of the three equivalent directions, indicating the absence of interaction between them. This finding is obtained by considering a 4×4 unit cell with 4 α-NO and 4 β-NO molecules: no appreciable energy difference is found if the β-NO molecules are tilted in different directions. Therefore a picture of the α-NO + β-NO layer where all the β-NO molecules are oriented in the same way – as necessarily implied by a 2×2 surface unit cell – is misleading [52, 55]. The energy barrier between the different tilt orientations is about 50 meV [54], thus experimental STM images at 150 K are likely a time average over the three different orientations. This would explain why they are compatible with a p3m1 symmetry that should be broken if β-NO is tilted in a preferential direction. To take into account this effect in the simulated STM images the ILDOS iso-surface was rotated around a β-NO site and averaged over the three possible tilt orientations. Similar considerations apply also to the α-NO + β-NO + γ-NO layer.

4.2.3 NH_3–NO mixed layer

We prepared the NH_3–NO complex by saturating with 2 L of NH_3 the α-NO layer described in the previous section. Figure 4.3a shows the corresponding surface imaged at $T < 170$ K. Above the fully extended 2×2 α-NO layer – not visible in the image – it is possible to distinguish three different adsorbed species on the basis of their apparent height: two of them, the majority species and the lower (darker) one, form a 2×2 layer, on which the third one is visible as a brighter trilobate feature. In order to gain insight on the nature and on the adsorption sites of these species we flashed the surface to obtain selective desorption. A first flash to 260 K leaves the surface unchanged, whereas a flash to 273 K desorbs the bright trilobate species. In a separate experiment this was tentatively identified as carbon monoxide adsorbed from the background, since we observed that its coverage increased after exposing the surface to CO. The darker species in figure 4.3a has a coverage comparable to the one of residual on-top β-NO on the α-NO layer used as a starting point for the preparation of the mixed layer, and desorbs after a flash to 300 K (figure 4.3b). This flashing temperature is the same of the TDS desorption peak of uncomplexed-NO from a mixed NH_3–NO layer, as reported by Burgess and coworkers [6]. Based on these indications, we tentatively identify the lower species as residual β-NO adsorbed on top sites, and the majority species in-registry with it as NH_3 adsorbed on-top as well. It should be noted here that our simulated STM images (not shown) do not reproduce the contrast difference between the β-NO and the NH_3 molecules of figure 4.3a. The reason of this discrepancy lies probably in the approximations used to derive the simulated STM images, that may fail in describing correctly such small height differences. More accurate simulations should take into account the polarization induced by the local electric field due to the STM tip.

A flash to 336 K (figure 4.3c) causes the partial desorption of the 2×2 layer,

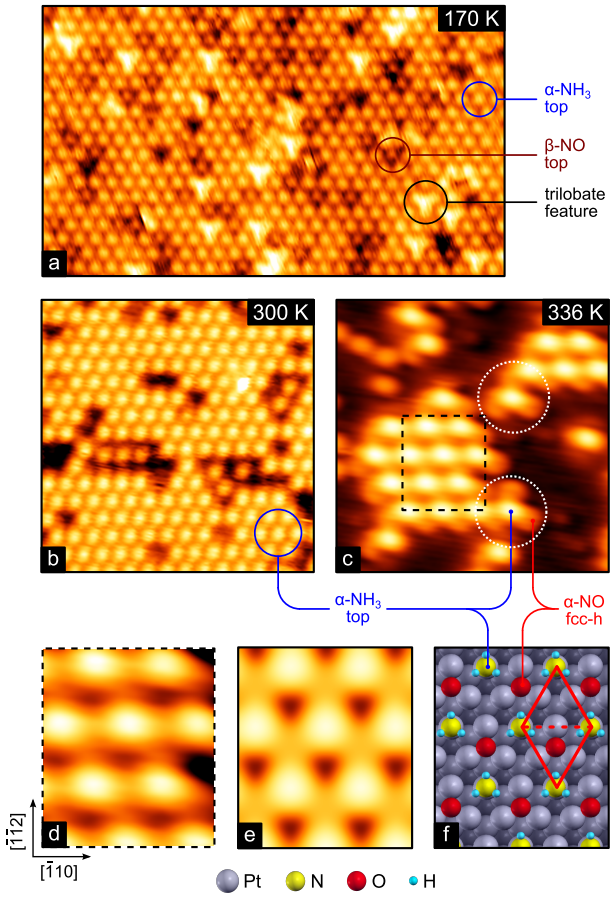

Figure 4.3: The NH_3–NO mixed layer on Pt(111). (a) the layer imaged at 170 K, with some β-NO molecules in-registry with NH_3 and the trilobate feature mentioned in the text; (b) two out-of-phase 2×2 domains of NH_3–NO after a flash to 300 K, β-NO is desorbed; (c) an island of NH_3–NO left by a flash to 336 K, the structure of the layer is manifest in the circles. Bottom: a detail from latter figure (d) with the corresponding DFT-simulated STM image (e) and a ball model (f) of the calculated geometry, on which a 2×2 unit cell delimited by four NH_3 molecules is highlighted. The dark spots on (d) are due to missing NH_3 molecules. Experimental parameters: (a) 15.5 nm $\times$ 9.1 nm, $V = 390$ mV, $I = 0.42$ nA, $T < 170$ K; (b) 8.2 nm $\times$ 8.2 nm, $V = 20$ mV, $I = 0.3$ nA, $T < 170$ K; (c) 4.7 nm $\times$ 4.7 nm, $V = -50$ mV, $I = 1.5$ nA, $T = 77$ K; (d) 1.4 nm $\times$ 1.6 nm, same parameters of (c). Theoretical image parameters: theoretical sample bias $V_{\mathrm{DFT}} = 200$ mV, ILDOS iso-value 4.0×10^{-2} nm^{-3}.

allowing to distinguish another species with lower apparent height. We attribute this lower feature to NO, since its apparent height with respect to the platinum surface is comparable to the one of α-NO alone on Pt(111) (from 8 pm to 35 pm, depending on tip condition and imaging parameters), whereas the brighter feature, already identified as NH_3, is comparable with α-NH_3 dosed alone (from 80 pm to 120 pm). From this image, the mixed layer can be argued to be the intercalation of a 2×2 adlayer of α-NH_3 with a similar 2×2 adlayer of NO, with the 1:1 NH_3:NO stoichiometry indicated by TDS measurements [6].

The adsorption site of NO in the mixed layer can be inferred by comparing the bottom row of figure 4.3 with the α-NO + β-NO layer (figure 4.2 middle row). In both cases there is a brighter species adsorbed on top sites, respectively α-NH_3 or β-NO. This species delimits a rhombic unit cell highlighted in the respective ball models. Since the images are oriented in the same way with respect to the crystallographic axes of the platinum surface, the upper half of the rhombic unit cells is centered on a hcp-hollow site and the lower one on a fcc-hollow one. In the α-NO + β-NO layer, the lower half of the cell appears brighter than the upper one, indicating to the presence of an α-NO molecule; the same contrast appears in the NH_3–NO mixed layer, indicating that also in this case NO is adsorbed in a fcc-hollow site.

From the discussion above we conclude that the mixed layer is the intercalation of a 2×2 adlayer of α-NH_3 with a 2×2 adlayer of α-NO, *id est* a mixture of the most stable structures of the two species adsorbed separately on Pt(111).

Our experimental determination of the adsorption geometry of the mixed layer relies totally on the identification of the adsorption site of NH_3 in this structure; further evidence is therefore needed to unambiguously confirm this picture. Indeed figure 4.4 shows that in principle there are six possible combinations of high-symmetry adsorption sites for the mixed layer. Among these, only three are compatible with the experimental STM images, where every triangle formed by three NO molecules surrounding an α-NH_3 points towards the $\langle \bar{1}\bar{1}2 \rangle$ directions, as emphasized at the borders of the adsorbate islands of figure 4.3c. In other words, only three combinations have the NO adsorbed in the lower half of a unit cell delimited by four NH_3 molecules, like the one in figure 4.3f. Another free parameter is the ammonia adsorption geometry: in principle, one can consider for NH_3 both "inverted umbrella" and "umbrella" configurations, with H atoms pointing upwards or towards the surface, respectively. The experimental STM images indicate however a similar apparent height for the complexed ammonia and for α-NH_3 alone on the surface, thus suggesting that the "inverted umbrella" geometry is retained.

In order to distinguish between these possibilities we performed DFT calculations to determine their equilibrium geometries and adsorption energies, reporting in table 4.1 only the configurations stable upon force relaxation. Among those compatible with the experimental STM images (upper part of the table), the stablest configuration is the no. 1, with NH_3 on top and NO on fcc-hollow sites, thus confirming our previous identification of the adsorption sites. The adsorption energy of other compatible configurations is at least 1.01 eV/cell higher, and the most of this difference comes from the fact that the no. 1 is the only configuration where NH_3

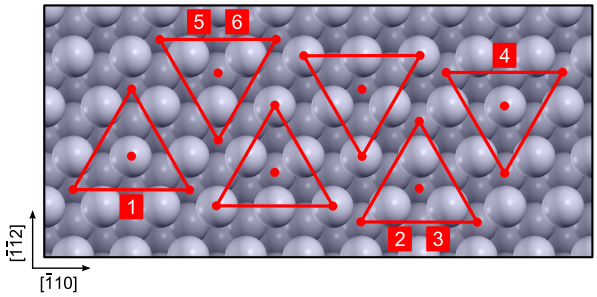

Figure 4.4: The six possible combinations of adsorption sites for the NH_3−NO 2×2 layer. In all cases the triangle center is the ammonia site, while the corners are the NO sites. Experimental STM images are compatible only with the upright triangles (lower row). The numbers refer to the configurations stable upon DFT force relaxation listed in table 4.1.

sits on-top: as we stated before, DFT calculations unambiguously support this site for NH_3 adsorption on this surface. Comparison with the experiment allows instead to exclude other possible stable configurations (lower part of table 4.1), such as the no. 4 where NH_3 sits on-top and NO on hcp-hollow sites, whose DFT adsorption energy is only 0.18 eV/cell higher than on-top NH_3 + fcc-hollow NO.

The stability of the mixed layer is evaluated by calculating the adsorption energy gain with respect to NH_3 and NO separately adsorbed in the same sites and at the same coverage. We therefore define the cohesion energy E_{coh} of the coadsorbed structure as

$$E_{coh} = \Big(E(NH_3 + NO/Pt_{2\times2}) + E(Pt_{2\times2})\Big) - \Big(E(NH_3/Pt_{2\times2}) + E(NO/Pt_{2\times2})\Big)$$

Here $E(NH_3 + NO/Pt_{2\times2})$ is the total energy of the platinum slab with the mixed layer adsorbed, $E(Pt_{2\times2})$ the energy of the clean slab and $E(NH_3/Pt_{2\times2})$ and $E(NO/Pt_{2\times2})$ the ones of a slab bearing an NH_3 layer and a NO one, respectively. This cohesion energy can be interpreted as the total-energy variation in desorbing a layer of one of the complex constituents – NO or NH_3 – from an otherwise clean platinum slab to adsorb it together with the other constituent. The variation of E_{coh} between the possible combinations of adsorption sites of table 4.1 closely follows the E_{ads} trend. In particular, we obtained for the on-top NH_3 + fcc-hollow NO layer $E_{coh} = -0.24$ eV (-0.29 eV) from a GGA calculation with (without) ZPE correction, and -0.50 eV from LDA without ZPE (table 4.2). This negative value indicates a stabilization upon complex formation, consistent with the shift towards higher temperature of the TDS desorption maxima of both NH_3 and NO upon coadsorption [5, 6]. The explicit inclusion of dispersion forces affects only marginally the geometric and electronic structure calculated by GGA, and gives cohesion energies in between the GGA and LDA values.

Table 4.1: Adsorption and cohesion energies (in eV/cell, without ZPE correction) for the stable NH_3−NO coadsorption geometries in a $\mathbf{2} \times \mathbf{2}$ unit cell. In the upper part are listed those compatible with the experimentally determined layer orientation. u-NH_3 indicates an "umbrella" geometry, with H atoms pointing towards the surface, while i-NH_3 indicates "inverted umbrella", with H atoms pointing upwards. u-NH_3 alone is not stable on the surface, so the corresponding cohesion energies remain undefined.

	configuration	E_{ads}	E_{coh}
1	i-NH_3 on-top + NO fcc-h	−2.69	−0.29
2	i-NH_3 fcc-h + NO hcp-h	−1.68	−0.06
3	u-NH_3 fcc-h + NO hcp-h	−1.58	–
4	i-NH_3 on-top + NO hcp-h	−2.51	−0.24
5	i-NH_3 hcp-h + NO fcc-h	−1.82	−0.07
6	u-NH_3 hcp-h + NO fcc-h	−1.72	–

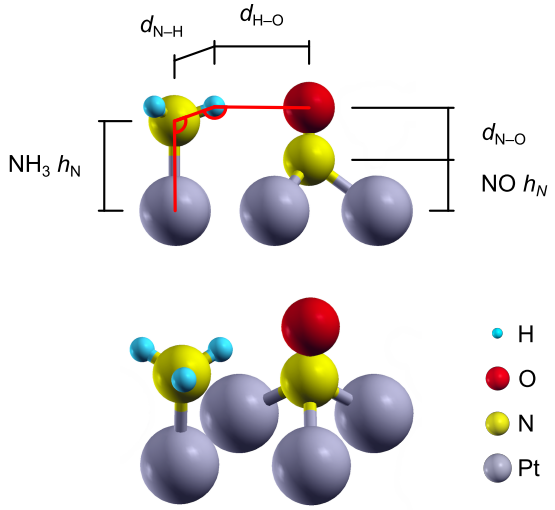

Figure 4.5: The geometrical parameters listed in table 4.2.

Having confirmed that the NH_3−NO mixed layer is the intercalation of an on-top α-NH_3 layer with a fcc-hollow α-NO one, we summarize the DFT results for this structure in table 4.2, reporting a comparison of cohesion energies calculated in different approximations, structural parameters, and charge transfers for the individually adsorbed NO and NH_3, and the α-NO − α-NH_3 2×2 mixed layer.

The calculated properties of this mixed layer are in line with the experimental findings. Specifically, NEXAFS measurements [3] detected an increase of the

Table 4.2: Calculated geometries, cohesion energies, and charge transfers for α-NO, α-NH_3, and the coadsorbed NH_3–NO. Columns refer to α-NO and α-NH_3 individually adsorbed on 2×2 unit cells (constituents), to the same molecules coadsorbed in the same cell (mixed layer), and to a triangular unit of α-NH_3 + 3 α-NO in a 4×4 cell (unit). Symbols denote: h height of an atom with respect to the average height of surface atoms; d distance between two atoms; α angle between three atoms; Δn difference of total projected charges with respect to the gas-phase molecules frozen in the adsorbed geometry; E_{coh} cohesion energy. The values for d_{H-O} and α_{O-H-N} before allowing the 2×2 layer to relax from the separate-adsorption geometry are reported in brackets.

	parameter		constituents	NH_3–NO	
				unit	mixed layer
	E_{coh} GGA+ZPE	eV/cell		unstable	−0.24
	E_{coh} GGA	eV/cell		−0.11	−0.29
	E_{coh} LDA	eV/cell		−0.39	−0.50
	d_{H-O}	pm	(230)	223	229
	α_{O-H-N}	deg	(164.7)	158.5	159.7
NO	h_N	pm	134	130	123
	d_{N-O}	pm	120	122	126
	Δn_σ [(a)]	electrons	−0.54	−0.55	−0.57
	Δn_π [(b)]	electrons	+0.68	+0.43	+0.80
NH_3	h_N	pm	220	221	217
	d_{N-H}	pm	103	103	102
	α_{Pt-N-H}	deg	107.5	110.2	109.7
	Δn [(c)]	electrons	−0.34	−0.34	−0.33

[(a)] NO n_σ is the sum of projected charges on $2s$ and $2p_z$ atomic orbitals of N and O, z being the surface normal;
[(b)] NO n_π is the sum of projected charges on $2p_x$ and $2p_y$ atomic orbitals of N and O;
[(c)] NH_3 n is the sum of projected charges on NH_3 atomic orbitals.

Table 4.3: Comparison between experimental (EELS) and theoretical (DFPT) vibrational spectra of α-NH_3, α-NO + β-NO, and NH_3−NO mixed layers.

configuration	coverage [ML]	vibrational mode	$\hbar\omega_{\text{theo}}$ [meV]	$\hbar\omega_{\text{exp}}$ [meV]	relative difference [(a)]
α-NH_3	1/4	NH_3 sym. def.	128	135	−0.05
α-NO + β-NO	1/4 + 1/4	N−O stretch	182	185	−0.01
		N−O stretch	217	212	0.02
α-NH_3 + α-NO	1/4 + 1/4	NH_3 sym. def. + N−O str.	150	159	−0.06
		NH_3 sym. def. + N−O str.	160		0.01

[(a)] $(\hbar\omega_{\text{theo}} - \hbar\omega_{\text{exp}})/\hbar\omega_{\text{exp}}$

energy separation between the adsorbed NO σ^* and π^* anti-bonding resonances in the mixed layer with respect to a pure-NO one, indicating a N−O bond length increase from (124 ± 5) pm to (128 ± 5) pm. This was attributed to an increased electron back-donation from Pt surface to the π^* anti-bonding resonance of the adsorbed NO molecule. This donation/back-donation picture is confirmed by our DFT calculations, which predict a net electron transfer from NH_3 to Pt surface, an elongated N−O bond, and an increased NO π projected charge inside the mixed layer (table 4.2). The calculations also predict a higher work function of the mixed layer ($\phi = 3.9$ eV) with respect to pure NH_3 ($\phi = 2.8$ eV), consistently with the reported experimental trend [3]. Eventually, the calculation of the vibrational modes of the adlayers correctly predicts the coalescence of the NH_3 and NO modes upon complex formation as detected by EELS [5] (table 4.3).

It should be noted that our preparation of the mixed layer differs from what reported in literature. Indeed, we first dose NO, anneal the surface to get an α-NO layer, and then dose NH_3, while in all the previous studies [3, 5, 6] NH_3 was dosed before NO. The recipe in literature comes from the observation by Esch and coworkers [3] that NH_3 adsorption is almost completely inhibited on a NO-saturated surface, while NO can still adsorb on a surface covered by NH_3. On the basis of our findings, this behavior can be easily rationalized by considering that both α-NH_3 and β-NO compete for the same on-top adsorption sites: when the surface is already saturated by NO these sites are not available for ammonia. On the contrary, when NH_3 is dosed first, fcc-hollow sites are available for α-NO adsorption. This procedure, however, cannot produce a long-range ordered mixed layer, because α-NH_3 is ordered only locally. An almost pure α-NO layer is instead the best, highly ordered template for the formation of a complete mixed layer upon NH_3 adsorption. In order to check that the atomic-level structure of the mixed layer is preserved regardless of the preparation procedure, we concluded our experiments by analyzing the surface obtained by dosing NH_3 first. As expected, while the order in the saturated layer is remarkably lower, the images obtained after flashing the sample in order to reduce the coverage removing excess adsorbates are indistinguishable from

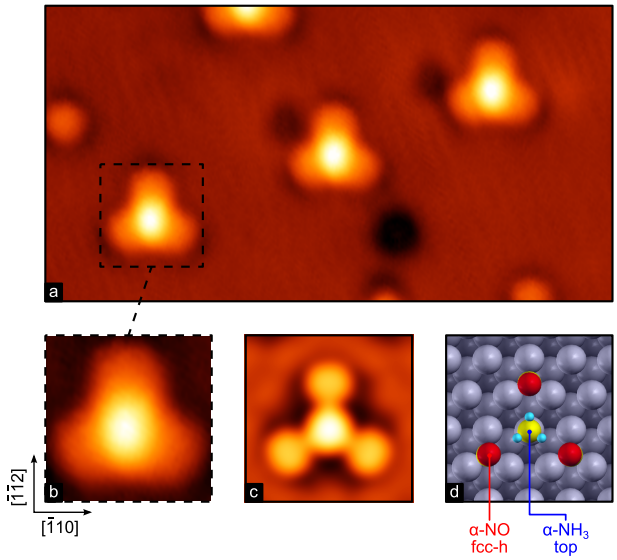

Figure 4.6: NH_3-3NO triangular units on Pt(111). (a) experimental STM image (6.6 nm × 3.4 nm). Bottom: a 1.1 nm × 1.1 nm detail (b) of the former image with the corresponding DFT-calculated STM image (c) and a ball model of the calculated geometry (d). Experimental image parameters: $V = 15$ mV, $I = 10$ nA, $T = 5$ K. For the DFT-calculated STM image an ILDOS iso-value of 1.3×10^{-2} nm^{-3} was used.

those obtained by our recipe.

4.2.4 NH_3-3NO isolated units

Annealing the mixed layer surface up to 345 K leads to the desorption of most of the adsorbates, leaving on the surface a small coverage of triangular units (figure 4.6) with a maximum apparent height of 87 pm ÷ 95 pm, compatible with the one of NH_3 in the mixed layer. Like the triangles at the borders of NH_3-NO islands in figure 4.3c, they are composed by a higher central molecule surrounded by three lower ones, and have the same orientation as well, pointing towards the $[1\bar{1}2]$ direction. We conclude that these units are formed by a central α-NH_3 molecule adsorbed on a top site and three α-NO molecules on fcc-hollow ones. Other choices of adsorption sites compatible with the experimental orientation of these triangles would adsorb NH_3 on a site different from the the top one, and the DFT calculations on the 2×2 layer (table 4.1) already indicate that shifting NH_3 from the top site is energetically unfavored.

This unit was simulated in a 4×4 unit cell, and we define its cohesion energy

as

$$\text{unit } E_{\text{coh}} = \Big(E(\text{NH}_3 + 3\text{NO/Pt}_{4\times4}) + E(\text{Pt}_{4\times4})\Big) - \Big(E(\text{NH}_3/\text{Pt}_{4\times4}) + E(3\text{NO/Pt}_{4\times4})\Big)$$

in order to account for the interaction between ammonia and nitric oxide, while leaving aside the one between the three NO molecules. We chose this definition because there are three NH_3−NO bonds per unit cell both in this triangular unit and in the 2×2 layer, so by comparing the cohesion energies for the two cases we obtain the relative strength of the NH_3−NO bond in the two structures. This cohesion energy and the structural parameters for NO in this structure (table 4.2) are in-between the α-NO and NH_3−NO layers. Since the 1:3 NH_3:NO stoichiometry of this structure is also intermediate, one could argue that these quantities are related to the amount of electron donation from ammonia to platinum and subsequent back-donation to the NO π^* resonance. This simple picture is however questioned by the reduced NO π population in this structure (table 4.2), which is even lower than in the α-NO case.

4.2.5 The NH_3−NO bond

The fact that NH_3 and NO are stabilized in a 2×2 coadsorption layer, where the two molecules are in a favorable geometry to react with each other, points towards a key role of the NH_3−NO inter-molecular interaction in the selectivity of NO reduction. This interaction is mediated by the charge transfer through the platinum surface, as detected both by NEXAFS and DFT, however the presence of a hydrogen atom in a linear configuration in-between two electronegative species – the nitrogen of ammonia and the oxygen of NO – suggests that a direct hydrogen bond may have a role (figure 4.5) Moreover, in the "triangular unit", the NO molecules slightly bend (3.4°) towards NH_3, hinting at the presence of H−O bonds. Their relative strength is suggested by the fact that the vast majority of the units left on the surface after the annealing still have three NO "leafs", meaning that they are stable up to NH_3 desorption. To assess whether a direct hydrogen bond contribute to the overall picture, we used the characterizing criteria recently given by the International Union of Pure and Applied Chemistry (IUPAC) [57, 58]. The hydrogen bond is defined by IUPAC as *«an attractive interaction between a hydrogen atom from a molecule or a molecular fragment X−H in which X is more electronegative than H, and an atom or a group of atoms in the same or a different molecule, in which there is evidence of bond formation.»* The situation is depicted as X−H · · · Y−Z, where in our case X is the nitrogen of ammonia, Y and Z are respectively the O and N atoms of NO (N−H · · · O−N). In the following the IUPAC criteria are listed and used to discuss our DFT results.

«The forces involved in the formation of a hydrogen bond include those of electrostatic origin, those arising from charge transfer between the donor and acceptor leading to partial covalent bond formation between H and Y [O]*, and those originating from dispersion.» «The atoms X and H are covalently bonded to one another and*

the X–H bond is polarized, the H · · · Y [H · · · O] *bond strength increasing with the increase in electronegativity of X* [N].» The analysis of Löwdin charges indicate an electrostatic interaction, together with the polarization of the N–H bond: the partial positive charge of hydrogen (+0.54 |*e*|) is in-between the negative charges of ammonia's N (−0.54 |*e*|) and NO's oxygen (−0.26 |*e*|). The partially covalent character of the H · · · O interaction is made evident by the decomposition of the DFT-calculated electronic structure into localized orbitals (Maximally-Localized Wannier Functions [59]), which is reported in a forthcoming publication [10]. The most relevant result is that there is one Wannier function associated to each H · · · O bond, and their charge barycenters are in-between O and H, indicating a directional, covalent interaction. This covalency is only partial, since the charge centers are not in the middle between H and O, but closer to the latter. Eventually, our calculations could not provide insight on the role of dispersive interactions, since these are neglected in standard DFT-GGA. Tests performed with more refined schemes (wdW-DF [19, 60, 61] and DFT-D [62]), reported in [10], gave unsatisfactory results, due also to implementation problems.

«The X–Y · · · Z [N–H · · · O] *angle is usually linear (*180°*) and the closer the angle is to* 180°*, the stronger is the hydrogen bond and the shorter is the H · · · Y* [H · · · O] *distance.»* The N–H · · · O angle in the equilibrium structure is about 160° (table 4.2).

«The length of the X–H [N–H] *bond usually increases on hydrogen bond formation leading to a red shift in the infrared X–H stretching frequency and an increase in the infrared absorption cross-section for the X–H stretching vibration. The greater the lengthening of the X–H bond in X–Y · · · Z* [N–H · · · O]*, the stronger is the H · · · Y* [H · · · O] *bond. Simultaneously, new vibrational modes associated with the formation of the H · · · Y bond are generated.»* The N–H bond length in NH_3 in presence of NO does not change with respect to ammonia separately adsorbed. There are three modes associated to N–H vibrations: one symmetric stretching mode with energy of 412 meV in NH_3/Pt, that decreases to 406 meV in the 2×2 mixed layer and 405 meV in the isolated triangular structure; two degenerate antisymmetric stretchings, with energy of 430 meV in NH_3/Pt, becoming 420 meV in the mixed layer and 419 meV in the isolated triangular structure. A small, but well defined, red shift is therefore detected. Eventually, several oscillation modes couple the two molecules.

By means of STM-IETS, which will be the subject of chapter 5, we tried to detect experimentally the shift induced by hydrogen bonding by measuring the vibrational modes of NO molecules individually adsorbed on the surface and complexed in the triangular NH_3–3NO units shown in figure 4.6. The signal-to-noise ration we were able to achieve at that time limited our measurements to the low-energy part of the spectrum ($\hbar\omega < 100$ meV), well below the vibrational signatures of hydrogen bonding. However we successfully detected two vibrations, at (48.4 ± 0.2) meV in the case of isolated NO, and at (53.0 ± 0.4) meV in the units (figure 4.7).[6] DFT calculations attributed the former to the hindered rotation of NO (two almost-degenerate

[6] The statistical uncertainties come from 7 measurements on the isolated NO and 8 on the triangular NH_3–3NO unit, like the ones displayed in figure 4.7.

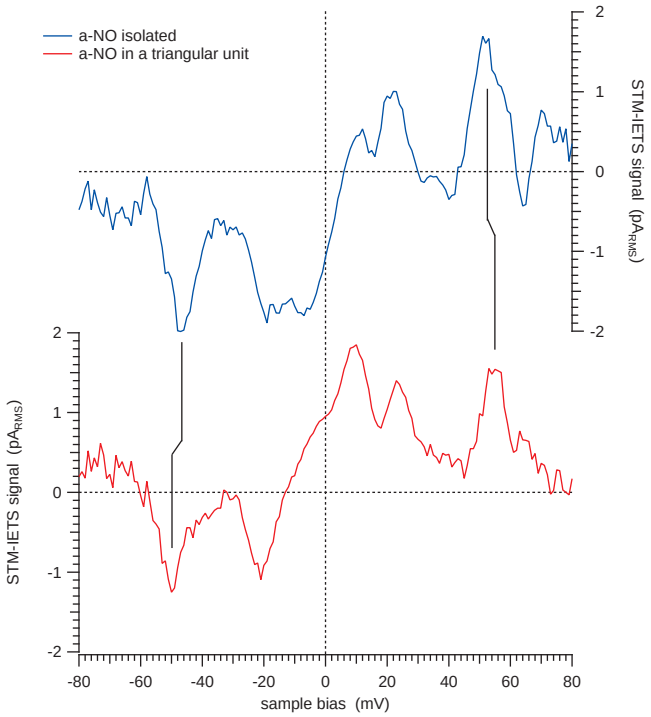

Figure 4.7: STM-IETS spectra of an individual α-NO molecule, and of a NO molecule in a triangular complex. Tip stabilized at $V = -80\,\mathrm{mV}$, $I = 20\,\mathrm{nA}$, sinusoidal modulation of $V_\mathrm{m} = 4.0\,\mathrm{mV_{pk}}$ at $f_\mathrm{m} = 1312\,\mathrm{Hz}$. The marked features correspond to the vibrational modes described in the text. The displayed traces are the difference between measurement acquired on the molecule and on the platinum surface. 670 individual spectra were averaged, for a total measurement time of 5 h 30 min. IETS signal was sampled in 1 mV steps, stabilizing the lock-in low-pass filter (fourth-order RC with 30 ms time constant, having a roll-off of 24 dB/oct, $f_{-3\,\mathrm{dB}} = 2.31\,\mathrm{Hz}$, $\mathrm{ENBW_{LPF}} = 2.60\,\mathrm{Hz}$) for 150 ms after each voltage step, before acquiring data for 10 ms.

modes at 52 meV and 53 meV, for 1/9 ML NO coverage), and the latter to a collective hindered translation of the unit at 55 meV.

«The X–H · · · Y–Z [N–H · · · O–N] *hydrogen bond leads to characteristic NMR signatures that typically include pronounced proton deshielding for H in X–H* [N–H]*, through hydrogen bond spin-spin couplings between X* [N] *and Y* [O]*, and nuclear Overhauser enhancements.»* We did not afford the NMR characterization, since the possibility of calculating NMR shifts via density-functional perturbation theory has been recently implemented in the QUANTUM ESPRESSO suite, but limiting to insulating systems.

«The Gibbs energy of formation for the hydrogen bond should be greater than the thermal energy of the system for the hydrogen bond to be detected experimentally.» HREELS experiments detect the effect of NH_3–NO interaction at 300 K [5].

Summarizing, we can conclude that there is a partial hydrogen-bond component in the NH_3–NO interaction. Several hints, such as the weak red-shift of the N–H modes and the limited covalent character of the H · · · O bond, point towards a limited relative importance of this bonding mechanism with respect to the substrate-mediated interaction.

4.3 Conclusions

We investigated the coadsorption of ammonia and nitric oxide on the (111) surface of platinum by combining atomically-resolved STM imaging and state-of-the-art DFT calculations.

Our investigation started from the individual adsorption of these species, imaging the coverage-dependent adsorption structures of NH_3 – short-ranged 2×2 adlayer, linear structures, isolated molecules – and confirming experimentally that the top site is the preferred one for its adsorption on this surface. Regarding NO, we were able to obtain an ordered and almost complete α-NO 2×2 layer with a minimal residual coverage of β-NO, which is the ideal template for the selective preparation of the coadsorption complex with long-range order.

By coadsorbing ammonia on this substrate, a mixed NH_3–NO adlayer with the same periodicity results. We determined the adsorption geometry of this layer, in particular NH_3 adsorbs on top and NO on fcc-hollow sites. The adsorption characterization provided by DFT agrees with the existing experimental results, corroborating the proposed model of interaction via surface-mediated charge transfer from NH_3 lone-pair orbital to NO π^* one [3]. The DFT cohesional stabilization of the extended layer is 0.29 eV per formula unit, and the calculated vibrational energies of both the coadsorption structure and of its constituents fit the experimental values found in literature. Eventually, the peculiar geometry of this layer points towards the existence of hydrogen bonds: the hydrogen atoms lie indeed between the nitrogen of ammonia and the oxygen of NO. Referring to IUPAC definition, we ascertained that an hydrogen-bond component is indeed present, but it is of relative importance with respect to the substrate-mediated interaction.

Our results demonstrate that the NH_3–NO interaction stabilizes a coadsorption layer where the two species are intermixed in a favorable geometry to react with each other. Further studies are required to properly assess the relevance of the mixed layer we characterized in the real catalytic process, taking into account the pressure [63] and materials gap as well as the possible influence of other coadsorbed species such as oxygen, always present in combustion exhausts.

References

[1] H. Bosch and F. Janssen, *n*, Catal. Today **2** (1988).

[2] P. Forzatti, *Present status and perspectives in de-NOx SCR catalysis*, Appl. Catal. A **222**.1-2 (Dec. 2001) 221; M. Shelef, *Selective Catalytic Reduction of NOx with N-Free Reductants*, Chem. Rev. **95**.1 (Jan. 1995) 209; V. Pârvulescu, P. Grange, and B. Delmon, *Catalytic removal of NO*, Catal. Today **46**.4 (Dec. 1998) 233; R. M. Heck, J. M. Chen, and B. K. Speronello, *Operating characteristics and commercial operating experience with high temperature SCR NOx catalyst*, Environ. Prog. **13**.4 (Nov. 1994) 221.

[3] F. Esch, T. Greber, S. Kennou, A. Siokou, S. Ladas, and R. Imbihl, *The formation of a NO-NH3 coadsorption complex on a Pt(l11) surface: a NEXAFS study*, Catal. Lett. **38** (1996) 165.

[4] K. Otto, M. Shelef, and J. T. Kummer, *Studies of surface reactions of nitric oxide by nitrogen-15 isotope labeling. I. Reaction between nitric oxide and ammonia over supported platinum at 200-250.deg.* J. Phys. Chem. **74**.13 (June 1970) 2690; K. Otto, M. Shelef, and J. T. Kummer, *Studies of surface reactions of nitric oxide by isotope labeling. II. Deuterium kinetic isotope effect in the ammonia-nitric oxide reaction on a supported platinum catalyst*, J. Phys. Chem. **75**.7 (Apr. 1971) 875; K. Otto and M. Shelef, *Studies of surface reactions of nitric oxide by isotope labeling. IV. Reaction between nitric oxide and ammonia over copper surfaces at 150-200.deg.* J. Phys. Chem. **76**.1 (Jan. 1972) 37; K. Otto and M. Shelef, *Studies of Surface Reactions of NO by Isotope Labeling*, Z. Phys. Chem. **85**.5_6 (July 1973) 308; S. Lombardo, F. Esch, and R. Imbihl, *The NO + NH3 reaction on Pt(100): steady state and oscillatory kinetics*, Surf. Sci. **271**.3 (Jan. 1992) L367.

[5] J. Gland and B. Sexton, *Observation of an NH3-NO complex on the Pt(111) surface*, J. Catal. **68** (1981) 286.

[6] D. Burgess, R. Cavanagh, and D. King, *NO/NH3 coadsorption on Pt(111): Kinetic and dynamical effects in rotational accommodation*, Surf. Sci. **214** (1989) 358.

[7] D. Löffler and L. Schmidt, *Kinetics of NH3 decomposition on single crystal planes of Pt*, Surf. Sci. **59** (1976) 195.

[8] J. Zhu, M. Kinne, T. Fuhrmann, R. Denecke, and H.-P. Steinrück, *In situ high-resolution XPS studies on adsorption of NO on Pt()*, Surf. Sci. **529** (2003) 384.

[9] A. Peronio, A. Cepellotti, S. Marchini, N. Abdurakhmanova, C. Dri, C. Africh, F. Esch, M. Peressi, and G. Comelli, *The NH3–NO coadsorption system on Pt(111): I structure of the NH3–NO layer*, J. Phys. Chem. C (2013) submitted.

[10] A. Cepellotti, A. Peronio, S. Marchini, N. Abdurakhmanova, C. Dri, C. Africh, F. Esch, M. Peressi, and G. Comelli, *The NH3–NO coadsorption system on Pt(111): II nature of the stabilizing intermolecular interaction*, J. Phys. Chem. C (2013) submitted.

[11] L. Bianchettin, A. Baraldi, S. de Gironcoli, E. Vesselli, S. Lizzit, L. Petaccia, G. Comelli, and R. Rosei, *Core level shifts of undercoordinated Pt atoms.* J. Chem. Phys. **128** (2008) 114706.

[12] D. Nečas and P. Klapetek, *Gwyddion: an open-source software for SPM data analysis*, Cent. Eur. J. Phys. **10** (2011) 181.

[13] Scanning Probe Image Processor `http://www.imagemet.com/`.

[14] J. F. Jørgensen, *Calibration, drift elimination, and molecular structure analysis*, en, J. Vac. Sci. Technol. B **12** (1994) 1698.

[15] P. Giannozzi et al., *QUANTUM ESPRESSO: a modular and open-source software project for quantum simulations of materials.* J. Phys.: Cond. Matt. **21** (2009) 395502.

[16] J. P. Perdew, K. Burke, and M. Ernzerhof, *Generalized Gradient Approximation Made Simple*, Phys. Rev. Lett. **77** (1996) 3865.

[17] J. P. Perdew, *Self-interaction correction to density-functional approximations for many-electron systems*, Phys. Rev. B **23** (1981) 5048.

[18] Y. Zhang and W. Yang, *Comment on "Generalized Gradient Approximation Made Simple"*, Phys. Rev. Lett. **80** (1998) 890.

[19] M. Dion, H. Rydberg, E. Schröder, D. C. Langreth, and B. I. Lundqvist, *Van der Waals Density Functional for General Geometries*, Phys. Rev. Lett. **92** (2004) 246401.

[20] D. Vanderbilt, *Soft self-consistent pseudopotentials in a generalized eigenvalue formalism*, Phys. Rev. B **41** (1990) 7892.

[21] J. W. Arblaster, *Crystallographic Properties of Platinum*, Platinum Met. Rev. **41**.1 (1997) 12; J. W. Arblaster, *Crystallographic Properties of Platinum*, Platinum Met. Rev. **50**.3 (July 2006) 118.

[22] L. Bengtsson, *Dipole correction for surface supercell calculations*, Phys. Rev. B **59** (1999) 12301.

[23] N. Marzari, D. Vanderbilt, A. De Vita, and M. Payne, *Thermal Contraction and Disordering of the Al(110) Surface*, Phys. Rev. Lett. **82** (1999) 3296.

[24] H. J. Monkhorst and J. D. Pack, *Special points for Brillouin-zone integrations*, Phys. Rev. B **13** (1976) 5188.

[25] J. Tersoff and D. R. Hamann, *Theory of the scanning tunneling microscope*, Phys. Rev. B **31** (1985) 805.

[26] S. Baroni, S. de Gironcoli, and A. Dal Corso, *Phonons and related crystal properties from density-functional perturbation theory*, Rev. Mod. Phys. **73** (2001) 515.

[27] A. Szabo and N. S. Ostlund, *Modern quantum chemistry*, English, Dover Publications, New York 1996.

[28] A. Kokalj, *Computer graphics and graphical user interfaces as tools in simulations of matter at the atomic scale*, Comput. Mater. Sci. **28** (2003) 155.

[29] J. Gland, *Adsorption and decomposition of nitric oxide and ammonia on a stepped platinum single crystal surface*, Surf. Sci. **71** (1978) 327.

[30] B. A. Sexton and G. E. Mitchell, *Vibrational spectra of ammonia chemisorbed on platinum (111)*, Surf. Sci. **99** (1980) 539.

[31] B. A. Sexton and G. E. Mitchell, *Vibrational spectra of ammonia chemisorbed on platinum (111)*, Surf. Sci. **99** (1980) 523.

[32] G. B. Fisher, *The electronic structure of two forms of molecular ammonia adsorbed on Pt(111)*, Chem. Phys. Lett. **79** (1981) 452.

[33] J. L. Gland and E. B. Kollin, *Ammonia adsorption on the Pt(111) AND Pt(S)-6(111) × (111) surfaces*, Surf. Sci. **104** (1981) 478.

[34] W. Guthrie, J. Sokol, and G. Somorjai, *The decomposition of ammonia on the flat (111) and stepped (557) platinum crystal surfaces*, Surf. Sci. **109** (1981) 390.

[35] J. M. Gohndrone, *Ammonia adsorption and decomposition on several faces of platinum*, J. Vac. Sci. Technol., A **7** (1989) 1986.

[36] W. Mieher and W. Ho, *Thermally activated oxidation of NHs on Pt(111): intermediate species and reaction mechanisms*, Surf. Sci. **322** (1995) 151.

[37] G. Szulczewski and R. J. Levis, *Collision-induced desorption of ammonia chemisorbed on Pt{111}: From direct measurement of the threshold energy to determination of the surface–adsorbate bond strength*, J. Chem. Phys. **103** (1995) 10238.

[38] I. Villegas and M. J. Weaver, *Infrared spectroscopy of model electrochemical interfaces in ultrahigh vacuum: interfacial cation solvation by ammonia on Pt(111)*, Surf. Sci. **367** (1996) 162.

[39] J. T. Ranney, A. J. Franz, and J. L. Gland, *Surface interactions between coadsorbed ammonia and carbon monoxide on the Pt(111) surface*, Surf. Sci. **384** (1997) L865.

[40] D. Jennison, P. Schultz, and M. Sears, *Ab initio calculations of adsorbate hydrogen-bond strength: ammonia on Pt(111)*, Surf. Sci. **368** (1996) 253.

[41] D. Jennison, P. Schultz, and M. Sears, *Ab Initio Ammonia and CO Lateral Interactions on Pt(111).* Phys. Rev. Lett. **77** (1996) 4828.

[42] M. García-Hernández, N. López, I. P. Moreira, J. Paniagua, and F. Illas, *Ab initio cluster model approach to the chemisorption of NH3 on Pt(111)*, Surf. Sci. **430** (1999) 18.

[43] D. C. Ford, Y. Xu, and M. Mavrikakis, *Atomic and molecular adsorption on Pt(111)*, Surf. Sci. **587** (2005) 159.

[44] G. Novell-Leruth, A. Valcárcel, A. Clotet, J. M. Ricart, and J. Pérez-Ramírez, *DFT characterization of adsorbed NH(x) species on Pt(100) and Pt(111) surfaces.* J. Phys. Chem. B **109** (2005) 18061.

[45] G. Novell-Leruth, A. Valcárcel, J. Pérez-Ramírez, and J. M. Ricart, *Ammonia Dehydrogenation over Platinum-Group Metal Surfaces. Structure, Stability, and Reactivity of Adsorbed NH x Species*, J. Phys. Chem. C **111** (2007) 860.

[46] W. Offermans, A. Jansen, and R. van Santen, *Ammonia activation on platinum {111}: A density functional theory study*, Surf. Sci. **600** (2006) 1714.

[47] K. Rasim, M. Bobeth, W. Pompe, and N. Seriani, *A microkinetic model of ammonia decomposition on a Pt overlayer on Au(111)*, J. Mol. Catal. A **325** (2010) 15.

[48] S. Zurita, J. Rubio, and F. Illas, *Active sites of Pt surfaces from ab initio cluster model molecular electrostatic potential maps*, Electrochim. Acta **41** (1996) 2275.

[49] I. Farbman, M. Asscher, and A. Ben-Shaul, *Effects of adsorbate lateral repulsion on desorption and diffusion kinetics studied by Monte Carlo simulations*, en, J. Chem. Phys. **104** (1996) 5674.

[50] M. Gajdoš, J. Hafner, and A. Eichler, *Ab initio density-functional study of NO on close-packed transition and noble metal surfaces: I. Molecular adsorption*, J. Phys.: Cond. Matt. **18** (2006) 13.

[51] R. Getman and W. Schneider, *DFT-Based Characterization of the Multiple Adsorption Modes of Nitrogen Oxides on Pt(111)*, J. Phys. Chem. C **111** (2007) 389.

[52] Z.-H. Zeng, J. L. F. Da Silva, H.-Q. Deng, and W.-X. Li, *Density functional theory study of the energetics, electronic structure, and core-level shifts of NO adsorption on the Pt(111) surface*, Phys. Rev. B **79** (2009) 205413.

[53] Z.-H. Zeng, J. L. F. Da Silva, and W.-X. Li, *Theory of nitride oxide adsorption on transition metal (111) surfaces: a first-principles investigation.* PCCP **12** (2010) 2459.

[54] Z.-H. Zeng, J. L. F. Da Silva, and W.-X. Li, *Density functional theory and ab initio molecular dynamics study of NO adsorption on Pd(111) and Pt(111) surfaces*, Phys. Rev. B **81** (2010) 1.

[55] M. Matsumoto, N. Tatsumi, and K. Fukutani, *Dynamical low-energy electron diffraction analysis of the structure of nitric oxide on Pt (111)*, Surf. Sci. **513** (2002) 485.

[56] M. Kiskinova, G. Pirug, and H. Bonzel, *No adsorption on Pt(111)*, Surf. Sci. **136** (1984) 285.

[57] E. Arunan, G. R. Desiraju, R. A. Klein, J. Sadlej, S. Scheiner, I. Alkorta, D. C. Clary, R. H. Crabtree, J. J. Dannenberg, P. Hobza, H. G. Kjaergaard, A. C. Legon, B. Mennucci, and D. J. Nesbitt, *Defining the hydrogen bond: An account (IUPAC Technical Report)*, Pure and Applied Chemistry **83** (2011) 1619.

[58] E. Arunan, G. R. Desiraju, R. A. Klein, J. Sadlej, S. Scheiner, I. Alkorta, D. C. Clary, R. H. Crabtree, J. J. Dannenberg, P. Hobza, H. G. Kjaergaard, A. C. Legon, B. Mennucci, and D. J. Nesbitt, *Definition of the hydrogen bond (IUPAC Recommendations 2011)*, Pure and Applied Chemistry **83** (2011) 1637.

[59] N. Marzari and D. Vanderbilt, *Maximally localized generalized Wannier functions for composite energy bands*, Phys. Rev. B **56** (1997) 12847.

[60] G. Román-Pérez and J. Soler, *Efficient Implementation of a van der Waals Density Functional: Application to Double-Wall Carbon Nanotubes*, Phys. Rev. Lett. **103** (2009) 096102.

[61] T. Thonhauser, V. R. Cooper, S. Li, A. Puzder, P. Hyldgaard, and D. C. Langreth, *Van der Waals density functional: Self-consistent potential and the nature of the van der Waals bond*, Phys. Rev. B **76** (2007) 125112.

[62] S. Grimme, *Semiempirical GGA-type density functional constructed with a long-range dispersion correction.* Journal of computational chemistry **27** (2006) 1787.

[63] T. Shimada, B. S. Mun, I. F. Nakai, A. Banno, H. Abe, Y. Iwasawa, T. Ohta, and H. Kondoh, *Irreversible Change in the NO Adsorption State on Pt(111) under High Pressure Studied by AP-XPS, NEXAFS, and STM †*, J. Phys. Chem. C **114** (2010) 17030.

Part II

Inelastic electron tunneling spectroscopy on single molecules

Chapter 5

How to probe the vibrational modes of one molecule

A scanning tunneling microscope can provide atomically-resolved images of a surface, and since its invention in 1981 [1] many efforts have been directed to devise new, "smart" ways to use it, attempting to get as much information as possible with the same spatial resolution. In this way, the standard topographic measurements were gradually complemented with all sorts of "local spectroscopies" [2]. These developments were also driven by the fact that the STM lacks direct chemical sensitivity: the images result form the convolution of the electronic structure of the tip and the sample, and unraveling the chemical nature of an adsorbed species from its STM appearance is an highly non-trivial task, usually requiring the support of theoretical methods [3, 4].

During my PhD I introduced for the first time in our laboratory the Inelastic Electron Tunneling Spectroscopy technique with an STM (STM-IETS), which allows for measuring excitation energies of single atomic or molecular species adsorbed on a surface, such as the vibrational modes of a molecule [5] or the flipping of a single magnetic moment [6]. I focused in particular on vibrations, which are particularly interesting from the catalysis point of view: the vibrational spectrum of a molecule is not only a fingerprint of its chemical identity, but allows also to probe its interactions with the local environment.

In this chapter I will first introduce the physical basis of IETS and present the measurement technique, detailing some of the key issues that I had tackle in order to successfully perform these measurements. The aim of this chapter is twofold: first, I hope that this technical survey will help the reader to get an organic understanding of the various aspects of STM-IETS; second, I want to document the milestones of the path I followed, in order to allow the reader interested in approaching this technique to follow a more direct path. For the same reason, I chose to report in some detail – in figure captions and in footnotes – the experimental conditions and the particular settings used for the instruments.

An STM-IETS measurement involves positioning the STM tip over the molecule

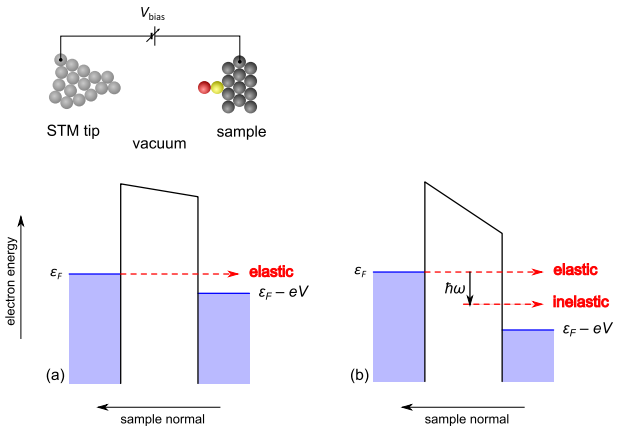

Figure 5.1: Electron tunneling trough an adsorbed molecule. The density of electronic states in the energy is schematically represented in blue, with ϵ_F denoting the Fermi energy and V the sample bias voltage. The black line represents the potential energy for the electrons. (a) Elastic tunneling, where the filled initial state in the tip and the empty final state in the sample have the same energy. (b) Inelastic tunneling: if the energy $e|V|$ of the tunneling electrons is greater than the quantum $\hbar\omega$ of an excitation, an electron can transfer part of his energy to it, ending up in an empty state at lower energy. This process corresponds to a new, inelastic tunneling channel.

of interest and then sweeping the bias voltage within the range of the relevant excitations. The majority of the electrons tunnel *elastically* from a state at a certain energy in the tip to a state at the same energy in the sample (figure 5.1a), but if the energy $e|V|$ of the tunneling electrons is greater than the quantum $\hbar\omega$ of an excitation, an electron can transfer part of his energy to it, ending up in an empty state at lower energy (figure 5.1b). In this way, when the threshold $e|V| = \hbar\omega$ is crossed, a new *inelastic* tunneling channel opens, adding its conductance to the elastic one. This conductance increase is detected as a kink in the $I(V)$ characteristic if the tunneling junction, or equivalently as a step in its first derivative $\mathrm{d}I/\mathrm{d}V(V)$, or as a peak in the second derivative $\mathrm{d}^2I/\mathrm{d}V^2(V)$ (figure 5.2). These features mark the characteristic energy of the underlying excitation, and are symmetric with respect to the sample bias, since the inelastic process can be triggered indifferently by electrons tunneling from the tip to the sample or *vice versa*.

The invention of this technique was inspired by the conventional inelastic electron tunneling spectroscopy [7–9], where the same measurement is performed on a different tunneling junction: the tip-molecule-sample system is replaced by a small quantity of analyte adsorbed on a tiny insulating layer sandwiched between two metal electrodes. The main strength of the conventional IETS when compared to the other vibrational spectroscopies is its excellent sensitivity, allowing to detect as few as 10^9 molecules. To this respect, STM-IETS reaches the physical limit: the

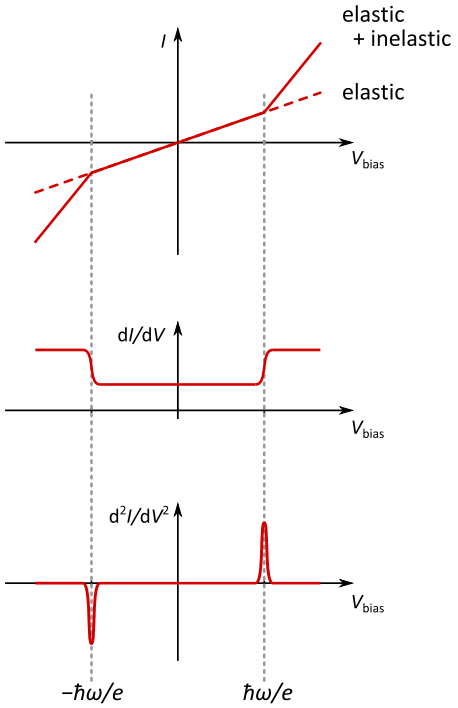

Figure 5.2: Schematic effect of an inelastic process on the $I(V)$ characteristic of a tunneling junction. The threshold $e|V| = \hbar\omega$ of an inelastic excitation is marked by symmetric features in the $I(V)$ curve and in its derivatives. The conductance change is grossly exaggerated.

single chemical bond [10].

This sensitivity comes to a cost: as can be expected form a technique collecting its signal form a single molecule, the signal-to-noise ratio of STM-IETS is particularly poor, making it exceptionally challenging and time-consuming. Experiments report relative variations of the differential conductance $\mathrm{d}I/\mathrm{d}V(V)$ at a vibrational threshold which rarely exceed 10%, being usually much less. Moreover, the detected modes are only a small subset of the vibrational spectrum of the molecule-surface system. This behavior has been theoretically rationalized [11, 12], and arises from the competition of two different processes: at the threshold for a vibrational excitation a new inelastic channel opens up, but the conductance of the elastic one is instead reduced. The magnitude of the observed features is the balance between these two canceling effects, and if it is smaller than the experimental sensitivity, the

threshold goes undetected. It might also happen that the balance is negative: STM-IETS on O_2/Ag(110) shows indeed a conductance *decrease* at a vibrational threshold [13].

Due to this effect, the number of systems where this technique can be successfully applied, together with the quantity and quality of the information it can provide, critically depends on the achieved signal-to-noise ratio: an higher SNR allows weaker features to be detected, and reduces the time needed to perform a measurement. Indeed, most of the work required to introduce this technique in our laboratory was spent in optimizing its SNR. This effort required a thorough understanding of many technical issues of STM-IETS, from the internals of a lock-in amplifier, to the quantitative characterization of the various contributions to the measured noise. I report in the following sections the key steps of this optimization, arranging them along two main themes: section 5.2 describes various methods to increase the signal, together with their intrinsic drawbacks; section 5.3 shows how it is possible to reduce the noise, i. e. the standard deviation of the STM-IETS signal.

5.1 The STM-IETS technique

The direct differentiation of the $I(V)$ curve to obtain $\mathrm{d}^2I/\mathrm{d}V^2(V)$ is unfeasible due to the poor signal-to-noise ratio of the $I(V)$ spectrum itself. For this reason, a phase-sensitive detection technique is commonly used. A small sinusoidal modulation of frequency f_m is added to the bias voltage, and a lock-in amplifier is used to extract form the time-dependent tunneling current the real part of its Fourier component at twice the modulation frequency. As will be discussed in detail in chapter 6, this quantity is strictly related to the second derivative $\mathrm{d}^2I/\mathrm{d}V^2(V)$. Internally, the lock-in simply multiplies the current signal by a sinusoidal reference at $2f_\mathrm{m}$ and then low-passes the result. The multiplication with the sinusoid shifts the Fourier spectrum of the input: part of the power previously at $2f_\mathrm{m}$ ends up at DC,[1] where it is then isolated form the noise by the low-pass filter. For the interested reader, reference [14] is an introductory but detailed explanation of the internals of a lock-in amplifier.

Entering into more detail, an STM-IETS measurement starts after having positioned the STM tip over a molecule, by allowing the feedback loop of the microscope to fix the tip-sample distance in order to get the desired tunneling current at the sample bias used. The feedback loop is then turned off, the modulation is added to the sample bias, and the latter is ramped in steps while recording the corresponding lock-in output. After each bias ramp the measurement is repeated, sweeping the voltage in the opposite direction: the comparison of the "forward" with the "backward" spectra allows to spot possible artifacts related to residual thermal drift of the tip-to-sample distance (as in figure 5.10), or to insufficient settling of the lock-in filter. The described measurement sequence is then repeated and the resulting spectra

[1] The remnant ending up at $4f_\mathrm{m}$. This is easily seen by considering the trigonometric identity $\cos(2\pi\, 2f_\mathrm{m}\, t)\, \cos(2\pi\, 2f_\mathrm{m}\, t) = \frac{1}{2} + \frac{1}{2}\cos(2\pi\, 4f_\mathrm{m}\, t)$.

are averaged together until the desired signal-to-noise ratio is achieved, checking from time to time for the possible lateral drift of the STM tip with respect to the surface. The measurement carried out on a molecule is then repeated on the bare surface and the two spectra are eventually subtracted, in order to highlight the features related to the molecule itself.

Figure 5.3 shows a typical result of the above procedure, performed on a carbon monoxide molecule adsorbed on a copper (110) surface. The antisymmetric peaks at ±35 meV originate from the hindered rotation of the molecule [15], whereas the peaks at −4 meV / +6 meV are relate to the hindered translation [16]. The position of the latter peaks is strongly influenced by the modulation broadening (section 5.2.2), which convolves them with the surrounding spectral features: a proper antisymmetric feature at ±5 meV is indeed obtained only at low modulation amplitudes ($V_\mathrm{m} = 1.3\,\mathrm{mV_{pk}}$).

5.2 Improving the IETS signal

5.2.1 Tunneling resistance

The signal level can be increased by imposing a higher tunneling current at the beginning of the spectroscopy operation, in order to bring the tip closer to the sample. In this way, the tunneling resistance is reduced, and the same modulation voltage will result in a stronger modulated current, and thus in an higher signal at $2f_\mathrm{m}$. The limit in this approach is set by the fact that reduced tip-to sample distances and high tunneling currents can induce phenomena such as the desorption of the molecule of interest, or its dissociation, diffusion on the surface, binding to the STM tip, *et cetera*. These phenomena can be triggered by various mechanisms, such as the chemical interaction with the atoms of the tip, or the electric field in the tunneling junction, or the energy deposited into the vibrational modes of the molecule by the inelastic electrons, and are the base of the controlled manipulation and chemistry of single molecules [17]. The maximum usable current depends on the system under study, and typically ranges from tens of nanoamperes, as in the case of CO/Cu(110), down to few picoamperes, for weakly-bound organic molecules.

Actually, a higher tunneling current results also in an increased noise level, but overall the signal-to-noise ratio increases, as can be seen in figure 5.4, which reports the signal and the noise of a STM-IETS measurement on CO/Cu(110) as a function of the tunneling current. The IETS signal is linear with the tunneling current, consistently with a picture where a fixed fraction of the tunneling electrons are scattered inelastically, and was fit with $S(I) = a_S\, I$. Conversely, the noise shows two contributions, one linear in I and the other one independent from I, and was fit with a quadrature sum $N(I) = \sqrt{(a_N\, I)^2 + b_N^2}$. The "SNR" panel shows a plot of the ratio of these two functions, which is 0 for $I = 0$, and approaches the positive value a_S/a_N for $I \to +\infty$.[2] In conclusion, the SNR increases with the tunneling current because

[2]The fit results are $a_S = (3.73 \pm 0.03) \times 10^{-3}\,\mathrm{A_{RMS}/A}$, $a_N = (0.081 \pm 0.002) \times 10^{-3}\,\mathrm{A_{RMS}/A}$,

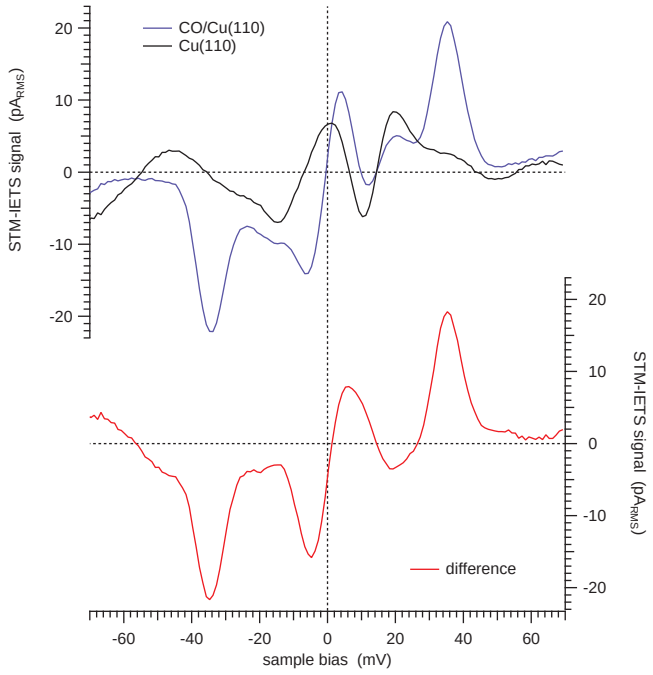

Figure 5.3: STM-IETS spectrum of CO/Cu(110). The upper panel shows the measurements on the adsorbed molecule and on the bare surface, the lower one their difference. The antisymmetric peaks at ±35 mV marks the CO hindered rotation, the ones at −4 meV / +6 meV the hindered translation. Tip stabilized at $V = -70\,\mathrm{mV}$, $I = 30\,\mathrm{nA}$, modulation of $V_\mathrm{m} = 6.3\,\mathrm{mV_{pk}}$ at $f_\mathrm{m} = 4216\,\mathrm{Hz}$, using the bipolar pulse waveform described in chapter 6. The measurement required one hour, being the average of 60 spectra on the molecule and 60 on the copper surface. IETS signal was sampled in 1 mV steps, stabilizing the lock-in low-pass filter (fourth-order RC with 30 ms time constant, having a roll-off of 24 dB/oct, $f_{-3\,\mathrm{dB}} = 2.31\,\mathrm{Hz}$, $\mathrm{ENBW_{LPF}} = 2.60\,\mathrm{Hz}$) for 210 ms after each voltage step, before acquiring data for 5 ms.

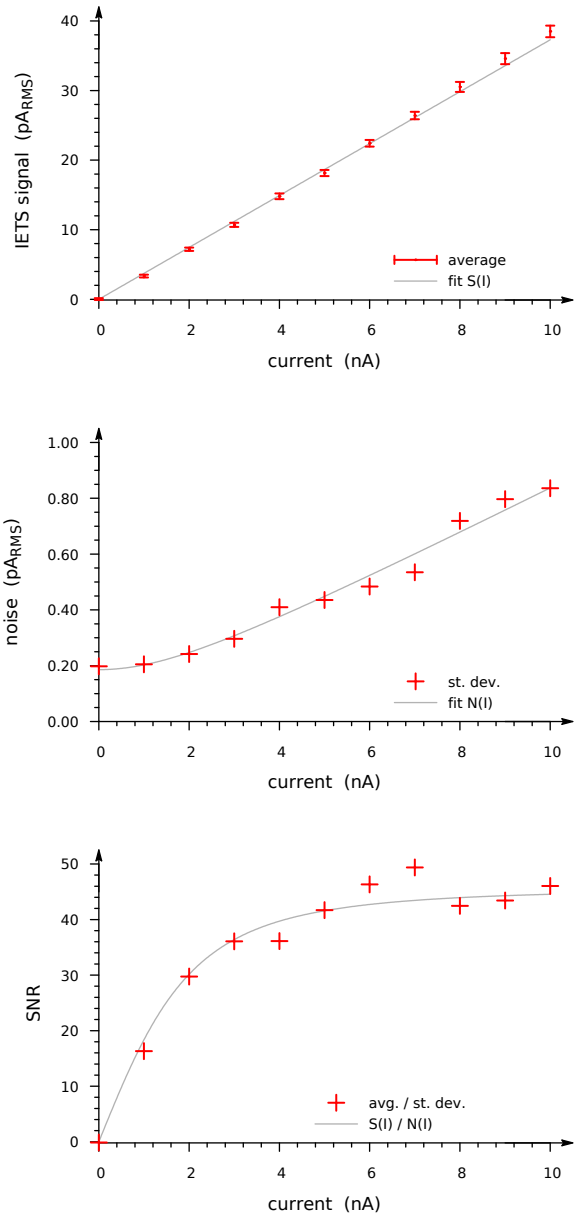

Figure 5.4: Signal, noise, and signal-to-noise ratio as a function of the tunneling current, in a STM-IETS measurement of the hindered rotation feature of CO/Cu(110). At each current, the IETS signal was sampled for 12 s: the "signal" panel reports the average of the time series at each current (error-bars: ±1 standard deviation) , the "noise" panel their standard deviations, and the "SNR" panel the ratio between the two. Fits are described in the text. Bias voltage $V_0 = +36$ mV, sinusoidal modulation of $V_m = 9.3\,mV_{pk}$ at $f_m = 1656$ Hz.

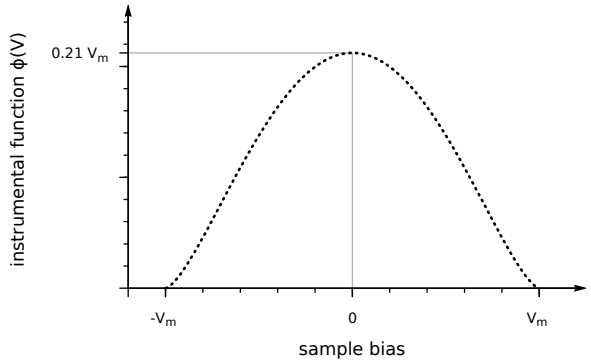

Figure 5.5: Instrumental function $\phi(V)$ of a lock-in amplifier detecting at twice the modulation frequency, using a sinusoidal modulation of amplitude V_m.

the noise has a component which is independent from I. For this reason, STM-IETS measurements should be made at the maximum current the system under study can withstand.

5.2.2 Modulation amplitude

Another obvious way to increase the detected IETS signal is to employ a stronger modulation voltage, but at the price of a reduced resolution along the V axis: a compromise has thus to be made between signal intensity and experimental resolution. This *modulation broadening* was rationalized by Klein and co-workers [18], who demonstrated that the lock-in output at twice the modulation frequency can be expressed as a convolution of the second derivative $\mathrm{d}^2I/\mathrm{d}V^2(V)$ of the current with respect to the bias voltage, with an instrumental function ϕ:

$$\mathrm{out}_2(V_0) = \int_{-\infty}^{+\infty} \mathrm{d}x \; \frac{\mathrm{d}^2 I}{\mathrm{d}V^2}(V_0 - x)\; \phi(x) \tag{5.1}$$

The instrumental function was found to be

$$\phi(V) = \begin{cases} \dfrac{2}{3\pi}\; V_\mathrm{m} \left(1 - \left(\dfrac{V}{V_\mathrm{m}}\right)^2\right)^{\frac{3}{2}} & \text{for } V \in [-V_\mathrm{m}; V_\mathrm{m}] \\ 0 & \text{otherwise} \end{cases} \tag{5.2}$$

and is plotted in figure 5.5.

From the above expression is evident that both the height and the width of ϕ scale with the modulation amplitude V_m: this shows clearly why boosting V_m

$b_N = (0.18 \pm 0.02)\,\mathrm{pA_{RMS}}$, $a_S/a_N = 46 \pm 1$. The non-linear least squares Marquardt-Levenberg algorithm was employed, as implemented in the gnuplot software.

increases the output signal, but also spoils the voltage resolution. In chapter 6 I investigate the origin of this broadening, discovering that it is indeed possible to reduce it by employing a tailored modulation function instead of the commonly-used sinusoid. This new modulation scheme increases both the energy resolution and the signal level of the measurement, and can easily be applied not only to STM-IETS, but also to any experimental situation where a lock-in amplifier is used to measure a second derivative.

Modulation is the most important factor contributing to STM-IETS resolution, but not the only one: any effect which smears in energy the electron distribution of the the sample and the tip will indeed result in a spectral broadening. For instance, if the sample and the tip are not superconducting, temperature contributes with a FWHM of $5.4\,k_{\mathrm{B}}T$ [19], which however is only 2.3 meV at 5 K. High-frequency noise in the bias voltage signal can also have a similar effect, and is eliminated by low-pass filtering.

5.3 Reducing the noise

The noise of a STM-IETS measurement is the noise at the output of the lock-in amplifier, originating from the fluctuations of its input signal: the STM tunneling current. Many contributions concur to the tunneling current noise, such as:

- unavoidable fundamental effects, such as the shot noise of the current, or the thermal Johnson-Nyquist noise of the feedback resistor of the current amplifier;
- mechanical vibrations that modulate the tip-to sample distance, and thus the tunneling resistance. These include sound waves that can propagate down to the tunneling junction, originating for instance from the vacuum pumps of the STM chamber, from the voices of the people in the room, from air draughts, *etc.*
- electromagnetic radiation, that can couple to the cables which carry the tunneling current outside the vacuum chamber;
- an improper electrical grounding of the experimental apparatus;
- the digitizing noise of the ADC sampling the current signal.

Among these, some will be dominant, others negligible. In order to sort out the most relevant contributions, these effects were characterized by measuring the Power Spectral Density $\mathrm{PSD}(f)$ of the $I(t)$ signal, which allowed also to get a prompt, quantitative feedback on the various attempts to reduce the noise level. In the following I will quickly review its definition, physical meaning and relation with STM-IETS noise; the uninterested reader can skip directly to formula 5.3.

To define the PSD it is useful to define first the truncated Fourier transform $X_T(f)$ of a signal $x(t)$

$$X_T(f) = \int_{-\frac{T}{2}}^{\frac{T}{2}} \mathrm{d}t \; x(t) \; e^{-2\pi i f t}$$

The PSD is then defined as

$$\mathrm{PSD}(f) = \lim_{T \to +\infty} \mathbf{E}\left[\frac{1}{T} \left|X_T(f)\right|^2\right]$$

where $\mathbf{E}$ denotes the ensemble average over different realizations of the random process $x(t)$. This definition can be understood by considering that the squared modulus of the Fourier transform $\left|X(f)\right|^2$ is proportional to the energy density at the frequency f carried by the signal $x(t)$. The factor $\frac{1}{T}$, together with the truncation of the Fourier transform and the limit $T \to +\infty$, are needed to define a power (energy per unit time). The physical dimensions of the PSD are $[x]^2/\mathrm{Hz}$, where $[x]$ is the dimension of $x(t)$, and it can be interpreted as the average power per unit frequency carried by the signal itself. Indeed, the total power of $x(t)$, which is defined as its variance, is given by

$$\sigma_x^2 = \int_{-\infty}^{+\infty} \mathrm{d}f \; \mathrm{PSD}(f)$$

If the signal $x(t)$ is fed into the input of a linear system, such as a lock-in amplifier, the variance of the output is instead given by

$$\sigma^2 = \int_{-\infty}^{+\infty} \mathrm{d}f \; \mathrm{PSD}(f) \; |H(f)|^2$$

In words, the system collects noise only in the bandwidth defined by its frequency response $H(f)$. With this respect, the lock-in amplifier acts as a tunable band-pass filter: its frequency response is non-negligible only in a very narrow band[3] around the modulation frequency f_m, and both the bandwidth and f_m can be chosen by the experimenter. The previous equation can thus be approximated by

$$\begin{aligned} \sigma^2 &\approx \mathrm{PSD}(f_\mathrm{m}) \int_{-\infty}^{+\infty} \mathrm{d}f \; |H(f)|^2 \\ &= \mathrm{PSD}(f_\mathrm{m}) \; \mathrm{ENBW} \end{aligned}$$

where the Eqivalent Noise BandWidth is defined as $\mathrm{ENBW} = \int_{-\infty}^{+\infty} \mathrm{d}f \; |H(f)|^2$. Eventually, defining the Linear Spectral Density

$$\mathrm{LSD}(f) = \sqrt{\mathrm{PSD}(f)}$$

[3] For instance, the STM-IETS measurements presented in this work were acquired with a lock-in -3 dB bandwidth of 4.62 Hz, corresponding to a -20 dB bandwidth of 15.60 Hz, and to a single-sided equivalent noise bandwidth $\mathrm{ENBW}_\mathrm{LPF} = 2.60$ Hz.

the standard deviation of the output, i. e. the measurement noise, is given by

$$\sigma = \mathrm{LSD}(f_\mathrm{m})\ \sqrt{\mathrm{ENBW}}$$

The detection bandwidth of a lock-in amplifier is determined by its low-pass filter, in particular we have

$$\sigma = \mathrm{LSD}_\mathrm{ss}(f_\mathrm{m})\ \sqrt{\mathrm{ENBW}_\mathrm{LPF}} \tag{5.3}$$

where LSD_ss is the single-sided linear spectral density of the input signal,[4] and $\mathrm{ENBW}_\mathrm{LPF}$ the single-sided equivalent noise bandwidth of the low-pass filter.[5] This definition also accounts for the fact that the input noise power is split between the in-phase and quadrature outputs of the lock-in. From now on we will refer to single-sided quantities only, dropping the "ss" subscript.

The last equation shows that two factors concur to the measurement noise σ: the spectral density $\mathrm{LSD}(f_\mathrm{m})$ of the current signal *at the modulation frequency* f_m, and a bandwidth $\mathrm{ENBW}_\mathrm{LPF}$ dependent on the lock-in settings. Consequently, σ can be lowered in two ways: by reducing $\mathrm{LSD}(f_\mathrm{m})$, or by reducing $\mathrm{ENBW}_\mathrm{LPF}$. The latter strategy is discussed in section 5.3.2, and comes down to choosing a lock-in filter with a narrower frequency response. This however will have a slower behavior in the time domain, requiring thus longer measurement times. The former strategy is discussed in next section, and can be pursued either by choosing f_m to minimize $\mathrm{LSD}(2f_\mathrm{m})$, or by reducing the LSD baseline.

5.3.1 Lower noise level

The spectral density of the tunneling current has been estimated via the Welch's method, as described in reference [20]: after having sampled $I(t)$ with the STM electronics, the resulting time series has been divided in overlapping segments which were then Fourier-transformed and averaged.[6] To obtain a reliable measurement, it is of paramount importance to avoid drifts in the average value of the tunneling current, since there are noise components that are proportional to it, as was already pointed out in section 5.2.1. To this end, we used the feedback loop of the STM to automatically compensate for variations in the tip-to-sample distance. Its action will, however, modify the low-frequency part of the spectrum: for this reason we employed the minimum possible gain setting, verifying that in this way only the frequency bins below 50 Hz were affected, and only marginally.

[4] All the spectral quantities introduced up to now are double-sided, involving also negative frequencies. Since the Fourier transform of real signals is Hermitian $X(-f) = X(f)^*$, it is customary to fold the PSD on the positive side of the frequency axis, introducing the single-sided quantity $\mathrm{PSD}_\mathrm{ss}(f) = \mathrm{PSD}(f) + \mathrm{PSD}(-f) = 2\,\mathrm{PSD}(f)$, with $f \geq 0$. The total power of the signal is now given by $\sigma_x^2 = \int_0^{+\infty} \mathrm{d}f\ \mathrm{PSD}_\mathrm{ss}(f)$.

[5] This is the quantity usually reported, defined as $\mathrm{ENBW}_\mathrm{LPF} = \int_0^{+\infty} \mathrm{d}f\ |H(f)|^2$.

[6] The current was sampled for typically 21 s at a sampling frequency of 100 kHz (2^{21} samples), the overlap between segments was 50%, and a linear background was subtracted from each segment to remove the DC component. Hann windowing was used to reduce the spectral leakage, accounting for its ENBW.

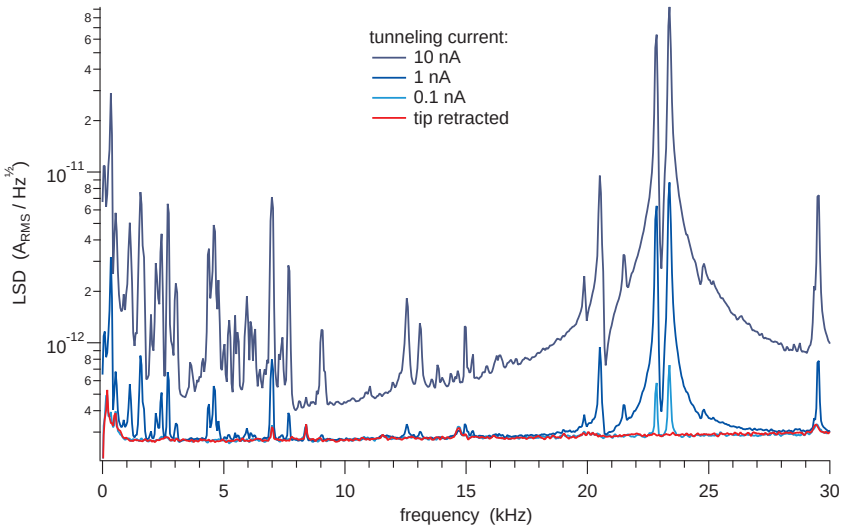

Figure 5.6: Linear Spectral Density of the tunneling current signal for various values of the average current. Measurements were taken on a clean Au(111) surface at 5 K with a Femto DPLCA-200 current amplifier (gain 10^7 V/A, bandwidth 50 kHz) at a bias voltage $V = 100$ mV.

Figure 5.6 compares the Linear Spectral Density acquired at different values of the DC tunneling current. As we already noticed in section 5.2.1, at low currents the main contribution to the LSD is the baseline of the current amplifier, which is instead negligible at high currents. The dynamic range of the LSD is quite high, so by properly choosing the modulation frequency the noise floor can be easily reduced by a factor of two. It is to be noted that the low-frequency region should be avoided, since the PSD of the tunneling current of an STM has a $1/f$-like behavior [21, 22].

From the spectroscopy point of view, we are not immediately interested in eliminating the various instabilities that appear as peaks in the spectrum, such as the mechanical longitudinal eigenmode of the piezoelectric tube scanner around 23 kHz: these can be avoided by a proper choice of the modulation frequency. A significant benefit would instead come from lowering the LSD baseline, and to this end a very effective optimization turned out to be the replacement of the standard Omicron SPM PRE4 current amplifier with a customized version of the commercial Femto DLPCA-200. Figure 5.7 compares the noise curves of the two amplifiers at various gain settings and at a tunneling current of 1 nA. With the Omicron PRE4, STM-IETS measurements at this current would have been performed at $2f_m = 1850$ Hz, where the noise level was around 110 $\mathrm{fA_{RMS}}/\sqrt{\mathrm{Hz}}$. With the new Femto DLPCA-200, the same measurements can be carried out at a noise level of 48 $\mathrm{fA_{RMS}}/\sqrt{\mathrm{Hz}}$ at $2f_m = 6600$ Hz, and indeed the DLPCA-200 outperformed the Omicron amplifier at all the considered tunneling currents. The characterization of the noise performance of the amplifiers is summarized in table 5.1, which can be used as a reference

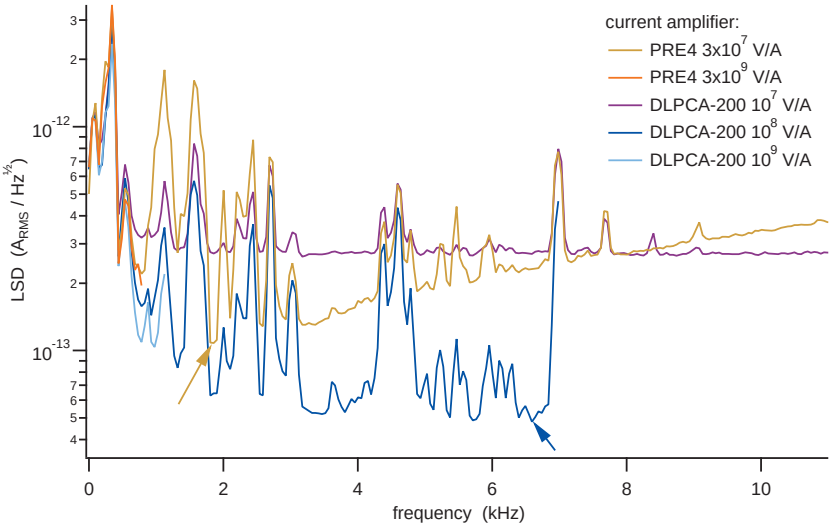

Figure 5.7: Linear Spectral Density of the tunneling current, that allows comparing the noise performance of two current amplifiers at various gain settings. Measurements were taken on a clean Au(111) surface at 5 K, with a tunneling current of 1 nA and a bias voltage $V = 100\,\text{mV}$. By replacing the Omicron PRE4 with a Femto DLPCA-200 the noise floor at this tunneling current has been lowered from 110 $\text{fA}_{\text{RMS}}/\sqrt{\text{Hz}}$ (yellow arrow) to 50 $\text{fA}_{\text{RMS}}/\sqrt{\text{Hz}}$ (blue arrow). Only the part of the LSD inside each amplifier's bandwidth is shown.

Table 5.1: Gain settings and optimal measurement frequency $2f_{\text{m}}$ for different values of the tunneling current, using the Femto DLPCA-200 current amplifier. The reported minimum-noise frequency should be regarded as an indication of a region where to look for the actual minimum.

current [nA]	gain [V/A]	bandwidth [kHz]	$2f_{\text{m}}$ [kHz]	LSD($2f_{\text{m}}$) [$\text{fA}_{\text{RMS}}/\sqrt{\text{Hz}}$]
100 pA	10^9	1.1	0.95	11
1 nA	10^8	7	6.6	48
10 nA	10^8	7	6.6	305
above	10^7	50	49.4	–

in choosing the best amplifier gain and measurement frequency $2f_{\text{m}}$ for a given tunneling current. Needless to say, the values reported pertain to our system only; for another STM in a different environment the stated characterization has to be repeated.

Another attempt to reduce the noise level consisted in isolating the vacuum chamber from the ground by means of four pneumatic damping legs (Newport Stabilizer I-2000). The LSD analysis showed however that their overall effect was detri-

mental: when the experimental system is floated on the legs, a very strong feature appears in the tunneling current spectrum at frequencies near $f_{\text{legs}} = 2.6\,\text{Hz}$ (figure 5.8). This is probably due to the combined effect of the damping legs and of the spring suspension of the STM head, both of which having a resonance at those frequencies. Due to this effect, the current is now modulated both by a voltage modulation at frequency f_{m} and by a conductance modulation at f_{legs},

$$\begin{aligned} I &= SV \\ &= S_0 \cos(2\pi f_{\text{legs}} t)\ \ (V_0 + V_{\text{m}} \cos(2\pi f_{\text{m}} t)) \\ &= S_0 V_0 \cos(2\pi f_{\text{legs}} t) + S_0 V_{\text{m}} \left(\frac{1}{2} \cos\left(2\pi (f_{\text{m}} - f_{\text{legs}}) t\right) + \frac{1}{2} \cos\left(2\pi (f_{\text{m}} + f_{\text{legs}}) t\right) \right) \end{aligned}$$

where S is the first-order conductance of the tunneling junction. Overall, the spectrum shows two sidebands at $f_{\text{m}} - f_{\text{legs}}$ and $f_{\text{m}} + f_{\text{legs}}$, which enters the lock-in detection bandwidth in a $\mathrm{d}I/\mathrm{d}V(V)$ measurement. These sidebands are instead not detected around $2f$, probably because they fall under the noise baseline of this measurement. A general point is now evident: any mechanical noise close enough to DC will affect spectroscopy measurements, by giving rise to sidebands inside the detection bandwidth of the lock-in amplifier.

Other optimizations were also performed, such as shutting down the mechanical vacuum pumps, or removing the ground loops by using the vacuum chamber as a single ground point for all the electronic equipment. Since the spectrum of the tunneling current is very feature-rich, the effect of these modifications is better visualized by the relative difference of the PSDs after (a) and before (b) the modification $(\text{PSD}_{\text{a}} - \text{PSD}_{\text{b}})/\,\text{PSD}_{\text{a}}$. Preliminary, low-resolution measurements showed that the improvements are limited to certain frequency regions, as figure 5.9 illustrates for the case of the mechanical pumps. As such, these optimizations are of relative importance for the spectroscopic measurements, since those frequencies could already be avoided by a proper choice of the modulation frequency f_{m}.

5.3.2 Longer measurements

The obvious way to reduce the standard deviation of a measurement is to spend time in averaging. In a tunneling spectroscopy experiment this can be done in two different ways: by repeating multiple times the acquisition of the whole spectrum, or by spending more time in acquiring each of its points. In both cases the standard deviation is reduced proportionally to the square root of the time employed: repeating a measurement N times and averaging scales the associated standard deviation as $1/\sqrt{N}$, whereas by increasing the duration of a single voltage step one can use a lock-in filter with a longer settling time and thus a proportionally smaller ENBW: the standard deviation of the lock-in output goes as $\sqrt{\text{ENBW}}$ (equation 5.3).

The maximum duration of a measurement is limited by the stability of the tunneling junction: the tip has to stay still over the feature of interest for the whole duration of the measurement, usually minutes or hours. The stability requirements in the vertical and lateral directions are different: roughly speaking a lateral drift

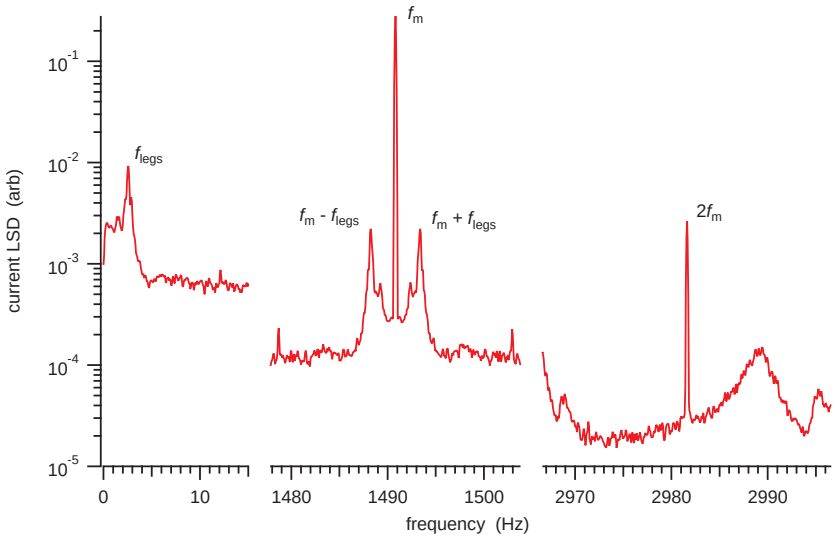

Figure 5.8: Linear spectral density of the tunneling current, showing the effect of the pneumatic damping legs. The feature at $f_{\text{legs}} \approx 2.6\,\text{Hz}$ is present only when the experimental system is floated on the legs. The same conductance modulation also gives rise to two sidebands around the $\mathrm{d}I/\mathrm{d}V$ signal at $f_{\text{m}} = 1490.8\,\text{Hz}$, whereas no sidebands are visible around the $\mathrm{d}^2I/\mathrm{d}V^2$ signal at $2f_{\text{m}}$, lying probably under the noise floor of the measurement. The LSD was acquired over a CO molecule adsorbed on Cu(110), at a sample temperature $T = 5\,\text{K}$, tunneling current $I = 20\,\text{nA}$, bias voltage $V = 36\,\text{mV}$ (corresponding to the hindered rotation mode of CO), modulation amplitude $V_{\text{m}} = 9.4\,\text{mV}_{\text{pk}}$. The feedback loop of the STM was excluded, and the Kaiser window was employed ($\alpha = 12/\pi \approx 3.82$) to reduce the spectral leakage.

of 53 pm – the Bohr radius of hydrogen – is hardly ever a problem, since it would still leave the tip over the feature of interest. On the contrary, a vertical approach of the same magnitude would increase the conductance of the tunneling junction by a factor of three.[7] In an scanning tunneling spectroscopy measurement the effect of vertical drift can be characterized by first acquiring a spectrum and then repeating the same measurement sweeping the bias voltage in the opposite direction, as shown in figure 5.10, where the conductance increase due to the tip drifting towards the surface causes an increase of the I and $\mathrm{d}I/\mathrm{d}V(V)$ signals. If this effect is moderate, this procedure allows also to compensate to a certain extent by simply averaging the two measurements.

Since the vertical position of the tip is reset by the feedback loop at the beginning of each spectrum, the amount of vertical drift sets the maximum duration of the single voltage sweeps and thus the measurement time per point. Instead, the lateral drift dictates how many unattended repetitions of a measurement can be

[7] Assuming a reasonable value for $k = 1\,\text{Å}^{-1}$ in a tunneling conductance proportional to e^{-2kz}, where z is the vertical position of the tip, see section 2.2.2.

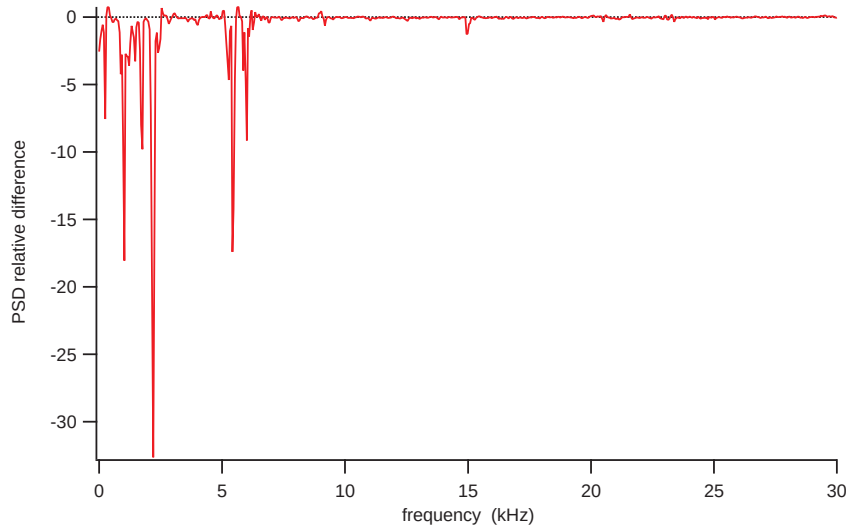

Figure 5.9: Relative difference $(\mathrm{PSD_a} - \mathrm{PSD_b})/\mathrm{PSD_a}$ of the current PSD after (a) and before (b) having switched off the mechanical vacuum pumps of the experimental camber. The PSD is reduced in certain frequency regions. Measurements were performed on a clean Au(111) surface at 5 K, with a tunneling current $I = 10\,\mathrm{nA}$ and a bias voltage $V = 100\,\mathrm{mV}$.

done before the experimenter has to manually re-center the tip over the feature of interest.

Different mechanisms contribute to the drift, such as the thermal expansion or contraction of the STM assembly (thermal drift), or the residual motion of the piezoelectric scanner after a displacement (piezo creep), in particular the motion towards the surface after having approached the tip into the tunneling position [23]. The former is greatly reduced by allowing the STM to thermalize at low temperatures, whereas the latter decreases logarithmically over time (see [24] and figure 5.11), compelling the experimenter to wait at least 45 min after an approach before being able to start a spectroscopy operation. Waiting is not the only possible solution: the amount of lateral drift during a spectroscopy operation can be quantified by comparing the subsequent and preceding topographic images [25]. This information allows both to track the feature of interest, in order to automatically repeat the measurement over it, and to correct for the drift while measuring. Similarly, the vertical drift speed can be measured by recording the coordinate z of the STM tip as a function of time, while keeping the tip still over the surface. Since the feedback loop compensates for the vertical drift by displacing the tip in order to maintain a constant tunneling current, the slope of the so measured $z(t)$ curve is (minus) the instantaneous drift velocity, which can then be corrected in the following measurements. Eventually, the piezo creep can be modeled and kept into account by a more refined piezo driving system [26, 27]. All these schemes are feasible and have been

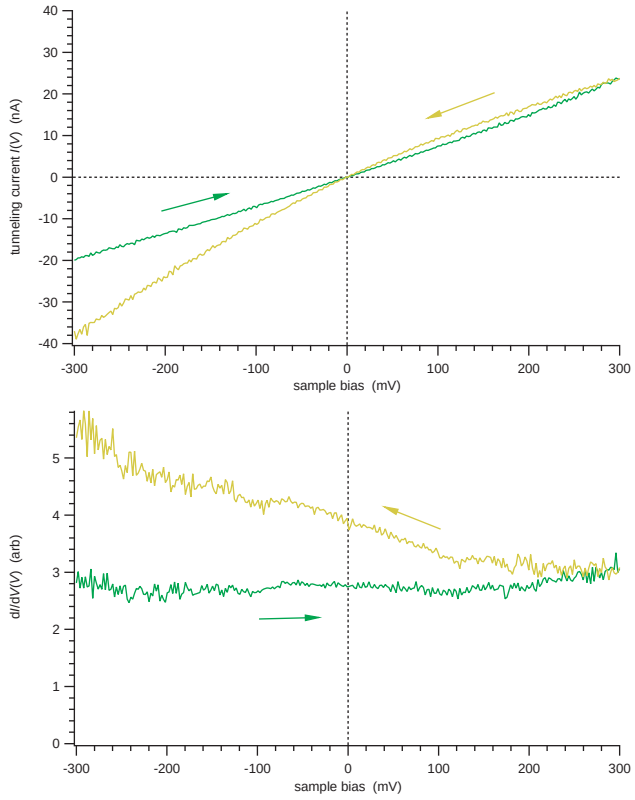

Figure 5.10: Vertical drift of the STM tip during a spectroscopy operation. The arrows indicate the direction of the voltage sweep. After a first spectrum (green) the measurement is repeated sweeping the voltage in the opposite direction (yellow). Since the tip is drifting towards the sample, both the current and its derivative are increasing.

demonstrated in literature, but they need a versatile enough STM control system on order to be effectively implemented and routinely employed. If this is done, the maximum duration of a measurement will then be imposed by the hold time of the cryostat that maintains the STM at low temperature.

5.4 Benchmarking the results

I conclude presenting one of the most challenging measurements that the above-described optimizations have made possible: STM-IETS of a cysteamine molecule adsorbed on the (111) surface of gold. This investigation relates to the field of organic-based electronics, where a fundamental issue is the control of the charge-transport at the interfaces between metal electrodes and functional organic films. To this end, the interposition of a Self-Assembled organic Monolayer (SAM) between the two can be used both to tailor the electronic properties of the interface –

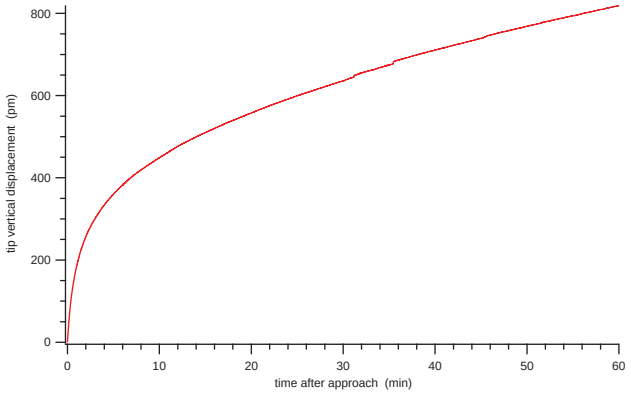

Figure 5.11: Vertical drift of the STM tip after having approached the sample. The graph shows the displacement imposed to the tip by the feedback loop of the STM in order to keep the tunneling current constant. The tip drift is equal and opposite in sign, and here would tend to move it closer to the sample.

by varying the SAM composition –, and to get a more ordered film with a reduced defect density. Cysteamine ($HS{-}CH_2{-}CH_2{-}NH_2$) is a small alkanethiol that can be used for this purpose: on gold surfaces, it easily forms a SAM by means of thiolate bonds (Au–S), whereas its amino group ($-NH_2$) can hydrogen-bind a second molecule that presents a carboxylic group (–COOH). Further details on the scientific background can be found in [28] and in the references therein.

Our ambitious goal was to characterize the low-coverage adsorption structures of this species: the STM images presented indeed a variety of morphologies, and we tried to assign them to the various possible adsorption conformations (single- or paired-molecules, upright or bent ones) by measuring their vibrational spectra. Unfortunately, this system proved to be particularly sensitive to reactions induced by inelastic tunneling: for bias voltages $|V| \gtrapprox 350\,\mathrm{mV}$ the diffusion of the molecule on the surface is easily induced. The measurement had thus to be performed at a maximum current of 15 pA, resulting in an STM-IETS signal of at most $14\,\mathrm{fA_{RMS}}$, more than 1500 times smaller than the $22\,\mathrm{pA_{RMS}}$ demonstrated in figure 5.3, and required a total measurement time of 18 h 52 min. Even at this low current, 9 spectra out of the 542 acquired on the molecule (1.7%) were expunged from the average, because the corresponding $I(V)$ and $\mathrm{d}I/\mathrm{d}V(V)$ measurements showed discontinuities, due probably to conformational changes of the molecule induced by the tunneling electrons. In order to confirm that the $\mathrm{d}^2I/\mathrm{d}V^2(V)$ characteristic of the tunneling junction was not permanently modified by these events, the spectra were split into four subsequently-acquired sets, checking then that the averages of the set were compatible with each other. The resulting STM-IETS spectrum is probably the average over different conformations of the molecule, and shows the C–H stretch feature at $(+358 \pm 3)\,\mathrm{meV}$ [29]. The same is absent at negative biases, due probably to a reduced cross section and the high background contribution from the gold

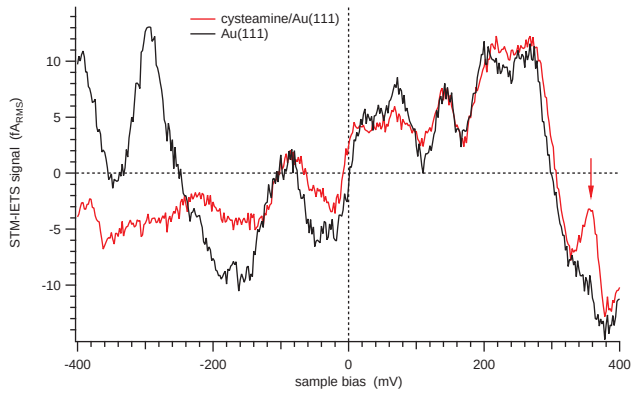

Figure 5.12: STM-IETS of cysteamine/Au(111). The arrow mark the C–H stretch at (+358 ± 3) meV. Tip stabilized at $V = -400\,\mathrm{mV}$, $I = 15\,\mathrm{pA}$, modulation of $V_\mathrm{m} = 18.9\,\mathrm{mV_{pk}}$ at $f_\mathrm{m} = 375\,\mathrm{Hz}$, using the bipolar pulse waveform described in chapter 6. The measurement on the molecule required 13 h 13 min, being the average of 533 individual spectra, whereas the one on the copper surface required 5 h 39 min, being the average of 232 spectra. IETS signal was sampled in 1 mV steps, stabilizing the lock-in low-pass filter (fourth-order RC with 30 ms time constant, having a roll-off of 24 dB/oct, $f_{-3\,\mathrm{dB}} = 2.31\,\mathrm{Hz}$, $\mathrm{ENBW_{LPF}} = 2.60\,\mathrm{Hz}$) for 180 ms after each voltage step, before acquiring data for 5 ms.

surface.

References

[1] G. Binnig, H. Rohrer, C. Gerber, and E. Weibel, *Surface Studies by Scanning Tunneling Microscopy*, Phys. Rev. Lett. **49** (1982) 57.

[2] R. Wiesendanger, *Scanning probe microscopy and spectroscopy: methods and applications*, Cambridge University Press, Cambridge 1994.

[3] W. Hofer, A. Foster, and A. Shluger, *Theories of scanning probe microscopes at the atomic scale*, Rev. Mod. Phys. **75** (2003) 1287.

[4] M.-L. Bocquet and B. Wang, *Metal-organic interaction probed by First Principles STM simulations*, Prog. Surf. Sci. **85** (2010) 435.

[5] B. C. Stipe, M. A. Rezaei, and W. Ho, *Single-Molecule Vibrational Spectroscopy and Microscopy*, Science **280** (1998) 1732.

[6] A. J. Heinrich, *Single-Atom Spin-Flip Spectroscopy*, Science **306** (2004) 466.

[7] R. Jaklevic and J. Lambe, *Molecular Vibration Spectra by Electron Tunneling*, Phys. Rev. Lett. **17** (1966) 1139.

[8] P. K. Hansma, *Inelastic electron tunneling*, Phys. Rep. **30** (1977) 145.

[9] K. Hipps and U. Mazur, *Handbook of Vibrational Spectroscopy*, ed. by J. M. Chalmers and P. R. Griffiths, John Wiley & Sons, Chichester 2002, chap. Inelastic electron tunneling spectroscopy.

[10] W. Ho, *Single-molecule chemistry*, J. Chem. Phys. **117** (2002) 11033.

[11] H. Ueba, T. Mii, and S. Tikhodeev, *Theory of inelastic tunneling spectroscopy of a single molecule – Competition between elastic and inelastic current*, Surf. Sci. **601** (2007) 5220.

[12] M. Paulsson, T. Frederiksen, H. Ueba, N. Lorente, and M. Brandbyge, *Unified Description of Inelastic Propensity Rules for Electron Transport through Nanoscale Junctions*, Phys. Rev. Lett. **100** (2008) 226604.

[13] J. Hahn, H. Lee, and W. Ho, *Electronic Resonance and Symmetry in Single-Molecule Inelastic Electron Tunneling*, Phys. Rev. Lett. **85** (2000) 1914.

[14] J. H. Scofield, *Frequency-domain description of a lock-in amplifier*, Am. J. Phys. **62** (1994) 129.

[15] L. J. Lauhon and W. Ho, *Single-molecule vibrational spectroscopy and microscopy: CO on Cu(001) and Cu(110)*, Phys. Rev. B **60** (12 1999) R8525.

[16] L. Vitali, R. Ohmann, K. Kern, A. Garcia-Lekue, T. Frederiksen, D. Sanchez-Portal, and A. Arnau, *Surveying Molecular Vibrations during the Formation of Metal–Molecule Nanocontacts*, Nano Letters **10** (2010) 657.

[17] S.-W. Hla, *Scanning tunneling microscopy single atom/molecule manipulation and its application to nanoscience and technology*, J. Vac. Sci. Technol. B **23** (2005) 1351.

[18] J. Klein, A. Léger, M. Belin, D. Défourneau, and M. J. L. Sangster, *Inelastic-Electron-Tunneling Spectroscopy of Metal-Insulator-Metal Junctions*, Phys. Rev. B **7** (6 1973) 2336.

[19] J. Lambe and R. Jaklevic, *Molecular Vibration Spectra by Inelastic Electron Tunneling*, Phys. Rev. **165** (1968) 821.

[20] G. Heinzel, A. Rüdiger, and R. Schilling, *Spectrum and spectral density estimation by the Discrete Fourier transform (DFT), including a comprehensive list of window functions and some new flat-top windows*, tech. rep., Hannover: Max-Planck-Institut für Gravitationsphysik, 2002.

[21] R. Möller, A. Esslinger, and B. Koslowski, *Thermal noise in vacuum scanning tunneling microscopy at zero bias voltage*, J. Vac. Sci. Technol. A **8** (1990) 590.

[22] H. Birk, M. de Jong, and C. Schönenberger, *Shot-Noise Suppression in the Single-Electron Tunneling Regime*, Phys. Rev. Lett. **75** (1995) 1610.

[23] S. O. R. Moheimani, *Invited Review Article: Accurate and fast nanopositioning with piezoelectric tube scanners: Emerging trends and future challenges*, Rev. Sci. Instrum. **79** (2008) 071101.

[24] S. Vieira, *The behavior and calibration of some piezoelectric ceramics used in the STM*, IBM J. Res. Dev. **30** (1986) 553.

[25] B. A. Mantooth, Z. J. Donhauser, K. F. Kelly, and P. S. Weiss, *Cross-correlation image tracking for drift correction and adsorbate analysis*, Rev. Sci. Instrum. **73** (2002) 313.

[26] H. Jung, J. Y. Shim, and D. Gweon, *New open-loop actuating method of piezoelectric actuators for removing hysteresis and creep*, Rev. Sci. Instrum. **71** (2000) 3436.

[27] D. Croft, G. Shed, and S. Devasia, *Creep, Hysteresis, and Vibration Compensation for Piezoactuators: Atomic Force Microscopy Application*, J. Dyn. Syst. **123** (2001) 35.

[28] A. Cossaro, D. Cvetko, and L. Floreano, *Amino–carboxylic recognition on surfaces: from 2D to 2D + 1 nano-architectures*, Physical Chemistry Chemical Physics **14** (2012) 13154.

[29] G. Socrates, *Infrared and Raman Characteristic Group Frequencies: Tables and Charts*, Wiley, 2004.

Chapter 6

Improving the resolution of a lock-in measurement by tailoring the modulation

This work stemmed from the effort in optimizing the STM-IETS measurement presented in the previous chapter; due to its more general relevance, not limited to STM spectroscopies, it is the subject of a separate publication [1]. It would not have been possible outside a scientific environment like the SSR group at the Tasc laboratory, at the same time it is particularly "personal", meaning that it comes from an idea of mine, and that I personally conceived and performed the calculations, the numerical simulation, and the experiments.

6.1 Introduction

Phase-sensitive detection with a lock-in amplifier [2] is a general measurement scheme finding the most diverse applications in science and technology. Just to name a few, it is used in the measurement of electronic [3] or vibrational [4] properties of single adsorbed molecules with a Scanning Tunneling Microscope (STM); in the spectroscopy of paramagnetic centers in materials by means of Electron Paramagnetic Resonance spectroscopy (EPR) [5]; in the high-sensitivity detection of gas-phase species with Wavelength-Modulation optical absorption Spectroscopy (WMS) [6]; in the characterization of the doping profile of semiconductors by capacitance-versus-voltage measurements [7].

Generally speaking, in all the mentioned examples the system under study is stimulated by adding a sinusoidal modulation of frequency f to a parameter s used as an excitation in the experiment. The lock-in amplifier is then used to extract the amplitude of the Fourier component at the h-th harmonic hf ($h = 1, 2, 3, \ldots$) from the time-dependent response $R(t)$ of the system. These Fourier components are related to the h-th order derivatives $\mathrm{d}^h R/\mathrm{d}s^h(s)$ of the system's response with respect to the stimulus, which are the final goals of the measurement.

Phase-sensitive detection is fundamental in demanding experimental conditions, for instance when the measured response $R(t)$ is dominated by $1/f$-like noise [2]. In these cases a proper choice of the modulation frequency f in a low-noise region of the spectrum can increase the Signal-to-Noise Ratio (SNR) of the measurement by orders of magnitude, allowing to precisely measure signals that would otherwise be undetectable. In general, boosting the amplitude of the sinusoidal modulation further improves the SNR, as the intensity of the recovered signal increases; at the same time, though, the resolution along the s-axis is conversely reduced by the so-called modulation broadening. A compromise has thus to be made, by trading signal – and ultimately measurement time – for experimental resolution.

In this work we demonstrate both numerically and experimentally that this modulation-induced broadening can be reduced by employing a tailored modulation function in place of the commonly-used sinusoid. This result is based on a mathematical analysis of the lock-in output, which reveals two key aspects of the lock-in functionality. On one side, it shows that the signal at the h-th harmonic is not simply proportional to the h-th order derivative, but contains also undesirable terms involving higher-order derivatives. Although this fact has been known for a long time [8], these higher-order terms are usually neglected. On the other side, we find a quantitative relation between these higher-order components and the modulation broadening, which is suggestive on how to systematically reduce the latter.

From the experimental point of view, we tested the proposed scheme in Inelastic Electron tunneling Spectroscopy (IETS) experiments with an STM [4], where the vibrational modes of a single molecule adsorbed on a conductive surface are detected by measuring the second derivative $\mathrm{d}^2I/\mathrm{d}V^2(V)$ of the current I tunneling trough the molecule with respect to the bias voltage V between the sample and the tip of the microscope. For this reason, without loss of generality, we focused the present investigation on the detection of the second harmonic ($h = 2$). Indeed, the ideas and analysis presented can be easily applied to all cases where a lock-in amplifier is used to measure a second derivative, and can also be extended to the detection of derivatives of order $h \neq 2$. Our results are particularly suited for situations where a better SNR would be desirable, but the modulation amplitude cannot be increased since it is the factor limiting the resolution of the measurement.

The paper s organized as follows: we will first present the analysis of the lock-in output on which this work is grounded: then the numerical search for a better modulation function will be illustrated; finally its performance will be experimentally assessed. Since we are interested in STM-IETS experiments, from here on we specialize our notation: the sample-tip bias voltage V will stand in for the stimulus s, and the tunneling current I for the response R. For the sake of brevity, we will also indicate the d-th derivative of the current with respect to the bias voltage as $I^{(d)}$ rather than $\mathrm{d}^dI/\mathrm{d}V^d$.

6.2 Analysis of the lock-in output

In our search for a method to control and reduce the modulation-induced broadening, we start by investigating the analytical expression of the lock-in output.

The output of a lock-in amplifier tuned to detect the h-th harmonic of the modulation frequency is [9]

$$\mathrm{out}_h(V_0) = \frac{2}{T} \int_{-\frac{T}{2}}^{\frac{T}{2}} \mathrm{d}t \; I(V_0 + V_\mathrm{m} \cos(2\pi f t)) \; \cos(2\pi h f t) \tag{6.1}$$

Here, the bias voltage V_0 is modulated by a sinusoid of amplitude V_m and frequency f. The lock-in amplifier acquires the resulting modulated current $I(t)$, multiplies it by a demodulating sinusoid at frequency hf and integrates over a period $T = f^{-1}$. Its output is thus the real part of the Fourier component at frequency hf of the current $I(t)$, expressed as a peak amplitude. In most lock-ins the integration over time is done by low-pass filtering, therefore the above expression is an idealization asymptotically valid for measurement times much longer than the response time of the filter. Moreover, this expression also neglects the possible phase shift between the tunneling current response and the demodulation sinusoid, which however can be easily compensated by dephasing the latter.

Starting from equation (6.1), Klein and co-workers [9] demonstrated that the lock-in output at twice the modulation frequency ($h = 2$ in the equation) can be expressed as a convolution of the second derivative $I^{(2)}(V)$ of the current with respect to the bias voltage, with an instrumental function ϕ,

$$\mathrm{out}_2(V_0) = \int_{-\infty}^{+\infty} \mathrm{d}x \; I^{(2)}(V_0 - x) \; \phi(x) \tag{6.2}$$

where the instrumental function was found to be

$$\phi(V) = \begin{cases} \dfrac{2}{3\pi} \; V_\mathrm{m} \; \left(1 - \left(\dfrac{V}{V_\mathrm{m}}\right)^2\right)^{\frac{3}{2}} & \text{for } V \in [-V_\mathrm{m}; V_\mathrm{m}] \\ 0 & \text{otherwise} \end{cases} \tag{6.3}$$

$\phi(V)$ is plotted in figure 6.1.

From the above expression is evident that both the height and the width of ϕ scale with the modulation amplitude V_m: this shows clearly why boosting V_m increases the output signal, but also spoils the voltage resolution.

Starting from the same equation (6.1), we derived a different expression for the lock-in output at a generic harmonic h. By expanding the current I as a Taylor series around $V = V_0$ (see appendix 6.A for details), we obtained a series of the derivatives of $I(V)$ with respect to the bias voltage, namely

$$\mathrm{out}_h(V_0) = \sum_{d=h}^{+\infty *} c_{hd} \; I^{(d)}(V_0) \; V_\mathrm{m}^d \tag{6.4}$$

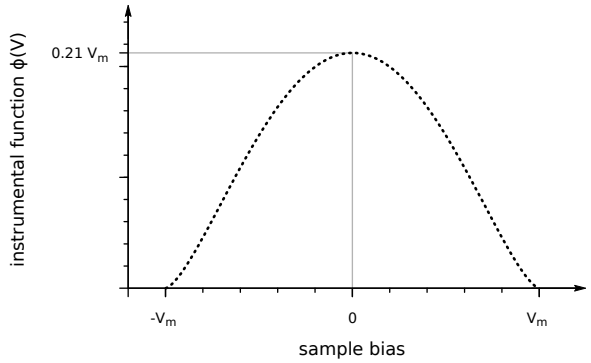

Figure 6.1: Instrumental function $\phi(V)$ of a lock-in amplifier detecting at twice the modulation frequency, using a sinusoidal modulation of amplitude V_m.

where the weights c_{hd} are

$$\begin{aligned} c_{0d} &= \frac{1}{2^{d+1}\ \left(\frac{d}{2}\right)!} && \text{for } h = 0 \\ c_{hd} &= \frac{1}{2^{d-1}\ \left(\frac{d+h}{2}\right)!\ \left(\frac{d-h}{2}\right)!} && \text{for } h > 0 \end{aligned} \tag{6.5}$$

The series starts from the h-th derivative, and the starred sum means that only the terms with the same parity of h are included, i. e. $d = h,\ h+2,\ h+4,\ \ldots$. For instance, the output at the second harmonic of the modulation frequency is

$$\begin{aligned} \mathrm{out}_2(V_0) = \frac{1}{4}\, I^{(2)}(V_0)\, V_\mathrm{m}^2 + \frac{1}{48}\, I^{(4)}(V_0)\, V_\mathrm{m}^4 \\ + \frac{1}{1536}\, I^{(6)}(V_0)\, V_\mathrm{m}^6 + \frac{1}{92160}\, I^{(8)}(V_0)\, V_\mathrm{m}^8 + \cdots \end{aligned} \tag{6.6}$$

and involves *all* the even derivatives of $I(V)$.

Since the two expressions for the lock-in output, (6.2) and (6.6), are both derived from equation (6.1), a direct link between them is expected. Indeed, as shown in appendix 6.B, the weights c_{2d} are related to the moments μ_{d-2} of the instrumental function ϕ:

$$(d-2)!\ c_{2d} = \frac{\mu_{d-2}}{V_\mathrm{m}^d} \tag{6.7}$$

valid for $d \geq 2$, where the moments are defined as $\mu_j = \int_{-\infty}^{+\infty} \mathrm{d}V\ V^j\ \phi(V)$. Therefore, for instance, the weight c_{24} of $I^{(4)}(V)$ is linked to the variance μ_2 of ϕ, thus measuring its spread.

6.3 The new modulation function

The analysis carried out in the previous section shows that the modulation broadening is directly related to the presence of higher-order derivatives in the output of the lock-in at $h = 2$. We now want to determine whether it is possible to reduce the contribution of these unwanted components by using as a modulation function a tailored, general periodic waveform instead of the traditional sinusoid $V_\mathrm{m}\cos(2\pi f t)$. If we express a generic modulating waveform by its Fourier series

$$\mathrm{mod}(t) = V_\mathrm{m}\sum_{k=1}^{+\infty}(a_k\cos(2\pi k f t) + b_k\sin(2\pi k f t)) \tag{6.8}$$

the lock-in output in equation 6.1 becomes

$$\mathrm{out}_h(V_0) = \frac{2}{T}\int_{-\frac{T}{2}}^{\frac{T}{2}}\mathrm{d}t\ \ I(V_0 + \mathrm{mod}(t))\ \ \cos(2\pi h f t) \tag{6.9}$$

Following once more the approach described in appendix 6.A, the output can be expanded in a Taylor series of I around V_0, leading also in this general case to a series of the derivatives of $I(V)$:

$$\mathrm{out}_h(V_0) = \sum_{d=h}^{+\infty}\tilde{c}_{hd}\ I^{(d)}(V_0)\ V_\mathrm{m}^d \tag{6.10}$$

The new weights $\tilde{c}_{hd}(\{a_k\},\{b_k\})$ of this series are a function of the sets of Fourier coefficients $\{a_k\}$ and $\{b_k\}$, which uniquely define the modulation waveform. Therefore the $\tilde{c}_{hd}$ can be tailored to a certain extent by properly choosing the modulation function. It is reasonable to argue that, for any given harmonic h, decreasing all the weights $\tilde{c}_{hd}$ but the first one $\tilde{c}_{hh}$, will make the lock-in output $\mathrm{out}_h(V_0)$ more close to the h-th derivative $I^{(h)}(V_0)$, thereby reducing the modulation broadening. It is to be noted that we did not investigate analytically under which conditions the lock-in output in this general case can be expressed by a convolution with an instrumental function, however from now on we will assume this hypothesis, which is consistent with our numerical and experimental findings.[1]

Continuing our investigation, we explored what happens when the modulation function is changed in the case $h = 2$ by means of a variational approach implemented within the *Mathematica* computational environment [10]. In the following we will briefly describe the general procedure and the main outcomes, whereas a sample of our *Mathematica* code and some more technical details are reported in

[1] To this regard, in a preliminary investigation – not reported here – we demonstrated that the lock-in output can always be expressed as a convolution if the modulation function is even-symmetric and invertible upon restriction of the domain to $t \in \left[0, \frac{T}{2}\right)$.

Table 6.1: The final optimized values of the non-zero Fourier coefficients defining by means of equation (6.8) the modulation function labeled "Fourier series" in figure 6.2.

coefficient	value
a_1	1.0000
a_3	0.0412
a_5	−0.2681
a_7	0.1065
a_9	0.1263
a_{11}	−0.1218
a_{13}	−0.0411
a_{15}	0.0892
a_{17}	−0.0115

the supplementing materials. As a first step, we defined a trial modulation function of the form (6.8), truncated at a cut-off harmonic K. Second, we derived analytically the expression of the weights $\tilde{c}_{2d}$ as explicit functions of the coefficients $\{a_1, \ldots, a_K, b_1, \ldots, b_K\}$, along the lines described in appendix 6.A. By varying the values of these coefficients, we numerically minimized the square of the most important undesired term $(\tilde{c}_{2\,4})^2$, while constraining $(\tilde{c}_{2\,2})^2 \geq (c_{2\,2})^2$, in order to enhance the relative weight of the second derivative $I^{(2)}(V_0)$ in the measured signal. In this way we obtained a set $\{a_1, \ldots, a_K, b_1, \ldots, b_K\}$ which defines our new, optimized modulation function.

The top panel of figure 6.2 shows a comparison of the standard sinusoid with different modulation waveforms. The wave labeled "Fourier series" is a typical outcome of the above-described procedure, obtained with a trial function having Fourier components up to the 17^{th} harmonic of the modulation frequency (table 6.1). The bipolar "pulse train" was instead obtained heuristically, by examining the optimized waveforms at different values of the cutoff K, and assuming that they converge to a simply shaped one for $K \to +\infty$. This function has a duty cycle of 0.5, and is discontinuous at $2\pi f t = \frac{\pi}{4}, \frac{3}{4}\pi, \frac{5}{4}\pi, \frac{7}{4}\pi, \ldots$

The performance of the new modulations was then assessed numerically, by calculating the corresponding lock-in output using equation (6.9). First we checked with a known $I(V)$ that in the small-modulation limit the second derivative $I^{(2)}(V)$ is exactly retrieved, as expected. Subsequently we replaced $I(V)$ with $V\,\Theta(V)$, where $\Theta(V)$ is the unit step function: since the second distributional derivative of $V\,\Theta(V)$ is the Dirac delta $\delta(V)$, in this way we could determine how the lock-in detects an infinitely sharp feature in the second derivative of the input. In other words, this is a measure of the instrumental function of the lock-in, obviously under the hypothesis that also with a general modulation the lock-in output can be expressed as a convolution of the form (6.3). As can be seen in the lower panel of figure 6.2, the two

new modulations lead to instrumental functions sharper than the one of the simple sinusoid: this demonstrates that it is indeed possible to improve the resolution of lock-in measurements by tailoring the modulation function.

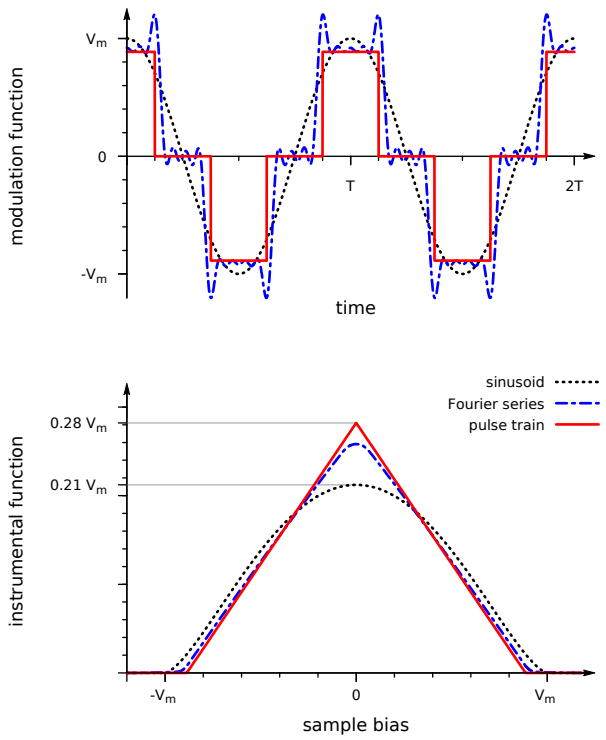

Figure 6.2: Three different modulation functions (top panel) with their corresponding instrumental functions (bottom panel). Here the relative amplitude of the different modulations was chosen to have instrumental functions with the same integral, leading thus to the same signal level when measuring features of $I^{(2)}(V)$ significantly wider than the modulation amplitude.

6.4 Experiment

To assess the performance of this new modulation scheme in a real experimental scenario, we compared the effect of the "bipolar pulse train" modulation against the standard sinusoid, by measuring by STM-IETS spectra. In particular we acquired the low-energy vibrational spectrum of a single carbon monoxide molecule adsorbed on the (110) surface of copper, a well-studied test system [11], due to the relatively high intensity of the features at ±36 mV, associated to the CO hindered rotation.

We performed our experiments in a Ultra-High Vacuum (UHV) system (base pressure 2×10^{-8} Pa), where the Cu(110) single crystal was prepared by sputtering

(1 keV normal-incidence Ne^+ beam with the sample at room temperature) and annealing cycles (900 K for 10 min, 2 K/s linear heating ramp, 0.5 K/s cooling). Carbon monoxide (SIAD, purity 99.97%) was adsorbed on the sample, kept at $T < 170\,\mathrm{K}$, by backfilling the preparation chamber in the 10^{-7} Pa range, for a net exposure of about 80 mL = $1.1 \times 10^{-5}\,\mathrm{Pa \cdot s}$. IETS measurements were performed using a commercial Omicron LT-STM microscope, operated at a sample temperature of about 5 K, equipped with Omicron MATRIX control electronics and the standard Omicron SPM PRE_4 I/V converter (gain 3×10^7 V/A, bandwidth 40 kHz when connected to the STM). The modulation was generated by a Tektronix AFG 3252 arbitrary function generator (bandwidth 120 MHz), synchronized to the Stanford Research Systems SR830 lock-in amplifier used for detection. We modulated the sample bias at a frequency $f = 4216\,\mathrm{Hz}$, with an overall noise density in the tunneling current at $2f$ of the order of $660\,\mathrm{fA_{pk}}/\sqrt{\mathrm{Hz}}$, measured at $I = 10\,\mathrm{nA}$. The lock-in low-pass filter was a fourth-order RC filter with a −3 dB cut-off frequency of 2.31 Hz (30 ms time constant, 24 dB/oct roll-off), corresponding to an Equivalent Noise BandWidth (ENBW) of 2.60 Hz. The phase shift between the modulation function and the demodulation sinusoid was chosen in order to zero the imaginary part of the lock-in output (lock-in's quadrature output). The acquisition of the IETS spectra started after having positioned the STM tip over a CO molecule, with the feedback loop of the microscope fixing the tip-sample distance in order to get the desired tunneling current at the sample bias used. The feedback loop was then turned off, the chosen modulation was added to the sample bias, and the latter was ramped in 1 mV steps while recording the corresponding lock-in output. To avoid artifacts due to the finite response time of the low-pass filter of the lock-in, its output was allowed to settle for 210 ms at the beginning of each voltage step, before acquiring data for 5 ms. After each bias ramp the measurement was repeated by sweeping the voltage in the opposite direction: the comparison of the "forward" and the "backward" spectra was used to spot possible artifacts related to the residual thermal drift of the tip-to-sample distance, or to insufficient filter settling. The described measurement sequence was repeated several times, averaging the resulting spectra until the desired signal-to-noise ratio was achieved. Checks to correct for possible lateral drift of the STM tip with respect to the molecule were performed from time to time. In order to highlight the molecular features, from every measurement carried out on a molecule a spectrum subsequently recorded on the bare copper surface was always subtracted.

Since the voltage resolution can be traded for signal intensity by changing the modulation amplitude, we compared the performance of the "bipolar pulse train" against the conventional sinusoid in two different situations. In a first test (figure 6.3 top panel) the relative amplitudes of the two modulations were set in order to yield instrumental functions characterized by the same width but different maxima (inset), thus expected to yield the same voltage resolution with a different signal strength. We repeated the IETS measurement on the same molecule using both modulations, and indeed the "new" spectrum overlaps almost exactly to the "conventional" one when scaled by a factor of 1.21. This is not surprising, because

our situation is intermediate between two opposite limits, as explained in the following. On one hand, if the spectral features were much wider than the modulation broadening, a perfect scaling would be expected, with a scale factor of 1.15, i. e. the ratio between the integrals of the two instrumental functions. On the other hand, if the features were much narrower than the modulation broadening, the two experimental curves would not be proportional any more, since the different shapes of the two instrumental functions would dominate the spectra. The ratio between the peak maxima would be 1.42, i. e. the ratio between the maxima of the two instrumental functions. As anticipated, the observed scaling factor is intermediate between these two extrema.

In a second test (figure 6.3 bottom panel) we chose the modulation amplitudes to yield the same experimental signal intensity at the CO hindered rotation features. Indeed, as expected, in this case the new modulation shows a significant improvement, delivering a better resolved spectrum and confirming thus the validity of our approach.

Finally, two general remarks on the bandwidth required by this new modulation scheme: first, there are no special requisites on the detection bandwidth, since only the Fourier component at twice the modulation frequency f is measured, as with the standard sinusoidal modulation. Second, an infinite bandwidth is instead needed to deliver a perfect pulse train to the system under investigation. In principle, thus, this measurement scheme could find limited applicability in experimental techniques where the available modulation bandwidth is instead small. Indeed, also our modulation waveform was noticeably distorted by the finite cut-off – approximatively 60 kHz, slightly more than $14f$ – of the modulation input of the Omicron MATRIX electronics. To verify whether the shape of the instrumental function was significantly affected, we reduced the distortion by lowering the modulation frequency from 4216 Hz to 304 Hz, and then repeated the measurement of figure 6.3. Similar results were obtained, with a ratio of 1.22 – instead of 1.21 – between the spectra acquired with the "new" and the "conventional" modulation. This means that most of the sharpening of the instrumental function already comes form the first Fourier components of the modulation, as can be seen in the lower panel of figure 6.2: the instrumental function of the "Fourier series" (cut-off at $17f$) is already quite similar to the one of the "pulse train" (no cut-off).

6.5 Conclusions

By carefully examining what a lock-in amplifier really measures we were able to devise a more efficient modulation scheme, capable of increasing both the signal level and the resolution of a second-harmonic lock-in measurement. In particular, at fixed resolution we achieved a signal gain between 15% and 42%, depending on the width of the measured features. This scheme was eventually verified in a STM-IETS experiment, where the experimental realization is simple, requiring only an arbitrary waveform generator to be added to the existing setup. However, this

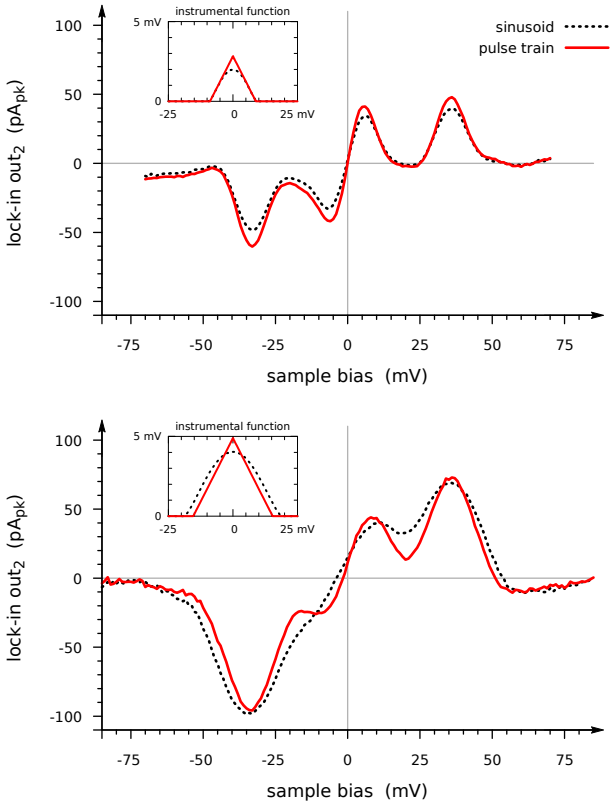

Figure 6.3: STM-IETS spectra of CO/Cu(110), using either the standard sinusoidal modulation (dotted line) or the pulse train (continuous line) described in the text. The insets show the calculated instrumental functions of the modulations used. In the top panel the modulation amplitudes were chosen to yield the same voltage resolution, whereas in the bottom panel they yield the same signal intensity at the CO hindered rotation features at ±36 mV. Experimental parameters: (top panel) tip stabilized at $V = -70\,\mathrm{mV}$, $I = 20\,\mathrm{nA}$, modulation amplitudes $V_\mathrm{m} = 9.4\,\mathrm{mV_{pk}}$ for the sinusoidal modulation and $V_\mathrm{m} = 8.9\,\mathrm{mV_{pk}}$ for the bipolar pulse train; each measurement required 22 min of acquisition time, corresponding to the average of 20 spectra on the molecule and 20 on the copper surface; (bottom panel) tip stabilized at $V = -85\,\mathrm{mV}$, $I = 15\,\mathrm{nA}$, modulation amplitudes $V_\mathrm{m} = 19.0\,\mathrm{mV_{pk}}$ for the sinusoidal modulation and $V_\mathrm{m} = 15.4\,\mathrm{mV_{pk}}$ for the bipolar pulse train; each measurement required 5 min, corresponding to 4 spectra on the molecule and 4 on the copper surface.

scheme is not limited to this technique and can be used whenever a second derivative is measured with a lock-in amplifier. Moreover, the ideas presented here can be readily extended to the measurement of other derivatives, for instance in the $\mathrm{d}I/\mathrm{d}V(V)$ electronic spectroscopy with an STM. Our results are particularly suited for situations where i) a better SNR would be desirable; ii) the modulation amplitude cannot be increased, since it is the factor limiting the resolution of the measurement; and iii) it is feasible to drive the system under study with an arbitrary modulation waveform.

We regard the present investigation as a simple but significant proof-of-concept, since we limited ourselves to a small subset of the possible modulation functions. Indeed, the triangular instrumental function of figure 6.2 is not unique: we verified that qualitatively different shapes are also attainable. In this regard, a still important open point is the elucidation of the analytical relationship between the modulation function and the corresponding instrumental function.

Eventually, substituting also the $\cos(2\pi\, 2f\, t)$ demodulation sinusoid with a Fourier series would make the lock-in output a linear combination of the Fourier components of $I(t)$ at the various harmonics of the modulation frequency. This can be exploited to further reduce the contribution of unwanted derivatives in the measured signal, and thus the modulation broadening. In doing this it should be kept in mind that the detection bandwidth has to be above the highest Fourier component included in the demodulation function used, and that the RMS value of the latter has to be limited, since the collected noise is roughly proportional to it.

Appendices

6.A Lock-in output as a series of derivatives

Here we derive the expression (6.4) of the lock-in output as a series of the derivatives of $I(V)$.

First we expand the current I in a Taylor series around $V = V_0$, assuming that $I(V)$ is sufficiently well-behaved that his Taylor series converges to $I(V)$ itself for any V_m of experimental relevance.

$$\begin{aligned} I(V) &= I(V_0 + V_\mathrm{m}\cos(2\pi f t)) \\ &= \sum_{d=0}^{+\infty} \frac{1}{d!}\, I^{(d)}(V_0)\ \ (V_\mathrm{m}\cos(2\pi f t))^d \end{aligned}$$

Then, using Euler's formula and the binomial theorem to expand the $\cos^d(2\pi f t)$ terms, we obtain

$$= \sum_{d=0}^{+\infty} \frac{1}{d!}\, I^{(d)}(V_0)\; V_\mathrm{m}^d\; \frac{1}{2^d} \sum_{k=0}^{d} \binom{d}{k} e^{2\pi i(2k-d)ft}$$

By defining a new sum index $h = 2k - d$ and rearranging the equation we get a series of complex exponentials

$$= \sum_{h=-\infty}^{+\infty} e^{2\pi i h f t} \sum_{d=|h|}^{+\infty *} \frac{1}{2^d \left(\frac{d+h}{2}\right)! \left(\frac{d-h}{2}\right)!} I^{(d)}(V_0)\, V_\mathrm{m}^d$$

where the star means that only the terms with the same parity of $|h|$ enter the sum over d, i. e. $d = |h|,\ |h| + 2,\ |h| + 4,\ \ldots$. To go from exponentials back to sinusoids we pick out the $h = 0$ term and pair the h and $-h$ ones, obtaining

$$I(V) = \sum_{h=0}^{+\infty} \cos(2\pi h f t) \sum_{d=h}^{+\infty *} c_{hd}\, I^{(d)}(V_0)\, V_\mathrm{m}^d$$

where

$$c_{0d} = \frac{1}{2^{d+1} \left(\frac{d}{2}\right)!} \qquad \text{for } h = 0$$

$$c_{hd} = \frac{1}{2^{d-1} \left(\frac{d+h}{2}\right)! \left(\frac{d-h}{2}\right)!} \qquad \text{for } h > 0$$

and $d \geq h$ has the same parity of h. Inserting this expansion for $I(V)$ in the expression (6.1) for the lock-in output, the orthogonality of sinusoids leaves only one term in the sum over h, leading to

$$\mathrm{out}_h(V_0) = \sum_{d=h}^{+\infty *} c_{hd}\, I^{(d)}(V_0)\, V_\mathrm{m}^d$$

which is equation (6.4).

6.B Link between the two expressions for the lock-in output at $2f$

Here we show the equivalence of the expressions of the lock-in output at twice the modulation frequency respectively as a convolution with an instrumental function (equation 6.2), and as a series of the derivatives $I^{(d)}(V_0)$ (equation 6.4 with $h = 2$), by deriving the relation (6.7) between the weights c_{2d} of the series and the moments of the instrumental function ϕ defined in equation (6.3).

The moments μ_j are defined as

$$\mu_j = \int_{-\infty}^{+\infty} \mathrm{d}V \;\; V^j\, \phi(V)$$

Since ϕ is zero outside the interval $[-V_\mathrm{m}, V_\mathrm{m}]$, the integration can be limited to this range. ϕ is an even function, so the odd moments vanish, whereas for the even ones

one has

$$\mu_{d-2} = 2 \int_0^{V_\mathrm{m}} \mathrm{d}V \;\; V^{d-2} \; \phi(V)$$

Inserting here the expression (6.3) of ϕ and defining the new integration variable $y = V^2/V_\mathrm{m}^2$, we arrive to

$$= \frac{2}{3\pi} \; V_\mathrm{m}^d \int_0^1 \mathrm{d}y \;\; y^{\frac{d-3}{2}} \; (1-y)^{\frac{3}{2}}$$

where the integral defines Euler's beta function $B(\frac{d-1}{2}, \frac{5}{2}) = \frac{3\pi \; (d-2)!}{2^d \; (\frac{d}{2}+1)! \; (\frac{d}{2}-1)!}$. Thus

$$\mu_{d-2} = \frac{1}{2^{d-1} \; \left(\frac{d}{2}+1\right)! \; \left(\frac{d}{2}-1\right)!} \; (d-2)! \; V_\mathrm{m}^d$$

where, using the definition (6.5) of the c_{2d}, we arrive at equation (6.7)

$$(d-2)! \; c_{2d} = \frac{\mu_{d-2}}{V_\mathrm{m}^d}$$

We turn now to the convolution (6.2)

$$\mathrm{out}_2(V_0) = \int_{-\infty}^{+\infty} \mathrm{d}x \;\; I^{(2)}(V_0 - x) \; \phi(x)$$

First we develop $I^{(2)}(V)$ in a Taylor series around V_0, which needs to converge to $I^{(2)}(V)$ only inside the interval $[-V_\mathrm{m}, V_\mathrm{m}]$, since ϕ is zero outside it (see equation 6.3).

$$= \int_{-\infty}^{+\infty} \mathrm{d}x \;\; \sum_{j=0}^{+\infty} \; \frac{1}{j!} \; I^{(2+j)}(V_0) \; (-x)^j \; \phi(x)$$

We then define the new sum index $d = j + 2$ and rearrange, using the fact that ϕ is an even function

$$= \sum_{d=2}^{+\infty} \; I^{(d)}(V_0) \; \frac{1}{(d-2)!} \int_{-\infty}^{+\infty} \mathrm{d}x \;\; x^{d-2} \; \phi(x)$$

The integrals are the moments μ_{d-2} of ϕ derived above; since they vanish if $d-2$ is odd, we arrive to the expression (6.4) of the lock-in output at $2f$ as a series of derivatives of $I(V)$

$$= \sum_{d=2}^{+\infty *} c_{2d} \; I^{(d)}(V_0) \; V_\mathrm{m}^d$$

where the starred sum indicates that only the even terms $d = 2, 4, 6, \ldots$ are included.

6.C The code

A sample of the Mathematica code used to search for better modulation functions and to assess their performance is available on-line. We used as a trial modulation function a sum of *cosines* of the *odd* harmonics of the modulation frequency, instead of the most general Fourier expansion of equation (6.8), for two specific reasons. First, for a general modulation the lock-in output out_h at a certain harmonic h is a series of *all* the derivatives $I^{(d)}$ of order $d \geq h$. To have only the derivatives of order d of the same parity of h, as it is the case for the traditional sinusoidal modulation, it is sufficient to include only odd-k terms in the Fourier expansion (6.8). Second, the main weakness of the method we use is that we minimize $(\tilde{c}_{2\,4})^2$ only. As soon as the number of Fourier coefficients of the modulation function gets high enough, it is easy to end up in a minimum of $|\tilde{c}_{2\,4}|$ where instead $|\tilde{c}_{2d}| > |c_{2d}|$ for $d > 2$, leading eventually to a wider instrumental function. One could further constrain $(\tilde{c}_{2\,6})^2 \leq (c_{2\,6})^2, (\tilde{c}_{2\,8})^2 \leq (c_{2\,8})^2, \ldots$ or minimize a suitable combination of the $\tilde{c}_{2d}$, but the computational cost would quickly become an issue. For this reason we excluded the sine terms to limit the number of variables in the minimization, getting thus an even-symmetric modulation function.

References

[1] A. Peronio, C. Dri, and G. Comelli, *Improving the resolution of a lock-in measurement by tailoring the modulation*, Rev. Sci. Instrum. (2013) submitted.

[2] M. L. Meade, *Lock-in amplifiers: principles and applications*, Peter Peregrinus, London 1983.

[3] R. Wiesendanger, *Scanning probe microscopy and spectroscopy: methods and applications*, Cambridge University Press, Cambridge 1994.

[4] B. C. Stipe, M. A. Rezaei, and W. Ho, *Single-Molecule Vibrational Spectroscopy and Microscopy*, Science **280** (1998) 1732.

[5] A. Abragam and B. Bleaney, *Electron paramagnetic resonance of transition ions*, Dover Publications, New York 1986.

[6] J. A. Silver, *Frequency-modulation spectroscopy for trace species detection: theory and comparison among experimental methods*, Appl. Opt. **31** (1992) 707.

[7] P. Blood and J. W. Orton, *The electrical characterisation of semiconductors*, Rep. Prog. Phys. **41** (1978) 157.

[8] W. R. Patterson and J. Shewchun, *Alternate Approach to the Resolution of Tunneling Current Structure by Differentiation*, Rev. Sci. Instrum. **35** (1964) 1704.

[9] J. Klein, A. Léger, M. Belin, D. Défourneau, and M. J. L. Sangster, *Inelastic-Electron-Tunneling Spectroscopy of Metal-Insulator-Metal Junctions*, Phys. Rev. B **7** (6 1973) 2336.

[10] Wolfram Research, Inc., *Mathematica 8.0*, Wolfram Research, Inc., Champaign 2010.

[11] L. J. Lauhon and W. Ho, *Single-molecule vibrational spectroscopy and microscopy: CO on Cu(001) and Cu(110)*, Phys. Rev. B **60** (12 1999) R8525.

Chapter 7

Conclusions and outlook

In this thesis work model systems for heterogeneous catalysis have been investigated by means of a combined approach, where the molecular-level insight provided by low-temperature scanning tunneling microscopy is complemented by density-functional-theory calculations of their electronic structure.

By comparing the experimental and DFT-calculated STM images of single CO_2 molecules and molecular complexes, the precise adsorption geometry of CO_2 adsorbed on Ni(110) has been determined. Whereas this closed-shell molecule usually physisorbs on transition-metal surfaces, in the case of Ni(110) it is found in a chemisorbed state, characterized by an high electron transfer from the surface and a bent geometry. This activated species is a precursor for CO_2 hydrogenation to methanol, explaining the peculiar activity of Ni-based catalysts towards this reaction. It is to be noted that the structure of this intrinsically disordered system cannot be determined by the usual surface-sensitive diffractive techniques, such as SPA-LEED or XPD.

The same combined approach allowed us to characterize the structure of the NH_3–NO coadsorption complex on the (111) surface of platinum, which was shown to be a 2×2 ordered adlayer where ammonia sits on top and NO on fcc-hollow sites. The strength of this picture arises from the agreement between the adsorption characterization provided by DFT and the existing experimental results. The two molecules interact via a surface-mediated charge transfer form the NH_3 lone-pair orbital to NO π^* one, as was previously detected by NEXAFS, and the calculated vibrational energies of both the coadsorption structure and of its constituents fit the experimental spectra found in literature. Evidence was found about a direct hydrogen bond between the hydrogen of ammonia and the oxygen of NO, which contributes to the complex stability together with the more important substrate-mediated interaction.

NH_3 and NO are stabilized in a coadsorption layer where the two molecules are in a favorable geometry to react together, and the question naturally arises whether this same complex has a relevant role in the selectivity of NO reduction also in real reaction conditions (ambient pressure or above, and temperatures up to 300 °C).

A proper answer requires further investigation: first of all the possible influence of other coadsorbed species should be taken into account, such as oxygen, which is always present in combustion exhausts. Secondly, an indication about the relevance of the pressure gap in the present case could come from *in situ* measurements up to near-ambient or reaction conditions, for instance by means of High-Pressure X-ray Photoelectron Spectroscopy (HP-XPS), or Sum-Frequency Generation vibrational spectroscopy (SFG).

for the first time in our laboratory, I have performed vibrational spectroscopy on single molecules by means of the STM-IETS technique. The key to the successful introduction of this challenging method has been a thorough understanding of the role of the various experimental parameters (tunneling current, modulation frequency, lock-in settings, ...) on the achieved signal-to-noise ratio. The frequency-dependent spectral density proved to be an essential, powerful tool to characterize and rationalize the different effects involved. The work done up to now allowed to depart from standard test systems – CO/Cu(110)– to successfully measure a 1500-times weaker signal, namely on the cysteamine molecule chemisorbed on Au(111). Further improvements are however foreseeable with the introduced methods. For instance, the spectral density of the voltage driving the piezoelectric actuator of the STM tip should be measured, to understand whether this is the factor limiting the noise baseline at high tunneling currents.

This characterization and optimization regarded also the energy resolution of STM-IETS spectra. To this respect, by carefully examining what a lock-in amplifier really measures, we discovered that it is possible to increase both the signal level and the resolution of a second-harmonic lock-in measurement. This is done simply by using a tailored modulation function, different from the commonly-used sinusoid. In particular, at fixed resolution we achieved a signal gain between 15% and 42%, depending on the width of the measured features. This scheme was verified in a pilot STM-IETS experiment, but it is not limited to this technique, and can be used whenever a second derivative is measured with a lock-in amplifier. Moreover, the ideas presented can be readily extended to the measurement of other derivatives, for instance in the $\mathrm{d}I/\mathrm{d}V(V)$ electronic spectroscopy with an STM. Many questions remain open, such as the elucidation of the analytical relationship between the modulation function and the corresponding lock-in instrumental function, or the possibility to tailor also the demodulation function.